

**Excited State Interactions and Management
in Organic Light Emitting Diodes**

by
Yifan Zhang

A dissertation submitted in partial fulfillment
of the requirements for the degree of
Doctor of Philosophy
(Physics)
in the University of Michigan
2014

Doctoral Committee:

Professor Stephen R. Forrest, Chair
Associate Professor Max Shtein
Assistant Professor Vanessa Sih
Professor L. Jay Guo

© Copyright by Yifan Zhang
2014

Acknowledgements

This thesis would have been impossible without the help from others. First, I acknowledge my advisor, Professor Stephen Forrest for his intellectual as well as financial support. Over the past years, I have been deeply inspired and energized by his exceptional scientific insight and dedication towards the highest standard of work. I also feel grateful that he gave me flexibility as well as trust in the projects I was on. I do not know how to return his favor, but I will surely carry on the spirit of always thinking critically and acting promptly.

Working in an interdisciplinary group with members from both science and engineering backgrounds offered me an unparalleled opportunity to learn from my colleagues. As my mentors, Stéphane Kéna-Cohen, Noel Giebink, and Xiangfei Qi familiarized me with basic experimental as well as data analysis techniques. Michael Sloatsky offered me numerous critical suggestions, including editing my first research paper manuscript, sharing with me a low temperature photoluminescence setup, and teaching me how to design and fabricate printed circuit boards. Jaesang Lee assisted me with device fabrication and characterization, which accelerated my progress in the final project. Eva Ruff not only provided reliable support as the group administrator, but also proofread this dissertation. I am also thankful to other group members for the enjoyable time we spent in the lab, during group meetings, and beyond. Among them are Jeramy

Zimmerman, Xin Xu, Richard Lunt, Kuen-Ting Shiu, Xuhuai Zhang, Guodan Wei, Greg McGraw, Brian Lassiter, Kyle Renshaw, Xiaoran Tong, Kevin Bergemann, Xin Xiao, Kyusang Lee, Xiaolong Hu, Nana Wang, Cedric Rolin, Olga Griffith, ByeongSeop Song, Anurag Panda, Xiao Liu, Quinn Burlingame, Xiaozhou Che, Dejiu Fan, Yue Qu, Wen Yu, Shota Nunomura, and the ones I forget to mention.

In addition, I acknowledge the contribution from Professor Mark Thompson at the University of Southern California on some of my projects. Also, Dr. Julie Brown at Universal Display Corp. offered experimental supplies and helpful suggestions that are essential for part of this thesis. I also acknowledge Professor Max Shtein, Professor Vanessa Sih, and Professor Jay Guo for serving on my dissertation committee.

My wife, Zhenxin, has been a constant inspiration during my graduate study. Her support and tolerance are indispensable for me to complete this dissertation. I am also grateful to my daughter, Annabelle, who has been growing up well in China. Lastly, I am deeply indebted to my parents for their inexhaustible patience, and the enormous effort they put into raising Annabelle.

Table of Contents

Acknowledgements.....	ii
List of Figures.....	vii
List of Tables.....	xi
List of Appendices.....	xii
Abstract.....	xiii
Chapter 1 Introduction to Organic Semiconductors.....	1
1.1 The Unique Features of Organic Semiconductors.....	1
1.2 Process and Deposition Techniques for Organic Materials.....	5
1.3 Organic Light Emitting Diodes.....	9
1.4 Organic Semiconductor Lasers.....	13
1.5 Organic Solar Cells.....	17
1.6 Organic Thin Film Transistors.....	19
Chapter 2 Physics of Organic Semiconductors.....	21
2.1 Electrical Properties of Organic Semiconductors.....	21
2.1.1 Charge Injection.....	21
2.1.2 Charge Transport.....	25

2.1.3 Charge Recombination.....	28
2.2 Photophysical Properties of Organic Semiconductors.....	28
2.2.1 Excitons: Types and Definitions.....	28
2.2.2 Exciton Transport.....	35
2.2.3 Exciton Interactions	38
2.3 Exciton Interactions in Organic Light Emitting Diodes	41
Chapter 3 Singlet-Triplet Annihilation in Fluorescent Organic Light Emitting Diodes .	44
3.1 Dynamics of Singlet-triplet Annihilation (STA)	44
3.2 Transient Electroluminescence Turn-on Decay Due to STA	48
3.3 Use of a Phosphorescent Dopant to Reduce STA.....	55
Chapter 4 Managing Triplets in Fluorescent OLEDs	58
4.1 Concept of Triplet Management	58
4.2 Suppressed EL Turn-on Decay through Triplet Management	60
4.3 Enhanced OLEDs Efficiency through Triplet Management.....	65
Chapter 5 Organic Semiconductor Lasers (OSLs) With a Continuous-wave Threshold	69
5.1 Theory for Continuous-wave (CW) Lasing in OSLs.....	70
5.2 Fabrication and Measurement of OSLs	73
5.3 Extended Lasing Duration in OSLs with Triplet Management	75
5.4 Observation of the CW Threshold in an OSL.....	82
Chapter 6 Triplet Contributions to Fluorescent OLED Efficiency.....	85

6.1 Fluorescent OLEDs with both STA and TTA	86
6.2 Evaluation of the Role of Triplets in Fluorescent OLEDs.....	94
Chapter 7 Triplet Annihilation in Phosphorescent OLEDs: Dexter-Mediated Triplet Diffusion	98
7.1 Transient Photoluminescence in Phosphorescent Emitters.....	99
7.2 Diffusion vs. Transfer Dominated Triplet Annihilation	106
7.3 Emitter Design for High Brightness PHOLEDs	110
Chapter 8 Controlling Triplet Dynamics to Extend the Operational Lifetime of Blue PHOLEDs	114
8.1 Blue PHOLEDs Operational Lifetime: an Introduction	115
8.2 Management of the Exciton Profile in PHOLEDs.....	118
8.3 Ten-fold Improvement in the Lifetime of Blue PHOLEDs	129
Chapter 9 Future Work	135
9.1 A Singlet Fission Organic Coating for Photovoltaics.....	135
9.2 Feasibility of an Electrically Pumped OSL	138
Appendix A Chemical Structures for Organic Molecules	142
Appendix B List of Publications, Conference Presentations and Patents.....	146
References.....	150

List of Figures

Figure 1.1 Structure of crystalline silicon and amorphous organic semiconductor tris(8-hydroxyquinoline) aluminum (Alq_3).....	2
Figure 1.2 Examples of curved and transparent OLEDs	3
Figure 1.3 Effect of material purity on OLED efficiency.....	5
Figure 1.4 Setup for gradient sublimation purification of organic materials.....	6
Figure 1.5 Setup and operation of vacuum thermal evaporation (VTE).....	6
Figure 1.6 Setup and operation of organic vapor phase deposition (OVPD)	8
Figure 1.7 Structure and operation of an OLED.....	10
Figure 1.8 Examples of OLED displays	11
Figure 1.9 Chemical structures of organic semiconductor laser materials	14
Figure 1.10 Three different feedback structures for OSLs	15
Figure 1.11 Structure and operation of an organic solar cell (OSC)	17
Figure 1.12 Curved OSCs installed on the bus shelters in San Francisco.	18
Figure 1.13 Basic structure of an organic thin film transistor (OTFT).....	19
Figure 1.14 Characteristics of an OTFT	20
Figure 2.1 Illustration of the barrier height for current injection from metal contact to organics.....	22
Figure 2.2 The current density-voltage (J-V) triangle (shaded) formed by three charge transport mechanisms in organics.....	27

Figure 2.3 Three type of excitons determined by their spatial extent.....	29
Figure 2.4 Ground state and excited state energies in the molecular configuration coordinate.....	30
Figure 2.5 Emission and absorption spectra of anthracene.....	32
Figure 2.6 Chemical structure and emission spectrum of platinum-octaethyl-phorphyrin (PtOEP).....	34
Figure 2.7 Annihilation between excitons considering both exciton diffusion and exciton-to-exciton energy transfer	39
Figure 2.8 Calculated EQE for a fluorescent OLED with STA, and a phosphorescent OLED with TTA.....	43
Figure 3.1 Structure of a bottom emitting OLED on glass substrate.....	45
Figure 3.2 Simulated exciton density dynamics	48
Figure 3.3 Structures for the red and blue emitting OLEDs.....	49
Figure 3.4 Setup for OLED efficiency and spectrum measurements	50
Figure 3.5 Transient electroluminescence (EL) of the devices.....	51
Figure 3.6 Recovery of the turn-on peaks under double pulse current injection.....	53
Figure 3.7 Delayed fluorescence from the devices.....	54
Figure 3.8 Electroluminescence transient of 1% Pt(TBPB) and 8% TBP co-doped with the host.....	56
Figure 4.1 Concept of the triplet management strategy.....	59
Figure 4.2 Photoluminescence (PL) spectra of ADN and Alq ₃ films, and EL spectra of OLEDs with DCM2 emitter.....	61
Figure 4.3 EL transients of OLEDs with various concentrations of ADN.....	63

Figure 4.4 EQE of triplet-managed OLEDs vs. of ADN concentration	66
Figure 4.5 EL transients and EQE for OLEDs with different rubrene concentrations	67
Figure 5.1 Calculated singlet density threshold and lasing duration	72
Figure 5.2 Atomic Force Microscope (AFM) images of the grating substrate.....	74
Figure 5.3 Interference lithography exposure setup using an Argon ion laser	75
Figure 5.4 Structure and operation of the organic semiconductor laser (OSLs)	76
Figure 5.5 PL, amplified spontaneous emission (ASE), and lasing spectra of 2 vol% DCM2 doped Alq ₃ thin film.	77
Figure 5.6 Probe pulse PL spectrum with and without the pump pulse	78
Figure 5.7 Absorption coefficient calculated for $x = 0$ and 70	78
Figure 5.8 PL and lasing transients measured at 1.6 kW/cm ² pump intensity.....	79
Figure 5.9 Lasing transients above the CW threshold	83
Figure 6.1 Energetics of a DBP doped rubrene mixture.....	88
Figure 6.2 EQE and charge balance factor vs. current density	89
Figure 6.3 EL turn-on and turn-off transients for the DBP doped rubrene OLED.....	90
Figure 6.4 Calculated singlet and triplet densities, ratios of the delayed fluorescence EL to total EL, and the ratio ξ of the effective triplet current density (J_T) to J	92
Figure 6.5 Ratio ξ vs. J , as a function of the STA rate k_{ST} and TTA rate k_{TT}	95
Figure 7.1 PL transients from 8% Ir(ppy) ₃ doped in CBP.....	104
Figure 7.2 Triplet absorption cross-section spectra for Ir(ppy) ₃ and PtOPE	106
Figure 7.3 Absorption and emission spectra of Ir(ppy) ₃ and PtOEP (open circle).....	107
Figure 7.4 Comparison between two triplet diffusion mechanisms	109
Figure 7.5 Absorption spectra of Ir(ppy) ₃ , Ir(ppy) ₂ acac, and PtOEP	111

Figure 7.6 Calculated PHOLED efficiency roll-off due to TTA.....	112
Figure 8.1 Illustration of triplet-polaron annihilation (TPA).....	117
Figure 8.2 Structures of the blue phosphorescent organic light emitting diodes (PHOLEDs).....	120
Figure 8.3 Performance characteristics of the blue PHOLEDs.	121
Figure 8.4 Ultraviolet photoelectron spectroscopy (UPS) data from molecules in the blue PHOLED emissive layer (EML).....	122
Figure 8.5 <i>J-V</i> characteristics of the hole-only and electron-only devices.	124
Figure 8.6 Energetics and exciton density profiles in the PHOLED EML.....	125
Figure 8.7 Emission spectra from probe devices for D2 at $J = 10 \text{ mA/cm}^2$ and parameters for calculating the exciton density profiles.....	127
Figure 8.8 Time evolution of the normalized luminance, L , of blue PHOLEDs and change in operating voltage ΔV	130
Figure 9.1 Structure and operation principle of the proposed singlet fission organic coating for photovoltaic applications.....	136
Figure 9.2 Calculated maximum power conversion efficiency (PCE) based on detailed balance theory.	137
Figure 9.3 Proposed structure for an OLED-pumped-OSL.....	138
Figure 9.4 Transient current density and emission from a blue emitting OLED.....	139

List of Tables

Table 1.1 A comparison of bulk physical properties between crystalline silicon and amorphous Alq ₃	2
Table 3.1 Fitting parameters for transient ELs from the OLEDs	52
Table 5.1 Parameters for the lasing threshold calculation in Figure 5.1.....	71
Table 5.2 Parameters for analyzing the PL and lasing transients	81
Table 7.1 Parameters for the PL transients fits using the diffusion and transfer models	105
Table 8.1 Commercial OLED efficiency and lifetime.....	115
Table 8.2 Common molecular bond energy [3].....	116
Table 8.3 Characteristics at $L_0 = 1000 \text{ cd/m}^2$ for blue emitting PHOLEDs*	123
Table 8.4 Lifetime fitting parameters for blue emitting PHOLEDs	132
Table 9.1 Literature report on low threshold OSLs	140

List of Appendices

Appendix A Chemical Structures for Organic Molecules	142
Appendix B List of Publications, Conference Presentations and Patents.....	146

Abstract

Over the past two decades, organic light emitting diodes (OLEDs) have been leading the research and development in organic semiconductors, and representing a primary driving force in information display as well as solid-state lighting innovations. In organic semiconductors, excitons (i.e. bound electron-hole pair excited states) are responsible for optical transitions, and are thus central to the operation of all organic optoelectronic devices. This dissertation aims at understanding the fundamental physics of exciton interactions and their effects on the performance of OLEDs. We show that managing exciton interactions based on exciton physics results in significantly improved device characteristics.

Organic light emitting diodes based on singlet (i.e. spin anti-symmetric) and triplet (spin symmetric) exciton emission are called fluorescent OLEDs and phosphorescent OLEDs (PHOLEDs), respectively. The first part of this dissertation studies exciton interactions in fluorescent OLEDs. We begin by identifying singlet-triplet annihilation (STA) as a loss mechanism in fluorescent efficiency, and thus propose a triplet management strategy to de-excite the detrimental non-emissive triplet. This strategy leads to more than 100% improvement in fluorescent OLED efficiencies, and also a more than 100-fold increase in lasing duration in organic semiconductor lasers (OSLs), thus allowing for the first observation of the continuous-wave threshold in OSLs.

Further, since triplet-triplet annihilation (TTA) contributes to fluorescent emission, we analyze the trade-off between STA and TTA, and propose optimal fluorescent material properties needed for high fluorescent efficiency.

The second part of this work focuses on exciton interactions in PHOLEDs. Triplet-triplet annihilation is studied through transient photoluminescence, and Dexter-type triplet diffusion is identified as the dominant mechanism leading to TTA. Thus, minimizing the Stokes shift between the molecular emission and absorption is introduced as a route leading to high efficiency PHOLEDs at high luminance. Indeed, exciton interactions are important for not only OLED efficiency but also operational lifetime. Based on the understanding that triplet-polaron annihilation (TPA) is a fundamental intrinsic degradation mechanism in blue PHOLEDs, we designed a novel OLED whose phosphorescent emitter concentration is varied linearly with position. This doping profile results in a low and uniform exciton density and thus a higher efficiency and suppressed TPA, leading to a significantly extended operational lifetime over conventional blue PHOLEDs.

Chapter 1

Introduction to Organic Semiconductors

In this chapter, we identify some unique features that distinguish organic semiconductors from conventional inorganic semiconductors. Following that, we discuss the process and deposition techniques for organic materials. Then, we cover four representative types of organic electronic devices: organic light emitting diodes (OLEDs), organic semiconductor lasers (OSLs), organic solar cells (OSCs), and organic field effect transistors (OFETs). Emphasis will be given to OLEDs and OSLs, as they illustrate background and provide motivation for this dissertation. This chapter is not intended as a comprehensive review of organic materials or devices, and readers interested in more details are referred to the references listed in each section.

1.1 The Unique Features of Organic Semiconductors

The building blocks of conventional inorganic semiconductors are atoms such as silicon (Si), germanium (Ge), gallium (Ga), and arsenic (As), which are covalently bonded to form ordered crystalline structures. In contrast, the building blocks of organic semiconductors are carbon-containing small molecules or polymers, which are bonded through weak van der Waals forces, and are often amorphous. Small organic molecules have well-defined molecular structures with a typical molecular weight of < 1000 , and

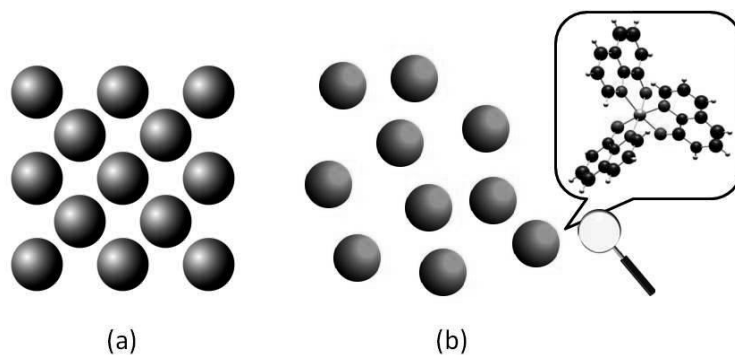


Figure 1.1 (a) Structure of crystalline silicon viewing from the [100] direction (b) Structure of amorphous organic semiconductor with the inset showing the chemical structure of tris(8-hydroxyquinoline) aluminum (Alq_3)

polymers are comprised of long chains of repeating molecular units without a definite molecular weight. This thesis is based on small molecules, which will also be the focus of this introduction.

Figure 1.1 shows a structural comparison between crystalline Si and an amorphous archetype small molecule, tris(8-hydroxyquinoline)aluminum (Alq_3). Compared to the periodic repeating unit cells in crystalline inorganic semiconductors, molecules in amorphous organic semiconductors are randomly distributed and oriented.

Table 1.1 A comparison of bulk physical properties between crystalline silicon and amorphous Alq_3

Physical properties	silicon	Alq_3
Density (g/cm^3)	2.33 [1]	1.51 [5]
Young's modulus (GPa)	~ 180 [7]	~ 1 [9]
Refractive index at 650 nm	3.85 [1]	1.72 [10]
Absorption coefficient (cm^{-1}) at 400 nm	1×10^5 [1]	4.5×10^4 [12]
Electron mobility ($\text{cm}^2\text{V}^{-1}\text{s}^{-1}$)	1400 [1]	$\sim 1 \times 10^{-5}$ [15]
Hole mobility ($\text{cm}^2\text{V}^{-1}\text{s}^{-1}$)	450 [1]	$\sim 5 \times 10^{-8}$ [15]

A comparison of their basic mechanical, optical, and electrical properties is given in Table 1.1.

Due to the low bonding strength and their resulting amorphous structure, organic thin films are “softer” than inorganic thin films for the same geometric size. For example, the Young’s modulus for crystalline Si is ~180 GPa compared to ~1 GPa for Alq₃ (Table 1.1). Such a unique feature of organics allows for curved [16], flexible [17-19], and stretchable [20-22] electronic and optoelectronic devices. For example, Fig. 1.2 (a) shows the curved smart phone released by Samsung in October 2013.

The oscillator strength (i.e. the probability of optical transitions) [23] of organics is significantly higher than inorganic semiconductors. This results in high absorption coefficient and luminescent quantum yield in organics desirable for optoelectronic applications [24]. Also notably, the optical refractive index for organics typically ranges from 1.5 to 2, as compared to > 3 for inorganic semiconductors. As a result of their low refractive index, organics are advantageous for developing optical devices such as transparent OLEDs [25] and photovoltaics [26]. For example, Fig. 1.2 (b) shows



Figure 1.2 (a) Samsung's Galaxy Round smart phone using a curved OLED display (b) A transparent OLED lighting panel manufactured by Phillips

transparent OLED light panels released by Philips.

Due to their morphologies, charge transport in amorphous organics is via hopping between localized molecular orbital levels [27], while in crystalline inorganic materials, charge transport is through delocalized energy bands [1]. Thus, the charge mobility in amorphous organic materials can be as much as 6 to 8 orders of magnitudes lower than that of crystalline inorganics. For example, the electron mobility for Si is $1400 \text{ cm}^2\text{V}^{-1}\text{s}^{-1}$, while for Alq_3 is approximately $1 \times 10^{-5} \text{ cm}^2\text{V}^{-1}\text{s}^{-1}$ (Table 1.1). Therefore, to achieve a reasonable operational voltage, the thickness of organic devices is often on the order of 100 nm, much thinner than their inorganic counterparts. Significantly higher charge mobility in organics has been achieved through crystalline structures [28-30]; however, a deposition technique for crystalline films compatible with a large number of organic molecules and also with adequate control of film thickness is yet to be demonstrated.

Another important but often undesired feature of organic materials is that they are generally air-sensitive which results from a combination of vulnerability of chemical reactions of organic molecules with oxygen and/or water, and ambient-induced film morphology changes. Therefore, hermetic packaging [31] is essential to ensure the long term reliability of organic devices. Interestingly, researchers have utilized the environmental sensitivity of organic devices in developing chemical sensors [32, 33].

1.2 Process and Deposition Techniques for Organic Materials

Purity of organic source materials used for devices is essential for achieving low impurity organic film growth [34]. Because impurities can act as both charge trapping and excited state quenching centers, low impurity films are important for achieving high device performance [35]. For example, Fig. 1.3 shows the OLED external quantum efficiency (EQE, defined by the ratio of the number of input electrons to the output photons from the OLED front surface) comparison between purified and unpurified rubrene host material, which differs by almost a factor of 2. The structure of the device is the same as reported in ref. [36] (also see Chapter 7).

Gradient sublimation is an effective and widely adopted method to purify small molecular weight organic materials [34]. The basic setup for gradient sublimation is shown in Fig. 1.4. Typically, a quartz boat is loaded with several grams of raw organic material available from a commercial source such as Sigma-Aldrich or Lumtec Taiwan. The boat is then positioned at the closed end of a long (~60 cm) quartz tube, followed by inserting two to three quartz sleeves in the middle of the tube. The tube is evacuated

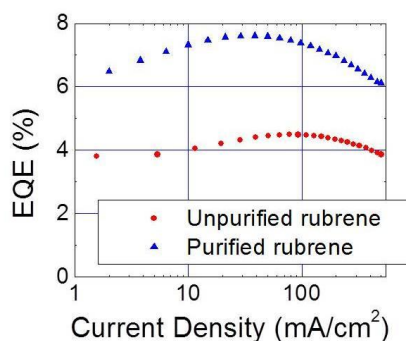


Figure 1.3 External quantum efficiency (EQE) as a function of current density of an OLED using rubrene as the host material in the emissive layer. There is a two-fold difference in EQE between the purified and unpurified rubrene.

through its open end using a two-stage mechanical and turbo pump combination to achieve pressure lower than 10^{-6} Torr. Subsequently, a horizontal three zone furnace is gradually ramped up, with a high temperature zone close to the quartz boat, an intermediate temperature zone near the sleeves, and a low temperature zone near the tube opening. Once sublimation of the organics is observed, the temperature of each zone is kept constant, typically ranging between 200°C and 500°C. The purification process usually lasts approximately one week. In the end, the purified organics crystallized on the

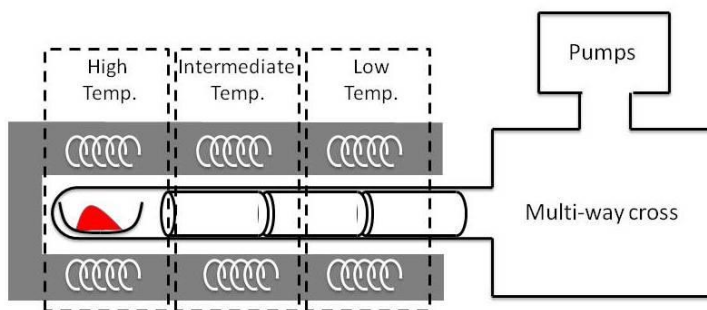


Figure 1.4 Setup for gradient sublimation purification of organic materials

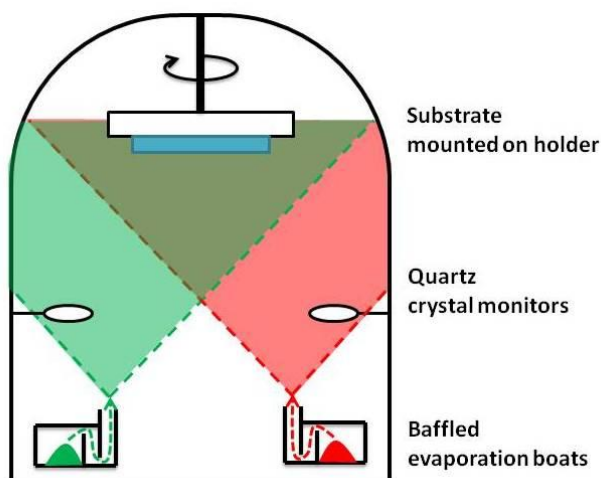


Figure 1.5 Setup and operation of vacuum thermal evaporation (VTE)

quartz sleeve are collected, while the volatile impurities condensed near the tube opening, and non-volatile impurities remaining in the boat are discarded.

A variety of deposition techniques are available for organic film deposition, including vacuum thermal evaporation (VTE) [24, 34, 37], organic vapor phase deposition (OVPD) [29, 38, 39], organic vapor jet print (OVJP) [40, 41], spin-cast, inkjet printing [42], physical vapor growth [28, 43], etc. Here, we will focus on VTE since all organic thin films and devices studied in this thesis were grown by this method. A brief discussion of OVPD and OVJP will be given since they are superior to VTE in terms of material utilization, film crystalline order tuning, and mask-free patterning.

Vacuum thermal evaporation is by far the most widely used organic film deposition technique for both research and large scale manufacturing purposes. As shown in Fig. 1.5, during VTE, organic source materials are loaded in a baffled evaporation boat made of tungsten or molybdenum positioned in the bottom of the vacuum chamber, and the substrate is placed at the top of the chamber facing down. Substrate rotation is usually enabled to achieve high film thickness uniformity. Quartz crystal monitors are used to read the film deposition rate, which also provide feedback to the current through the evaporation boat for deposition rate control. Multiple organic sources can be co-evaporated simultaneously, with individual crystal monitors to control the rate and thus the concentration of each. Pressure in the range of 10^{-6} - 10^{-7} Torr during deposition is required to achieve low impurity levels [34] necessary for device operation, and it has been shown that ultrahigh vacuum (with pressure $< 10^{-9}$ Torr) is beneficial for both OLED efficiency and reliability [35].

The material utilization efficiency (i.e. the weight ratio of material deposited on the substrate vs. all the evaporated material) is dependent on the geometry of both the substrate and the chamber. For example, in a VTE chamber typical for academic research, if a 3.5-inch-diameter substrate is 60 cm above the source, assuming a uniform source evaporation profile within 90° , the utilization efficiency is approximately 1%. In contrast, industrial VTE chambers often use in-line linear sources [44] and large area substrates (up to 1 m \times 1 m), resulting in $> 50\%$ utilization efficiency [45]. The VTE deposited film is typically amorphous, while high substrate temperature and low deposition rate can result in crystalline structures [34, 46] for some molecules.

As illustrated in Fig. 1.6, organic vapor phase deposition (OVPD) [38] is a deposition technique where the organics are first evaporated into a hot carrier gas, and then flow through a path with heated walls to reach a cooled substrate. Due to complete elimination of material deposition on the hot chamber walls, OVPD can potentially achieve higher materials utilization efficiency [39] than VTE. Note that the utilization

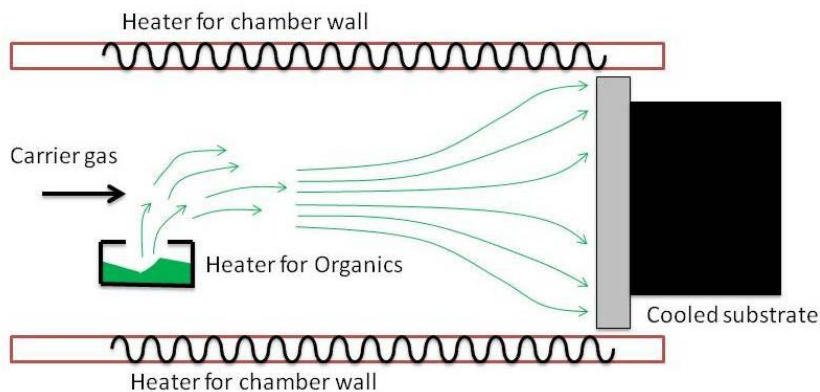


Figure 1.6 Setup and operation of organic vapor phase deposition (OVPD)

efficiency of OVPD also significantly depends on source and substrate geometry. In addition, a variety of crystalline film morphologies can be achieved through tuning the source temperature, carrier gas flow rate, chamber pressure and substrate temperature [29, 39].

Organic vapor jet printing (OVJP) [40] is a deposition technique based on the same principles as OVPD, where the principal difference is that the organic vapor reaches the cooled substrate surface through a heated nozzle. In contrast to the use of shadow masks in VTE for organic film patterning, OVJP growth can be directly patterned on the substrate with $<10\ \mu\text{m}$ resolution [41]. At the same time, OVJP offers superior material utilization efficiency because the deposition occurs in the near field with $< 1\ \text{mm}$ substrate-to-nozzle distance, and also there is no material loss due to shadow masks. Although industrial fabrication of organic devices (i.e. OLED displays and light panels) is presently solely through VTE, OVPD and OVJP have the potential to replace VTE in the near future.

1.3 Organic Light Emitting Diodes

Research on OLEDs can be dated back to half a century ago when electroluminescence from organic crystals was first observed. Most notably, in 1963, Pope et al. [47] observed light emission from 10-micron-thick tetracene doped anthracene crystals when the applied voltage was higher than 400 V, corresponding to $100\ \mu\text{A}/\text{cm}^2$ current density. During the 1970s and 1980s [37, 48-50], organic electroluminescence research gradually shifted from single crystals to polycrystalline and amorphous films. In particular, in 1987, the work of Tang and VanSlyke [37] on a bi-layer Alq_3 and 1-bis[4-

[N,N-di(4-tolyl)amino]phenyl]-cyclohexane (TAPC) device grown on an indium-tin-oxide (ITO) coated glass substrate marked the birth of modern OLED technology. The concept of the electron transport layer (ETL) and hole transport layer (HTL) in the Tang device is still used in state-of-the-art OLEDs today. The next giant leap in OLED technology happened in the late 1990s, when phosphorescent OLEDs were demonstrated by the groups led by Forrest and Thompson [51, 52], which led to OLEDs with ~100% internal quantum efficiency (IQE) [53].

Figure 1.7 illustrates the basic structure and operation of an OLED. Typically, a bottom emitting OLED is grown on transparent substrates such as glass or plastic, with an ITO anode, and an aluminum cathode on top. The organic layers sandwiched between the electrodes typically have a total thickness of 100-200 nm. During operation (i.e. when current is turned on), holes are injected from ITO and transported through the HTL to

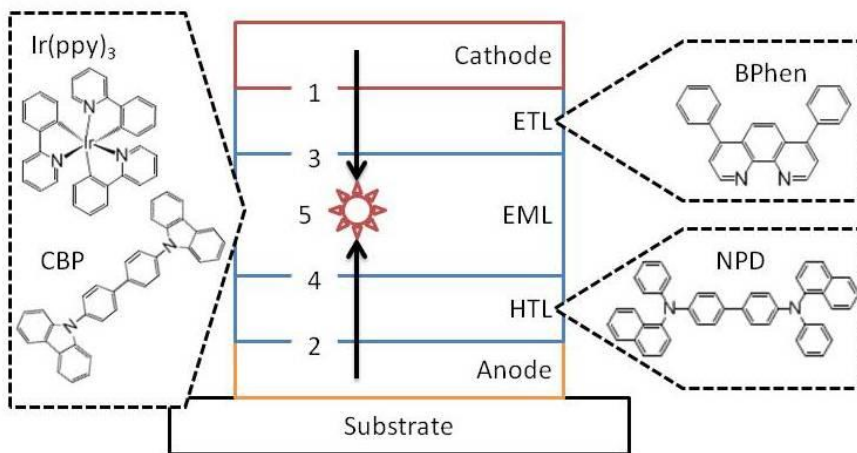


Figure 1.7 Structure and operation of an organic light emitting diode (OLED) consisting of an anode, a hole transport layer (HTL), a emissive layer (EML), an electron transport layer (ETL), and a cathode. The arrows show representative organic molecules used for different layers. The processes of 1-5 are electron injection, hole injection, electron transport, hole transport, and electron-hole recombination, respectively.

reach the emissive layer (EML); electrons are injected from aluminum and transported through the ETL to reach the EML. When an electron and a hole reach each other inside the EML, they combine to form a bound excited state called exciton. OLED emission results from radiative decay of the excitons.

Depending on the total spin quantum number of the exciton, it is either a triplet (spin number = 1) or a singlet (spin number = 0), and the formation ratio of singlets vs. triplets was shown to be 1 vs. 3 [54, 55], following the spin degeneracy statistics. OLEDs utilizing singlets for emission are called fluorescent OLEDs, in which triplet transitions are spin forbidden and hence non-emissive. Therefore, the maximum internal quantum efficiency, IQE (i.e. the ratio of the number of the input electrons and the generated photons) of fluorescent OLEDs is only 25%. Recently, it was discovered that by utilizing



Figure 1.8 (a) A prototype flexible phone from LG, (b) A tablet computer from Samsung, (c) A smart watch from Samsung, (d) A TV from LG. All these electronic devices use OLED displays.

triplet-triplet annihilation, the theoretical limit of fluorescent OLED IQE can, in principal, be increased to 62.5% [36, 56, 57], which will be discussed in detail in Chapter 6. OLEDs utilizing triplets for emission are called phosphorescent OLEDs in which singlets undergo rapid intersystem crossing to form triplets; thus, the theoretical maximum IQE of phosphorescent OLEDs is 100% [51-53]. After the demonstration of phosphorescent OLEDs, it was shown that phosphorescence-sensitized fluorescent OLEDs could also reach 100% IQE [58, 59].

OLEDs are by far the most widely used organic electronic devices, and the main applications are divided into displays and lighting. It is worth noting that all commercial OLEDs are based on small molecules rather than polymers due to their superior efficiency and operational stability.

As shown in Figure 1.8, OLED displays have been adopted in mobile phones, electronic tablets, watches, cameras, computer monitors, TV screens, etc. According to DisplaySearch (<http://www.displaysearch.com/>), the global market of OLED displays was \$8 billion in 2013, with mobile displays making up well more than half of the revenue. The most well-known OLED displays are the ones used in Galaxy smart phones made by Samsung. The advantages of OLED displays over conventional liquid crystal displays (LCDs) include light weight, high contrast ratio, fast response, large color gamut [60] (especially for the green sub-pixel), high mechanical flexibility, and low power consumption. However, the drawbacks for OLED displays compared to LCDs include high fabrication cost and limited operational lifetime. The lifetime issue for OLEDs is most significant for blue phosphorescent emission (among red, green and blue sub-pixels for displays), and in Chapter 8, we will show that significant improvement in blue

phosphorescent OLEDs lifetime can be achieved by a combined material and device architecture approach.

Compared to OLED displays, OLED lighting is still gaining momentum to be fully commercialized. In comparison to its strong competitor, LED lighting, OLED illumination has the advantage of mechanical flexibility, low heat generation, and color tunability. Although the high cost of the OLED light panel is the main hurdle for its wide application, the fabrication cost can significantly decrease with the increase of manufacturing scale. Both OLED and LED lighting panels have superior power efficiency [61], environmental impact (i.e. material toxicity), operational lifetime, as well as color purity when compared to conventional incandescent or fluorescent lighting.

One interesting but undesired feature of OLED operation is that its efficiency decreases as the output luminance increases, often called efficiency roll-off. Although inorganic LEDs also suffer efficiency roll-off [62], the on-set current density for roll-off is much higher ($> 10 \text{ A/cm}^2$) for inorganic LEDs than for OLEDs ($\sim 0.1 \text{ A/cm}^2$). Note that the OLED efficiency roll-off can be compensated by a large emissive area, which is difficult to achieve using inorganic LEDs. A significant portion of this thesis (i.e. Chapters 3, 4, 6, and 7) is devoted to understanding the physics related to such a phenomenon and pursuing solutions.

1.4 Organic Semiconductor Lasers

Similar to OLEDs, research on organic semiconductor lasers (OSLs) has a long history. The first demonstration of an optically pumped organic liquid dye laser was by

Sorokin et al. at IBM Watson Research Center in 1966 in chloro-aluminum phthalocyanine (ClAlPc), only 6 years after the first demonstration of the ruby crystal laser. Liquid dye lasers have the advantage of wavelength tunability, low cost, self-repairable (due to liquid circulation), and the capability of achieving ultrafast pulses (<10 fs). However, the disadvantages are the operational lifetime of dyes (which require frequent change of dye and solution), and their toxicity.

Significant breakthroughs in organic thin film lasers occurred in the 1990s, when amplified spontaneous emissions (ASE) were demonstrated by Heeger's group and Friend's group using poly-phenylenevinylene (PPV) [63, 64], and unequivocal lasing was reported by Forrest's group using Alq₃ doped with 4-(dicyanomethylene)-2-methyl-6-(4-dimethylaminostyryl)-4H-pyran (DCM) [65]. Because these materials systems are organic semiconductors, these organic lasers are also called organic semiconductor lasers (OSLs) [66]. In all cases, they required an optical pump. In the late 1990s and early 2000s, organic thin film laser researchers were encouraged by the rapid development of OLEDs, and it was envisioned that an electrically pumped OSL would soon be demonstrated [67, 68]. Unfortunately, it has not yet been demonstrated to date. In

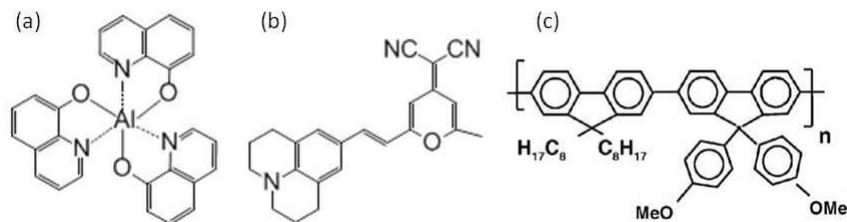


Figure 1.9 Chemical structures of organic semiconductor laser materials: (a) Alq₃, (b) 4-(dicyanomethylene)-2-methyl-6-julolidyl-9-enyl-4H-pyran (DCM2), and (c) poly[9,9-dioctylfluorene-co-9,9-di(4-methoxyphenyl)fluorene] (F8DP)

Chapters 5 and 9, we will discuss the difficulties in achieving an electrically pumped OSL, and our effort towards its demonstration.

Two essential components of any laser are the gain medium and the feedback structure. In Fig. 1.9, we show common organic semiconductor lasing materials. Alq₃ (Fig. 1.9 (a)) doped 4-(dicyanomethylene)-2-methyl-6-julolidyl-9-enyl-4H-pyran (DCM2, Fig. 1.9 (b)) were among the earliest demonstrated OSL systems [10]. Figure 1.9 (c) shows poly[9,9-dioctylfluorene-co-9,9-di(4-methoxy-phenyl)fluorene] (F8DP) [13], which holds the lowest reported threshold record among all OSLs of 36 nJ/cm². The optical gain from OSL materials originates from the population inversion in a four-level system made arising from the vibronic levels in the singlet excited state and the ground state. The physics leading to laser action will be discussed in Chapter 2.

Figure 1.10 shows common feedback structures for OSLs. The planar waveguide structure (Fig. 1.10 (a)) depends on reflections from the organic film and air interface to

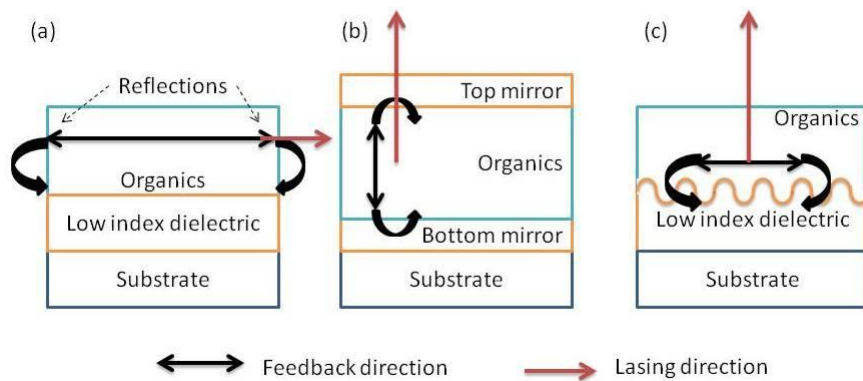


Figure 1.10 Three different feedback structures for OSLs: (a) planar waveguide, (b) vertical cavity, and (c) distributed feedback. The black arrows show feedback directions and the red arrows show lasing (i.e. out-coupling) direction.

provide feedback, leading to an edge emitting device. It typically has a high lasing quantum efficiency (>70% was demonstrated by the Forrest group [65]) due to its multimode nature. The vertical cavity structure (Fig. 1.10 (b)) depends on the top and bottom mirrors (using silver or dielectrics) for feedback, and is thus surface emitting. The feedback mechanism in a distributed feedback (DFB) structure (Fig. 1.10 (c)) is diffraction from an integrated grating, which can be conveniently fabricated through interference lithography [69] (see Chapter 5). Depending on the diffraction order, the emission from DFB lasers can be either from the surface or from the edge.

Conventional optically pumped OSLs require a pump pulse shorter than 20 ns, which is caused by the temporal increase of losses associated with the non-emissive triplet excitons. Giebink et al. [4] and Lehnhardt et al. [70] studied the transient intensities of OSLs pumped by long pulses (>100 ns), and found that both triplet absorption and interactions between singlets and triplets limits the OSL operation to only the nanosecond pulsed mode. In Chapter 5 we will show that such triplet induced losses can be suppressed through the mixing of “triplet manager” [71] molecules into the gain medium. Furthermore, we theoretically demonstrate that a continuous-wave operation regime exists for OSLs, which is supported by the transient emission data from OSLs using “triplet managers”.

1.5 Organic Solar Cells

At approximately the same time when Tang et al. published the first OLED structure with respectable efficiency (i.e. approximately 1% EQE), another work from Tang reported an organic thin film solar cell with 1% power conversion efficiency (PCE, defined as the ratio of the maximum generated electrical power to the incident solar power) [72]. The reported solar cell employed a bi-layer donor-acceptor type of heterojunction, where excitons split into electrons and holes at the bi-layer interface, thus generating current. After nearly 30 years of research, still using the same donor-acceptor concept, PCEs close to or higher than 11% have been achieved in organic solar cells (OSCs) using either small molecules or polymers [73, 74].

As illustrated in Fig. 1.11, the basic structure [72] of a planar OSC includes an ITO anode, an electron donor layer, an electron acceptor layer, and a cathode. The

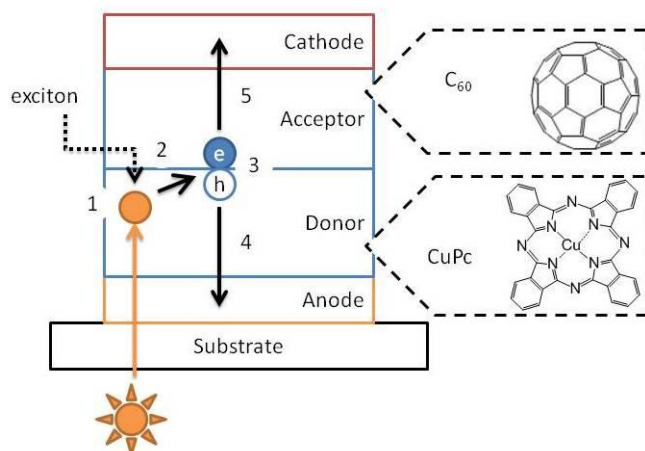


Figure 1.11 Structure and operation of an organic solar cell (OSC) made of donor and acceptor bi-layer organics, the arrows show representative organic molecules used for donors and acceptors. The processes of 1-5 are photon absorption (or exciton formation), exciton diffusion, exciton splitting, hole diffusion, and electron diffusion, respectively.

operation of OSCs can be regarded as the inverse process of OLED operation. Sunlight incident from the transparent ITO side is absorbed by the donor and acceptor layers. Excitons are formed following absorption, which diffuse to the donor-acceptor interface and split into electrons and holes that are subsequently collected at the electrodes.

For the same reason (i.e. high structural disorder) as low charge mobility mentioned in Section 1.1, the exciton diffusion length in organics is also low, leading to loss of excitons in planar OSCs. Use of bulk and nanocrystalline mixed heterojunctions (i.e. comprised of a mixed donor and acceptor layer) [75, 76] moves the exciton splitting interface closer to the exciton generation site, and thereby eliminates the need for long diffusion. This has been shown effective in yielding higher PCEs.

Wide commercialization of OSCs is still challenging due to their low efficiency, short operational lifetime, and high cost compared to inorganic solar cells. However, the unique features of OSCs such as their mechanical flexibility and optical transparency can potentially push OSCs to the market and fill roles that inorganic solar cells cannot accomplish. For example, Fig. 1.12 shows curved organic solar panels installed in bus



Figure 1.12 Curved OSCs installed on the bus shelters in San Francisco.

shelters in San Francisco.

1.6 Organic Thin Film Transistors

The first organic thin film transistor (OTFT) was demonstrated by Tsumura et al. [77] in 1986 using a polythiophene thin film with a carrier mobility of $10^{-5} \text{ cm}^2\text{V}^{-1}\text{s}^{-1}$ and a current on-off ratio of less than three orders of magnitudes. Through use of crystalline organic thin films, the performance of OTFTs can surpass that of amorphous silicon, with the calculated carrier mobility as high as $10 \text{ cm}^2\text{V}^{-1}\text{s}^{-1}$ (note that these high mobilities are likely due to charge transport on organic surface and can differ significantly from organic bulk mobilities) [28, 78] and the current on-off ratio larger than 10^8 [79].

The basic structure of an OTFT and the representative organic molecules used are shown in Fig. 1.13. The current-voltage relationship between the drain and source electrodes ($I_{DS}-V_{DS}$) of an OTFT can be modulated by the voltage applied through the gate and source electrodes (V_{GS}). As illustrated in Fig. 1.14 (left), the $I_{DS}-V_{DS}$

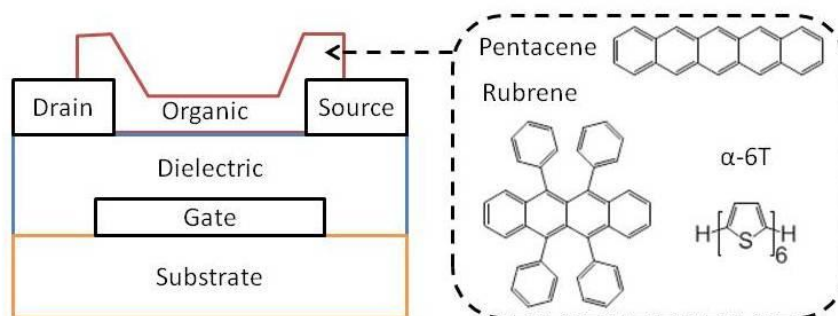


Figure 1.13 Basic structure of an organic thin film transistor (OTFT), and common organic molecules used in OTFTs, pentacene, rubrene, and alpha-sixithiophene (α -6T).

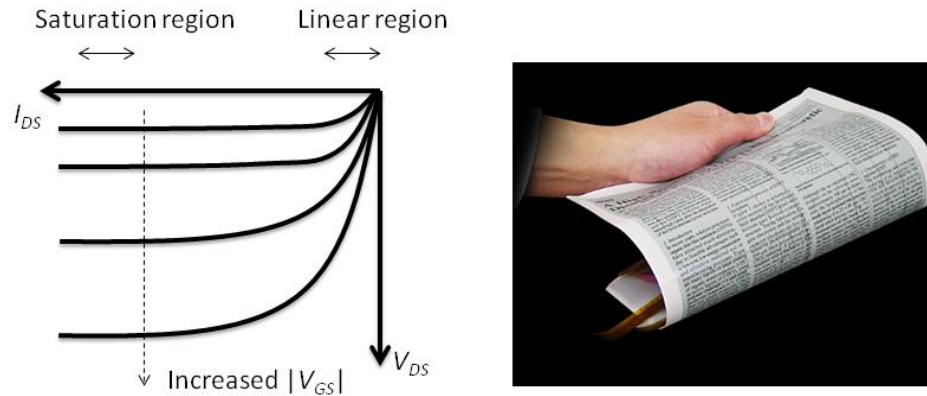


Figure 1.14 (left) Drain-source current-voltage characteristics (I_{DS} - V_{DS}) modulated by the gate-source voltage (V_{GS}) (right) An electronic paper prototype by SONY.

characteristics of a transistor are typically divided into a linear region and a saturation region. The linear region (when $V_{DS} < V_{GS}$) is a result of Ohm's law, and the saturation region (when $V_{DS} \approx V_{GS}$) happens when the electric field near the drain electrode vanishes and the accumulation region width approaches zero [1]. Transistors typically operate in the saturation region when I_{DS} is solely modulated by V_{GS} .

Compared to inorganic thin film transistors, OTFTs have advantages in terms of cost and mechanical flexibility; however, the reliability [80] and carrier mobility in OTFTs still need improvement in order to compete with inorganic transistors. Applications of OTFTs include the backplanes for flexible and/or transparent OLED displays, radio frequency identification tags (RFID), chemical sensors, etc. Another interesting application of OTFTs is to make electronic paper (Fig. 1.14 (right)) [81], where the switch of OTFTs controls the status of electronic ink capsules, and thus the color of the pixels.

Chapter 2

Physics of Organic Semiconductors

Following the introduction to the general features of organic semiconductors, their processing techniques, and applications in Chapter 1, we discuss in this chapter the physics of organic semiconductors. This chapter is divided into three sections. In Section 2.1, we discuss the electrical properties of organic semiconductors, covering the processes of charge injection, transport, and recombination. In Section 2.2, we focus on the photophysics of organic materials, covering the concepts of excitons, exciton transfer, and exciton interactions. In Section 2.3, the influence of exciton interactions on OLED efficiency is discussed.

2.1 Electrical Properties of Organic Semiconductors

2.1.1 Charge Injection

The electron and hole transport states in organic semiconductors are called the LUMO (lowest unoccupied molecular orbital) and HOMO (highest occupied molecular orbital) respectively. The absolute values of the orbital energies are referenced to the vacuum energy level. Ultraviolet photoelectron spectroscopy (UPS) and inverse photoelectron spectroscopy (IPES) [82, 83] can be used to measure the HOMO (E_{HOMO})

and LUMO (E_{LUMO}) energies respectively. Molecular orbital energy levels are conceptually comparable to the conduction and valence band extrema in inorganic semiconductors; however, it is worth noting that intrinsic organic semiconductors have a very low free carrier concentration ($< 10^5 \text{ cm}^{-3}$) due to the large bandgap ($E_{LUMO} - E_{HOMO} > 2 \text{ eV}$). Moreover, due to film morphology, disorder and interactions between charges and their local environments (for example, phonons or molecular dipoles), molecular orbitals are highly localized [84].

Charge injection in organics is the process of charge moving from the Fermi surface of the metal electrodes to the frontier molecular orbitals of an organic semiconductor. As shown in Fig. 2.1 (a), an electron injected from the metal Fermi level, E_F into the organic LUMO level, E_{LUMO} , needs to overcome a built-in barrier height of $\Delta V = E_{LUMO} - E_F$. The earliest physical model for such type of injection is thermionic emission described by Richardson [85]:

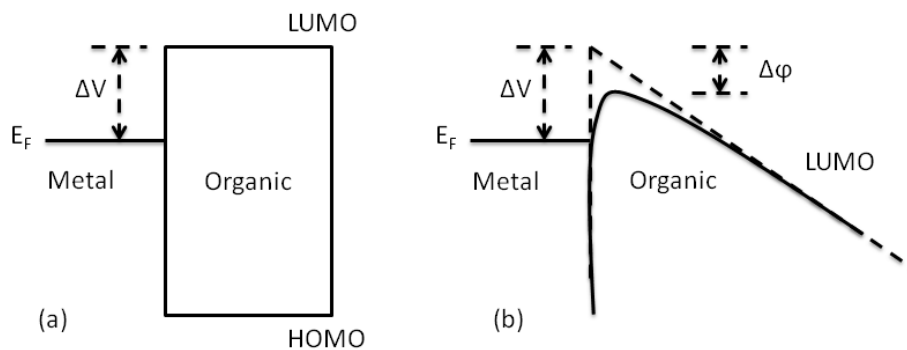


Figure 2.1 (a) Illustration of the barrier height for current injection from metal contact to organics (b) Barrier height reduction due to the interfacial electric field

$$J = \frac{em_e}{2\rho^2\hbar^3}(k_B T)^2 \exp\left[-\frac{DV}{k_B T}\right], \quad (2.1)$$

where J is the current density, e is the electron charge, m_e is the electron mass, k_B is the Boltzmann constant, \hbar is the reduced Planck's constant, and T is the temperature.

The Richardson model was later improved by Schottky [86] to include the effect of barrier height reduction, $\Delta\phi$, due to the interface electric field (Fig. 2.1 (b)). Emtage et al. [87] further derived expressions relevant to insulators (or organic semiconductors) with low charge mobility, which simplifies to the following equations under the limit of low electric field and high electric field respectively:

$$J_{low} = N_e \mu \exp\left(-\frac{\Delta V}{k_B T}\right) eF \quad (2.2)$$

$$J_{high} = N_e \mu \sqrt{\frac{k_B T}{\pi}} (4eF^3 \varepsilon)^{1/4} \exp\left[-\frac{\Delta V - \Delta\phi}{k_B T}\right] \quad (2.3)$$

where N_e is the electron density of states, μ is the mobility, F is the electric field at the metal/insulator interface, and ε is the dielectric constant of the insulator.

More recent improvements of the thermionic emission model relevant to the injection into organics was from Scott and Malliaras [88], which included an organic-to-metal interface reverse recombination current in addition to the metal-to-organic injection current. This model was later used to understand charge injection in OLEDs [89, 90].

Besides thermionic emission, another method for modeling current injection in organics is by Fowler and Nordheim [91] of electron tunneling through the injection

barrier. Fowler-Nordheim tunneling results directly from solving Schrödinger's equation for a triangular barrier,

$$J_{FN} = BE^2 \exp \left[-\frac{4\sqrt{2m}(\Delta V)^{3/2}}{3\hbar eF} \right] \quad (2.4)$$

where B is a tunneling pre-factor. This model was also successfully applied to modeling charge injection OLEDs [92, 93]; however, the barrier reduction effect due to the interface electric field is not considered by Eq. (2.4), which could cause significant overestimate of the tunneling efficiency.

The drawback for applying the thermionic emission or tunneling model is that neither considers the energetic disorder in organic semiconductors. To include such disorder in organics, Arkhipov et al. [94] and Baldo et al. [95] considered the Gaussian distribution of the molecular orbital energies, and the Miller-Abraham type [96] hopping between the metal and organic interface,

$$R(\Delta V) = \begin{cases} A_0 \exp\left(-\frac{\Delta V}{k_B T}\right) & \Delta V > 0 \\ A_0 & \Delta V \leq 0 \end{cases} \quad (2.5)$$

where R is the hopping probability between sites with an energy barrier of ΔV , and A_0 is the maximum hopping rate determined by the molecular orbital overlap. Then, the total injection current density is the integral over all possible states,

$$J = \int_{-\infty}^{+\infty} dU_I \int_{-\infty}^{+\infty} dU_o f(U_I) \exp \left[-\frac{1}{2} \left(\frac{U_I}{\sigma_I} \right)^2 - \frac{1}{2} \left(\frac{U_o}{\sigma_o} \right)^2 \right] \times R(U_o - U_I - aeF) \quad (2.6)$$

where U_I and U_o are the disorder energies of the metal-organic interface states, and the organic bulk respectively, σ_I and σ_o are the standard deviations of the Gaussian energy distributions, f is the distribution of the interface states, and a is the average intermolecular spacing. By modeling the J - V characteristics in a broad selection of organic semiconductors and temperature range using Eq. (2.6), Baldo et al. [95] suggested that the current density in organics is often limited by interface injection rather than organic bulk transport. However, mechanisms determining the J - V characteristics in organics are still under intense research investigation.

2.1.2 Charge Transport

When a molecule in organics is charged, due to both electron-phonon coupling and the polarization of the surrounding molecules by the charge, its configuration is distorted and energy is relaxed to a lower level than its molecular orbital energy [47]. This newly formed quasi-particle is called a polaron, and charge transport in organics is through polaron hopping between discrete molecular sites.

The earliest model for charge transport in organics was the space charge limited current (SCLC) model introduced by Mott and Gurney [97], and Rose [98], which assumed the charge injection from electrodes into organics is efficient (i.e. the contact is Ohmic). The derivation of the SCLC J - V relation starts from the Ohm's law and Gauss's law,

$$J = e\rho\mu F \tag{2.7}$$

$$\frac{dF}{dx} = \frac{ep}{\epsilon_r \epsilon_0} \quad (2.8)$$

where p is the hole density (and the same expression applies to the electron density n), ϵ_r is the relative permittivity of the insulator, and ϵ_0 is the vacuum permittivity.

Integrating Eq. (2.7) after plugging in Eq. (2.8) yields,

$$\int \frac{J}{\epsilon_r \epsilon_0 \mu} dx = \int F dF \rightarrow F = \sqrt{\frac{2xJ}{\epsilon_r \epsilon_0 \mu}}. \quad (2.9)$$

Then, integrating one more time yields the quadratic Mott-Gurney J-V relationship,

$$\int F dx = \int \sqrt{\frac{2xJ}{\epsilon_r \epsilon_0 \mu}} dx \rightarrow J_{SCLC} = \frac{9}{8} \frac{\epsilon_r \epsilon_0 \mu}{d^3} V^2. \quad (2.10)$$

If there are trap states within the bandgap of the organics which have an exponential distribution in energy, $N_T(E)$ relative to the molecular orbital energies (for example, LUMO),

$$N_T(E) = \frac{N_{LUMO}}{k_B T_T} \exp\left(\frac{E - E_{LUMO}}{k_B T_T}\right) \quad (2.11)$$

where N_{LUMO} is the trap density at the LUMO energy, T_T is a trap distribution temperature, Rose also derived the following expression for trapped charge limited current (TCLC).

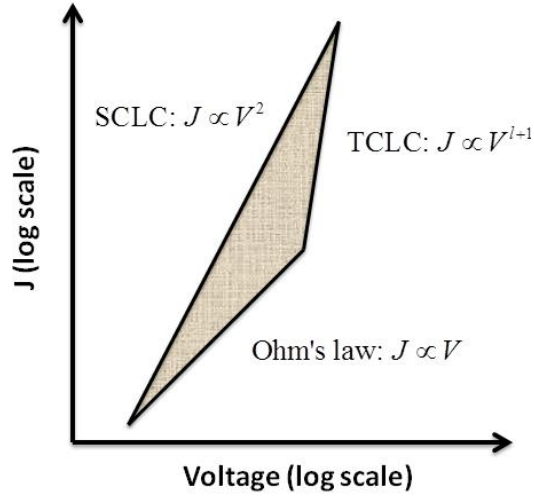


Figure 2.2 The current density-voltage (J-V) triangle (shaded) formed by three charge transport mechanisms in organics: Ohm's law, space charge limited current (SCLC), and trapped charge limited current (TCLC)

$$J_{TCLC} = q\mu N_c \left(\frac{\epsilon_r \epsilon_0 l}{qN_{LUMO}} \right)^l \frac{(2l+1)^{l+1}}{(l+1)^{2l+1}} \frac{V^{l+1}}{d^{2l+1}} \quad (2.12)$$

where N_c is the density of states at the LUMO energy, and $l = T_r / T$. Equation (2.12) was applied to a large selection of organic materials [99-103], with the factor l typically in the range of 6-10.

Interestingly, it was pointed out by Lampert [104] that the J - V characteristic of insulators with Ohmic contacts is confined to a triangular area illustrated in Fig. 2.2 (when both the J and V axes are in a log scale) defined by three limiting curves: Ohm's law, SCLC, and TCLC. This theory has been routinely and successfully applied to organic semiconductors [105, 106].

2.1.3 Charge Recombination

Charge recombination occurs when the electrons and holes coexist in the same spatial location but at their respective energies. The recombination rate, R , in organics is generally modeled following the treatment of Langevin assuming that electrons and holes move towards each other under the influence of their mutual Coulomb interaction,

$$R = \frac{e(\mu_n + \mu_p)}{\varepsilon_0 \varepsilon_r} np = k_L np \quad (2.13)$$

where μ_n and μ_p are electron and hole mobilities, respectively, and k_L is the Langevin recombination rate. Following recombination, the electron and hole form a bound excited state, or exciton, which plays a central role in the photophysical properties of organic semiconductors.

2.2 Photophysical Properties of Organic Semiconductors

2.2.1 Excitons: Types and Definitions

When organic molecules are excited, an electron from the HOMO is promoted to the LUMO, leaving a hole in the HOMO, and the resulting electron-hole pair is bound through Coulomb interaction to form an exciton.

As shown in Fig. 2.3, depending on the spatial extent of excitons, they can be divided in three different types [107, 108]: Frenkel excitons, charger transfer excitons, and Wannier-Mott excitons. The most common excitons in amorphous semiconductors are of the Frenkel type, which has the most localized (usually confined to a single

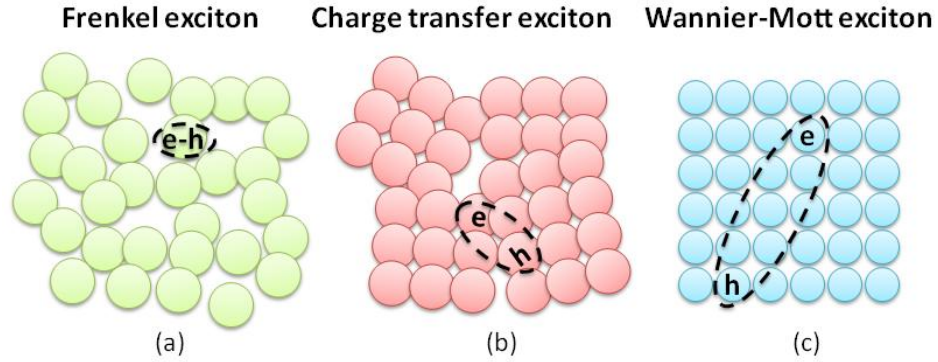


Figure 2.3 Three type of excitons determined by their spatial extent.

molecule) wave function and the highest binding energy E_b (~ 1 eV) among the three. Charge transfer excitons have a broader spatial extent than Frenkel excitons, and are often reported in organics with local crystalline order [47]. Frenkel and charge transfer excitons may also exist in the same organic material [109]. The delocalized Wannier-Mott exciton has a small E_b (< 10 meV), and is generally observed in high dielectric constant crystalline inorganic semiconductors.

The energy of an exciton relative to the molecular ground state can be solved through its Hamiltonian, H_{ex} , which is the summation between the single excited electron Hamiltonian H_e , and the electron-electron interaction, U_{ee} ,

$$H_{ex} = H_e + U_{ee} = T_e + U_e + U_{ee} \quad (2.14)$$

where T_e and U_e are the single electron kinetic and potential energies, respectively. Under the Born-Oppenheimer approximation [110], H_e can be calculated by solving the electron energy in a stationary molecular nuclear configuration. The discrete eigen-energies of H_e for the molecular ground and excited states in the configuration coordinate scheme [110] are illustrated in Fig. 2.4. The energy spacings between the eigen-energies in the same

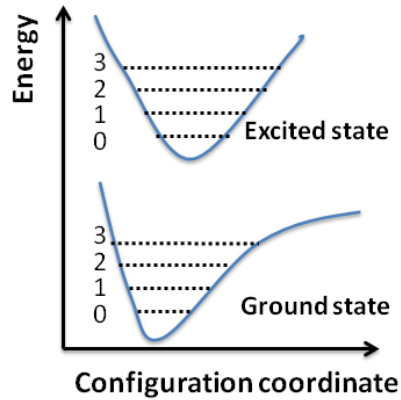


Figure 2.4 Ground state and excited state energies in the molecular configuration coordinate. The numbers (0-3) are the indexes for different vibronic states.

state are approximately the same due to the parabolic shape in U_e close to the energy minimum.

The interaction in Eq. (2.14) is given by $U_{ee} = \frac{1}{4\pi\epsilon_0} \frac{e}{r_{12}}$, where r_{12} is spatial

separation between the excited electron in the LUMO and the unpaired electron left in the HOMO. Then, the eigen-energies for U_{ee} can be calculated through $E_{ee} = \langle \psi | U_{ee} | \psi \rangle$, where ψ is the spatial wave function of the two-electron system.

Depending on the symmetry of the spin wave functions, excitons can be either spin anti-symmetric singlets or spin symmetric triplets. The total wave function of an exciton is the product of the spin wave function and the spatial wave function. Since electrons are Fermions whose total wave function is anti-symmetric, the singlet spatial wave function ψ_S is symmetric and the triplet spatial wave function ψ_T is anti-symmetric:

$$\begin{aligned}\psi_S &= \frac{1}{\sqrt{2}} [\phi_{HOMO}(1)\phi_{LUMO}(2) - \phi_{HOMO}(2)\phi_{LUMO}(1)] \\ \psi_T &= \frac{1}{\sqrt{2}} [\phi_{HOMO}(1)\phi_{LUMO}(2) + \phi_{HOMO}(2)\phi_{LUMO}(1)]\end{aligned}\tag{2.15}$$

where ϕ_{HOMO} and ϕ_{LUMO} are the wave functions for the HOMO and LUMO respectively, and 1 and 2 are indices for the two electrons. Thus, interaction energies for singlets (E_S) and triplets (E_T) are

$$E_S = \frac{e}{4\pi\epsilon_0} \left\langle \psi_S \left| \frac{1}{r_{12}} \right| \psi_S \right\rangle = J + K\tag{2.16}$$

and
$$E_T = \frac{e}{4\pi\epsilon_0} \left\langle \psi_T \left| \frac{1}{r_{12}} \right| \psi_T \right\rangle = J - K\tag{2.17}$$

where J and K are the Coulomb and exchange energies, respectively:

$$J = \frac{e^2}{4\pi\epsilon_0} \left\langle \psi_{HOMO}(1)\psi_{LUMO}(2) \left| \frac{1}{r_{12}} \right| \psi_{HOMO}(1)\psi_{LUMO}(2) \right\rangle\tag{2.18}$$

$$K = \frac{e^2}{4\pi\epsilon_0} \left\langle \psi_{HOMO}(1)\psi_{LUMO}(2) \left| \frac{1}{r_{12}} \right| \psi_{HOMO}(2)\psi_{LUMO}(1) \right\rangle.\tag{2.19}$$

Therefore, the molecular singlet energy is higher than triplet by $2K$.

Optical transition (i.e. absorption and emission) rates in organics can then be calculated through dipole transitions between a molecular ground state and excited state using the Fermi's Golden rule,

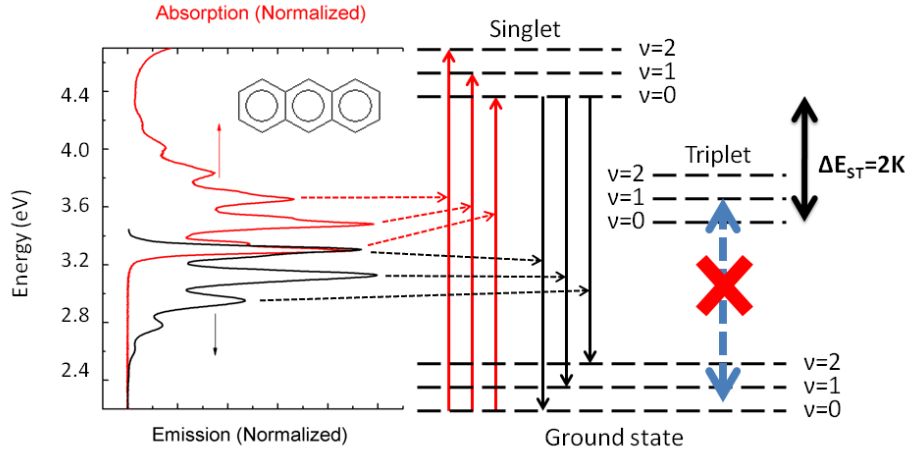


Figure 2.5 (left) Emission and absorption spectra of a prototype fluorescent molecule, anthracene (the chemical structure is shown in the inset) dissolved in cyclohexane, and the corresponding transitions (right) between the singlet excited state and ground state. The energy of triplet is lower than singlet by $\Delta E_{ST} = 2K$ (see Eq. (2.19)), and the triplet is non-emissive.

$$\begin{aligned} \Gamma &= \frac{2\pi}{3\hbar} \left| \langle \psi_f S_f | H | \psi_i S_i \rangle \right|^2 \rho(E_f) \\ &= \frac{2\pi}{3\hbar} F^2 \left| \langle S_f | S_i \rangle \right|^2 \left| \langle \psi_f | d | \psi_i \rangle \right|^2 \rho(E_f) \end{aligned} \quad (2.20)$$

where S_i and S_f are the spin wave functions of the initial and final states, ψ_i and ψ_f are the spatial wave functions of the initial and final states, $\widehat{H} = \widehat{d}F$ is the transition Hamiltonian, where \widehat{d} is the dipole moment, and $\rho(E_f)$ is the density of the final state with the energy E_f . Clearly, the spin symmetries of the initial and final states need to be the same for Γ to be non-zero, which is called the dipole transition selection rule. Because most molecules have a spin symmetric ground state due to the filled HOMOs, only singlet excitons are responsible for absorption and emission in fluorescent organic molecules. The absorption and emission processes in an archetype organic molecule

anthracene are illustrated in Fig. 2.5, and the vibronic spectral peaks are explained by transitions between discrete levels in the ground and singlet excited states.

Early demonstrations of OLEDs [37] were based on fluorescent emission from singlets; however, electron-hole recombination in OLEDs forms both singlets and triplets with a ratio of 1:3 [55] determined by the spin degeneracy. Since triplets are non-emissive due to the dipole transition selection rule, the maximum internal quantum efficiency (*IQE*) in fluorescent OLEDs is only 25%. Fortunately, the selection rule can be broken by the strong spin-orbit coupling in phosphorescent molecules due to the mixing of singlet and triple states, usually effected by insertion of a metal atom with high orbital angular momentum into the molecule. The Hamiltonian, H_{SO} for spin-orbit interaction is [110],

$$H_{SO} = -\frac{Ze^2}{8\pi\epsilon_0 m_e^2 c^2 r^3} \hat{l} \cdot \hat{s} \quad (2.21)$$

where Ze is the charge of the nucleus, m_e is the electron mass, c is the speed of light, r is the electron-nucleus distance, \hat{l} and \hat{s} are the electron orbital and spin angular momentum, respectively. To see how H_{SO} mixes singlets and triplets, apply

$$\begin{aligned} (H_{SO})_z &= A_1 \hat{l}_{1,z} \cdot \hat{s}_{1,z} + A_2 \hat{l}_{2,z} \cdot \hat{s}_{2,z} = \\ &(A_1 \hat{l}_{1,z} + A_2 \hat{l}_{2,z}) \cdot (\hat{s}_{1,z} + \hat{s}_{2,z}) + (A_1 \hat{l}_{1,z} - A_2 \hat{l}_{2,z}) \cdot (\hat{s}_{1,z} - \hat{s}_{2,z}) \end{aligned} \quad (2.22)$$

to $\langle 1,0 | H_{SO} | 0,0 \rangle_z$. Since, $\langle 1,0 | (A_1 \hat{l}_{1,z} + A_2 \hat{l}_{2,z}) \cdot (\hat{s}_{1,z} + \hat{s}_{2,z}) | 0,0 \rangle = 0$,

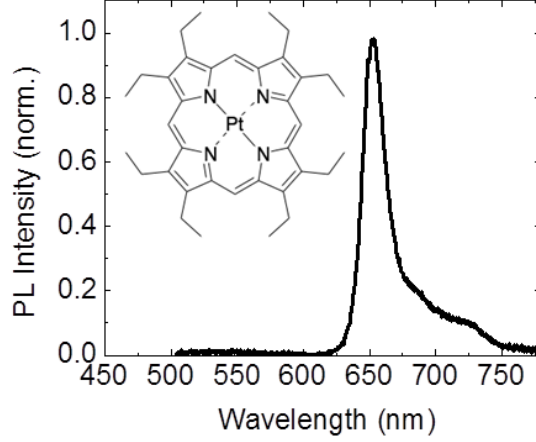


Figure 2.6 Chemical structure and emission spectrum (when doped at 2 vol% in Alq₃) of an archetype phosphorescent molecule, platinum-octaethyl-porphyrin (PtOEP).

$$\begin{aligned}
 \langle 1,0|H_{SO}|0,0\rangle_z &= \frac{1}{2} \langle 1,0|(A_1 \hat{l}_{1,z} - A_2 \hat{l}_{2,z}) \cdot (\hat{s}_{1,z} - \hat{s}_{2,z})|0,0\rangle \\
 &= \frac{\hbar}{2} \langle 1,0|A_1 \hat{l}_{1,z} - A_2 \hat{l}_{2,z}|1,0\rangle \\
 &= \frac{\hbar}{2} (A_1 l_{1,z} - A_2 l_{2,z})
 \end{aligned} \tag{2.23}$$

where $|1,0\rangle$ is a triplet with zero spin in the z direction, and $|0,0\rangle$ represents a singlet wavefunction. From Eq. (2.23), it is evident that H_{SO} breaks the transition rules between singlets and triplets, thus allowing singlet-to-triplet intersystem crossing as well as triplet emission.

Since r^3 is proportional to $1/Z^3$, Eq. (2.21) implies that H_{SO} is then proportional to Z^4 . Thus, the spin-orbit coupling effect is significantly stronger for a nucleus with a large atomic number. This concept guided the early discovery of efficient triplet emitters based on heavy metal (such as iridium and platinum) complexes, and thus the demonstration of

efficient phosphorescent OLEDs (PHOLEDs) [51, 52]. Figure 2.6 shows the chemical structure and emission spectrum of platinum-octaethyl-phorphyrin (PtOEP), based on which the first PHOLED was demonstrated.

2.2.2 Exciton Transport

Exciton transport refers to both the individual exciton energy transfer and the collective behavior of exciton diffusion. We first discuss the mechanisms for exciton transfer, and then show how exciton diffusion relates to the individual transfers.

Exciton transfer occurs from a donor (D) to an acceptor molecule (A, which may or may not be a different type from D). The rate of exciton transfer can also be calculated by Eq. (2.20) using $\psi_i = \psi_D^* \psi_A$ and $\psi_f = \psi_D \psi_A^*$, where the wave functions, ψ_D and ψ_A represent the donor and acceptor ground states, and ψ_D^* and ψ_A^* are the donor and acceptor excited states.

If the transfer Hamiltonian in Eq. (2.20) is a dipole-dipole interaction,

$$H_{dipole} = \frac{1}{4\pi\epsilon_0} \frac{1}{R_{AD}^3} \left[d_D \cdot d_A - \frac{3}{R_{AD}^2} (d_D \cdot \vec{R}_{AD})(d_A \cdot \vec{R}_{AD}) \right] \quad (2.24)$$

where \vec{R}_{AD} is the vector from the donor to the acceptor, \hat{d}_D and \hat{d}_A are the dipole moments of the donor and acceptor, respectively. Förster [111] first solved this Hamiltonian, deriving the Förster transfer rate, Γ_F given by:

$$\Gamma_F = \frac{1}{\tau_D} \left(\frac{R_F}{R_{AD}} \right)^6 \quad (2.25)$$

Here

$$R_F = \left[\frac{3\hbar^4 c^4}{4\pi n^4} \int \frac{1}{E^4} F_D(E) \sigma_A(E) dE \right]^{1/6} \quad (2.26)$$

is the Förster radius, τ_D is the donor exciton lifetime, $F_D(E)$ is the donor emission spectrum normalized to the photoluminescence quantum yield Φ_{PL} by $\int F_D(E) dE = \Phi_{PL}$, and $\sigma_A(E)$ is the acceptor absorption cross section.

Due to the dipole transition selection rule, Förster transfer between fluorescent molecules is only allowed for singlets; however, Förster transfer of triplets from phosphorescent molecules is allowed [58] for the same reason as triplet emission is allowed – i.e. due to strong spin-orbit coupling (see Eq. (2.23)). The emissive layer of fluorescent OLEDs typically utilizes the host-dopant architecture, where charge transport and recombination are through the host, and excitons on the host subsequently Förster transfer to the dopant for emission to occur. The Förster radius for such host-dopant system with strong emission and absorption overlap is typically 3 - 5 nm [10].

Hamiltonians containing other than dipole-dipole interactions in Eq. (2.20) can also give rise to exciton transfer. Most notably, Dexter [112] considered the electron-electron exchange interaction, whose matrix element is:

$$\begin{aligned}
\langle H_{exchange} \rangle &= \frac{1}{4\pi\epsilon_r\epsilon_0} \left\langle \psi_D(2)S_D(2)\psi_A^*(1)S_A^*(1) \left| \frac{1}{r_{12}} \right| \psi_D^*(1)S_D^*(1)\psi_A(2)S_A(2) \right\rangle \\
&= \frac{1}{4\pi\epsilon_r\epsilon_0} \left\langle \psi_D(2)\psi_A^*(1) \left| \frac{1}{r_{12}} \right| \psi_D^*(1)\psi_A(2) \right\rangle \langle S_D(2) | S_A(2) \rangle \langle S_A^*(1) | S_D^*(1) \rangle
\end{aligned}
\tag{2.27}$$

where S and ψ are the spin and spatial wave functions respectively. After calculating Eq. (2.20) using Eq. (2.27), the Dexter transfer rate is:

$$\Gamma_D = \frac{2\pi}{\hbar} \left| \langle H_{exchange} \rangle \right|^2 \int F_D(E) \sigma_A(E) dE .
\tag{2.28}$$

Note that Dexter exciton transfer only requires separate spin conservation in the two initial states and the two final states (a result of Eq. (2.27)); therefore, triplet transfer in fluorescent molecules is allowed by the relatively short-range Dexter transfer.

The collective motions of incoherent exciton transfer results in exciton diffusion, described by [113],

$$\frac{\partial N(\vec{r},t)}{\partial t} = G(\vec{r},t) - \frac{N(\vec{r},t)}{\tau} + D\nabla^2 N(\vec{r},t)
\tag{2.29}$$

where $N(\vec{r},t)$ is the exciton concentration, $G(\vec{r},t)$ is the exciton generation rate, τ is the exciton lifetime, and D is the exciton diffusivity. Assuming simple cubic lattice exciton diffusion sites and diffusion through only nearest neighbors, D can be calculated from the nearest neighbor exciton transfer rate Γ_m through:

$$D = a^2 \Gamma_m
\tag{2.30}$$

where a is the lattice constant. The exciton diffusion length $L_D = \sqrt{D\tau}$ is then defined by the average diffusion distance of an ensemble of excitons within their lifetime.

2.2.3 Exciton Interactions

Exciton interactions that result in annihilation are a special type of exciton transfer, where energy is transferred from an exciton to another excited state (exciton or polaron). The transfer Hamiltonian, and thus the rate for exciton interaction, can be calculated from Fermi's Golden rule (Eq. (2.20)). Common exciton interactions [47, 114, 115] in organics include singlet-polaron annihilation (SPA) [115], triplet-polaron annihilation (TPA) [116, 117], singlet-triplet annihilation (STA) [4, 118], triplet-triplet annihilation (TTA) [116, 119], etc.

When annihilation involves a singlet, its energy transfer is typically dominated by Förster type interactions (Eq. (2.25) and (2.26)), because the long-range dipole-dipole interaction has a significantly higher rate than the Dexter type interaction (Eq. (2.27) and (2.28)). In contrast, triplet annihilation usually follows Dexter type interactions.

The exciton annihilation rate depends on the relative distance between the energy donor and acceptor, which is constantly changing as a result of exciton diffusion. Therefore, as illustrated in Fig. 2.7, the description of collective exciton annihilation should also involve exciton diffusion. For example, one type of TTA occurs through,



where T is a triplet, T^n is a hot triplet (i.e. a spin symmetric exciton with a higher energy than T), and S_0 is the molecular ground state. Singlet formation during TTA is

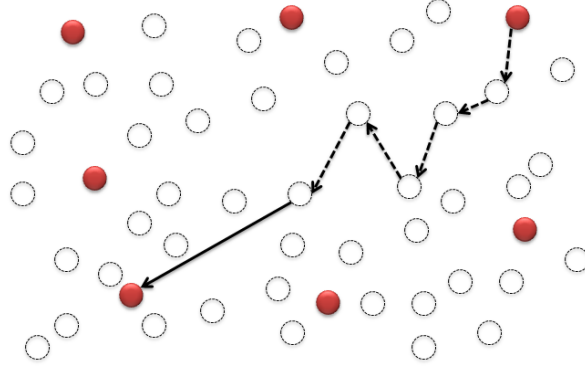


Figure 2.7 Annihilation between excitons (red filled circles) considering both exciton diffusion (dashed arrows) and exciton-to-exciton energy transfer (solid arrow). The open circles are the available transport site for excitons.

neglected by Eq. (2.31), and is treated by Eq. (2.41) in the next section. Thus, a description of triplet dynamics $T(\vec{r}, t)$ considering both triplet diffusion and annihilation is:

$$\frac{\partial T(\vec{r}, t)}{\partial t} = D_T \nabla^2 T(\vec{r}, t) - \frac{1}{\tau_T} T(\vec{r}, t) - \left[\int_{r_1} U_{TT}(|\vec{r}_1 - \vec{r}|) T(\vec{r}_1, t) dr_1^3 \right] T(\vec{r}, t) \quad (2.32)$$

where D_T is the triplet diffusivity, τ_T is the triplet lifetime, and $U_{TT}(r)$ is the interaction rate between two triplets. Although an analytical solution does not exist for Eq. (2.32), under the assumption that Eq. (2.31) occurs when two triplets are within a capture radius R_C following Smoluchowski [113], Eq. (2.31) can be simplified to,

$$\frac{\partial T(\vec{r}, t)}{\partial t} = D_T \nabla^2 T(\vec{r}, t) \quad (2.33)$$

with the boundary condition $T(r, t)|_{r=R_C} = 0$.

Now, Eq. (2.33) can be solved in spherical coordinates with $T(r, t = 0) = T_0$:

$$T(r, t) = T_0 \left[1 - \frac{R_C}{r} + \frac{2R_C}{r\sqrt{\pi}} \int_0^{\frac{(r-R_C)}{2\sqrt{D_T t}}} \exp(-x^2) dx \right]. \quad (2.34)$$

Then, the triplet flux at the boundary $r = R_C$ in the frame of motion of a center triplet as the annihilation center is:

$$4\pi R_C^2 D_T \left(\frac{\partial T}{\partial r} \right) \Big|_{r=R_C} = 4\pi D_T R_C \left(1 + \frac{R_C}{\sqrt{\pi D_T t}} \right) T_0 \approx 4\pi D_T R_C T_0. \quad (2.35)$$

After considering T_0 of such triplets all acting as annihilation centers:

$$\frac{dT_0}{dt} = -2 \times 4\pi R_C^2 D_T \left(\frac{\partial T}{\partial r} \right) \Big|_{r=R_C} T_0 = -8\pi D_T R_C T_0^2 \quad (2.36)$$

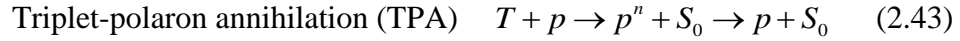
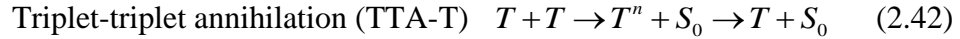
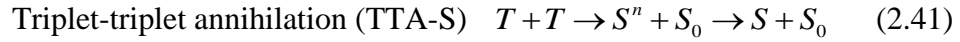
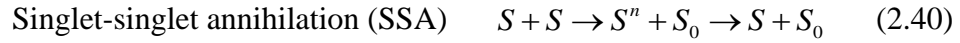
where the factor of 2 comes from the doubled diffusivity as a result of the relative motion of the participating triplets. Thus, when using a simple TTA rate, $k_{TT} = 8\pi D_T R_C$, triplet density dynamics considering both the triplet natural decay and TTA is then:

$$\frac{dT}{dt} = -\frac{T}{\tau} - \frac{1}{2} k_{TT} T^2. \quad (2.37)$$

Similarly, exciton density decay due to bimolecular annihilation is generally calculated by the product of the densities of the energy donors and acceptors, and an annihilation rate.

2.3 Exciton Interactions in Organic Light Emitting Diodes

Exciton interactions result in a non-linear dependence of exciton density on current density (J), thus contributing to change of OLED external quantum efficiency (EQE) vs. J . The functions of J - V (as discussed in section 2.1) and EQE - J are the two most important characteristics of an OLED. To model EQE - J in a fluorescent OLED, we consider the following exciton interactions,



where S , T , and p are the singlet, triplet, and polaron, and S^n , T^n , and p^n are the intermediate hot singlet, triplet, and polaron (i.e. S , T , and p are excited to higher energy states). The bimolecular interaction rates for Eq. (2.38) – (2.43) are k_{ST} , k_{Sp} , k_{SS} , k_{TT-S} , k_{TT-T} , and k_{Tp} , respectively. Assuming a uniform exciton formation rate in the OLED active region of thickness d , the singlet and triplet density dynamics are,

$$\frac{dS}{dt} = \frac{1}{4} \frac{J}{ed} - k_S S - k_{SS} S^2 - k_{ST} ST - k_{Sp} Sp + k_{TT-S} T^2 \quad (2.44)$$

$$\frac{dT}{dt} = \frac{3}{4} \frac{J}{ed} - k_T T - 2k_{TT-S} T^2 - k_{TT-T} T^2 - k_{Tp} T p \quad (2.45)$$

where the factors of $\frac{1}{4}$ and $\frac{3}{4}$ in the generation terms are determined by the formation ratio of singlet and triplet during charge recombination. If we only consider exciton natural decay and STA, and neglect all other interactions, under equilibrium condition,

$$S(t \rightarrow \infty) = \frac{Jk_T}{4edk_T k_S + 3k_{ST}J}. \quad (2.46)$$

Then, we can determine the $EQE(J)$ in the fluorescent OLED as,

$$EQE(J) = \eta_{out} \eta_{PL} \frac{k_S S(t \rightarrow \infty) d}{J/e} = \eta_{out} \eta_{PL} \frac{k_S k_T ed}{4edk_T k_S + 3k_{ST}J} \quad (2.47)$$

where η_{out} is the optical out-coupling efficiency, and η_{PL} is the radiative efficiency of the emitter. From (2.47), it is evident that $EQE(J)$ is a decreasing function of J , meaning that the OLED is less efficient if operated at high J (or high luminance).

Similarly, assuming efficient inter-system crossing and only TTA (Eq. (2.42)) in a phosphorescent OLED, the triplet density dynamics are determined by,

$$\frac{dT}{dt} = \frac{J}{ed} - k_T T - k_{TT-T} T^2. \quad (2.48)$$

Then, the $EQE(J)$ in the phosphorescent OLED is

$$EQE(J) = \eta_{out} \eta_{PL} \frac{edk_T}{2Jk_{TT-T}} \left[\sqrt{k_T^2 + \frac{4k_{TT-T}J}{ed}} \right] \quad (2.49)$$

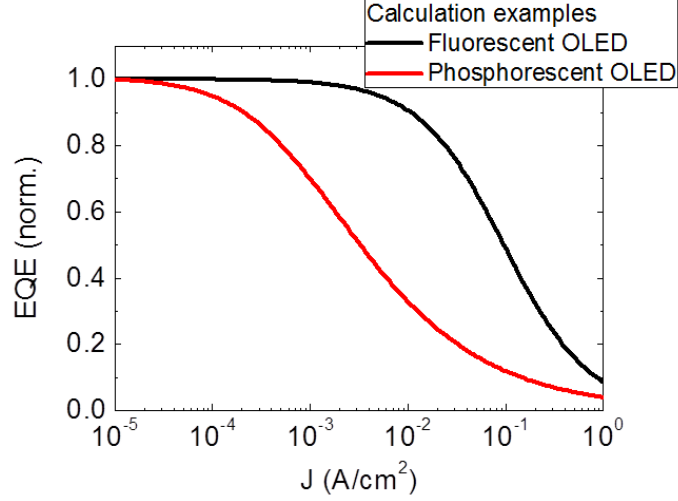


Figure 2.8 Calculated $EQE(J)$ for a fluorescent OLED with STA (Eq. (2.47)) and a phosphorescent OLED with TTA (Eq. (2.49)) using parameters described in text.

which can be simplified to $EQE(J) = \eta_{out} \eta_{PL} \frac{J_0}{4J} \left(\sqrt{1 + \frac{8J}{J_0}} - 1 \right)$ with $J_0 = \frac{2edk_T^2}{k_{TT}}$.

Therefore, $EQE(J)$ is also a decreasing function of J . Previously, Baldo et al. [116] pointed out that $EQE(J)$ drops to 50% of the peak EQE when $J=J_0$.

In Figure 2.8, we plot the calculated $EQE(J)$ based on Eq. (2.47) and Eq. (2.49) for the fluorescent OLED and the phosphorescent OLED respectively. In these calculations, we used the following parameters that are typical for organics: $k_S=3 \times 10^8 \text{ s}^{-1}$, $k_T=1 \times 10^5 \text{ s}^{-1}$, $k_{ST}=2 \times 10^{-10} \text{ cm}^3 \text{ s}^{-1}$, $k_{TT-T}=3 \times 10^{-12} \text{ cm}^3 \text{ s}^{-1}$, and $d=30 \text{ nm}$. It is thus clear that exciton interactions can strongly affect OLED efficiency, especially at high luminance. This dissertation is focused on understanding these interactions, and thus providing solutions through exciton management to enhance the desired interactions and suppress the detrimental interactions.

Chapter 3

Singlet-Triplet Annihilation in Fluorescent Organic Light Emitting Diodes

Electron-hole recombination (Eq. (2.13)) in OLEDs generates both singlets and triplets. As discussed in section 2.2.3, once a singlet collides with a triplet, the triplet can be temporarily excited to a hot triplet state, and then rapidly relaxed to its original triplet state. This is a process known as singlet-triplet annihilation (STA), in which the singlet energy is non-radiatively dissipated. Since singlets are responsible for fluorescent emission, STA leads to a loss of fluorescent OLED efficiency. In this Chapter, we introduce the dynamics of STA in fluorescent OLEDs, and then apply the dynamics to explain electroluminescence (EL) transient turn-on decays in two prototype fluorescent OLEDs. Finally, we discuss a strategy of de-exciting the detrimental triplets through the use of a phosphorescent dopant which results in decreased STA and thus can potentially improve fluorescent OLED efficiencies.

3.1 Dynamics of Singlet-triplet Annihilation (STA)

Figure 3.1 shows the basic structure of a bottom emitting OLED on glass substrate. The organic layers consist of an emissive layer (EML) sandwiched between an

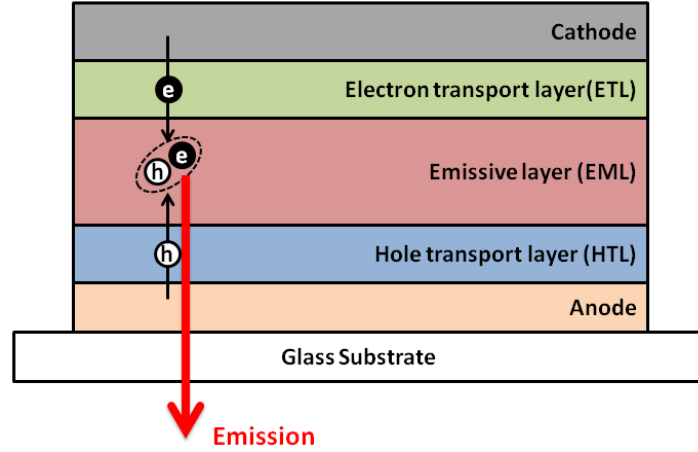


Figure 3.1 Structure of a bottom emitting OLED on glass substrate

electron transport layer (ETL) and a hole transport layer (HTL). Electrons and holes injected from the electrodes recombine in the EML, and the OLED emission is the out-coupled light from singlet radiative decay. In this section, we model the singlet and triplet dynamics after the charge recombination. It is shown that STA leads to singlet density transient decays following the fluorescent OLED turn-on.

Triplet density dynamics in fluorescent OLEDs are determined by the processes of triplet non-radiative decay, triplet-triplet annihilation (TTA), and triplet polaron annihilation (TPA). Of these, TTA occurs through two routes [115],



where T is triplet, S is singlet, and S^0 is the ground state. Considering spin statistics, when two triplets annihilate, the result is the fractional production of 3/4 triplet excited

states, 1/4 singlet excited state, and 1 molecular ground state [114]. Also, TPA is described by,

$$T + n \rightarrow S^0 + n, \quad (3.3)$$

where n is the polaron [120]. The polaron density arises both from injected charge determined by current density at time t , $J(t)$, and interfacial charge due to the junction capacitance [115]. Then, assuming Langevin recombination,

$$\frac{dn}{dt} = \frac{J(t)}{ed} - \gamma n^2, \quad (3.4)$$

where d is the width of the exciton formation region which is approximately equal to the width of the EML, and k_L is the Langevin recombination rate [89], given by:

$$k_L = \frac{e}{\varepsilon_r \varepsilon_0} (\mu_h + \mu_e) \quad (3.5)$$

Here, $\varepsilon_r = 2.9$ is the relative permittivity of the EML, ε_0 is the permittivity of free space, and μ_h and μ_e are the mobilities of holes and electrons in the EML, respectively. Equation (3.4) neglects the charge transit time from the electrodes to the EML. A complete treatment of the charge injection and transit can be found in [89]; our approximation allows for a simplified analytical treatment.

According to Eq. (3.1) to (3.5), the triplet density dynamics are given by:

$$\frac{dT}{dt} = \frac{3}{4} k_L n^2 - k_T T - \frac{5}{4} k_{TT} T^2 - k_{TP} n T, \quad (3.6)$$

where k_T is the triplet non-radiative decay rate, k_{TT} is the TTA rate, and k_{TP} is the TPA rate. The factors of 3/4 and 5/4 arise from the spin statistics of triplet generation and TTA, respectively.

The singlet density dynamics are a function of the singlet decay rate, as well as STA. Now, STA occurs via [4]:



where T^n is the intermediate hot triplet. This interaction is significant when the absorption spectrum of T overlaps the emission spectrum of S due to the Förster transfer mechanism as in Eq. (2.26) [4]. According to Eq. (3.1), (3.4), and (3.7), the singlet density dynamics are then described by:

$$\frac{dS}{dt} = \frac{1}{4}k_L n^2 - k_S S + \frac{1}{4}k_{TT} T^2 - k_{ST} ST, \quad (3.8)$$

where k_S is the singlet decay rate and k_{ST} is the STA rate. The factors of 1/4 arise from spin statistics similar to Eq. (3.6).

Using Eq. (3.4), (3.6), and (3.8), the simulated singlet, triplet, and polaron densities are plotted in Fig. 3.2 using reaction rates and other parameters typical of many doped fluorescent systems. The current density $J = 0.8 \text{ A/cm}^2$ is chosen for the calculation so that it is consistent with the J for transient EL measurements in the next section. It can be seen that after the polaron density reaches equilibrium according to Eq. (3.6), the triplet lifetime which is reduced by TPA (at rate $k_{TP}n$), governs the triplet dynamics. Before the triplet density becomes significant, the singlet density is determined

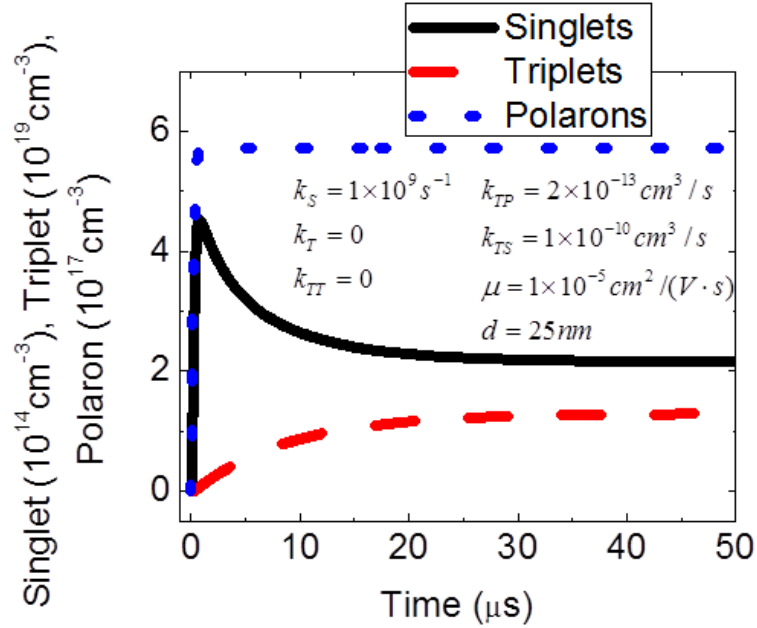


Figure 3.2 Simulated density dynamics according to the model in text for a device at 0.8 A/cm^2 injection current density using the parameters listed.

by the decay constant, k_s . As the triplet density increases over time, STA suppresses the continued increase of the singlet density. This results in a peak in singlet density. As the triplet density increases further, the STA term in Eq. (3.8) dominates, ultimately resulting in a decrease in the singlet density. Since the light output in fluorescent OLEDs is proportional to singlet density, STA leads to transient EL turn-on decays.

3.2 Transient Electroluminescence Turn-on Decay Due to STA

To observe the predicted EL transients, OLEDs were grown on commercially pre-coated indium-tin-oxide (ITO) on glass substrates cleaned as described previously [121]. Organic layers are deposited in a vacuum thermal evaporation chamber with base pressure $< 5 \times 10^{-7}$ Torr. A 40 nm thick 4,4'-bis[*N*-(1-naphthyl)-*N*-phenyl-amino]-

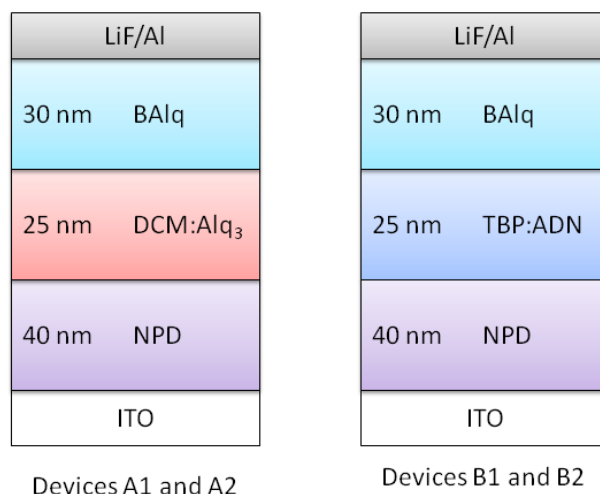


Figure 3.3 Structures for red emitting OLEDs A1 and A2 (left), and blue emitting OLEDs B1 and B2 (right). The short name of each layer is explained in text and also in Appendix A.

biphenyl (NPD) was first deposited as the hole transport layer (HTL), followed by a 25nm thick emission layer (EML), and a 30 nm thick bis(2-methyl-8-quinolinolate)-4-(phenylphenolato)aluminum (BAq) electron transport layer (ETL). The host, tris(8-hydroxyquinoline) aluminum (Alq₃), was doped with the red emitting fluorophore, 4-dicyanmethylene-2-methyl-6-(*p*-dimethylaminostyryl)-4*H*-pyran (DCM), and 9,10-Di(naphth-2-yl)anthracene (ADN) was doped with the blue emitting 2,5,8,11-tetra-tert-butylperylene (TBP) for the OLED EMLs. The chemical structures of these molecules are shown in Appendix A. The four OLEDs studied consist of the following dopant concentrations: 3 vol% DCM:Alq₃ (Device A1), 8 vol% DCM:Alq₃ (A2), 3 vol% TBP:ADN (B1), and 8 vol% TBP:ADN (B2). All devices were completed with a 0.8 nm thick LiF layer followed by an 80 nm thick aluminum cathode deposited through a shadow mask to form 1 mm² square devices. The structures of the four OLEDs are illustrated in Fig. 3.3.

After deposition, current-voltage-luminance (I - V - L) characteristics were measured in atmosphere using an HP4155 parameter analyzer with a calibrated Si photodiode following the standard procedures [122] (see Fig. 3.4 left). The OLED emission spectra were measured using a fiber-coupled OceanOptics USB4000 spectrometer (see Fig. 3.4 right). The device was then loaded into a N_2 chamber where the transient EL was measured by excitation with rectangular current pulses at a repetition rate of 5Hz and width of 100 μ s from a HP8114A pulse generator. Emission was collected by a Si avalanche photodiode (APD, Hamamatsu C5460), and monitored by an oscilloscope (Tektronix 3054B).

Figure 3.5 shows the EL turn-on for devices A1 and B2 as functions of time and current pulse amplitude. The ratio of peak-to-steady-state EL increases with drive current. Also, the rise time ($< 1 \mu$ s) is significantly shorter than the decay time ($\sim 20 \mu$ s). For DCM:Alq₃ devices (A1 and A2), the shape of the transient EL only weakly depends on the dopant concentration, while for the TBP:ADN device (B1 and B2), the EL turn-on

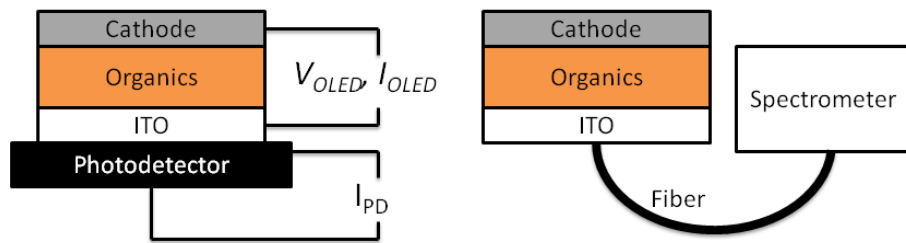


Figure 3.4 (left) Setup for OLED density-voltage-luminance (J - V - L) characterization. A parameter analyzer is used to measure the current (I_{OLED}) and voltage (V_{OLED}) through the OLED, and the current (I_{PD}) through a calibrated photodetector. (right) Setup for OLED emission spectrum measurement.

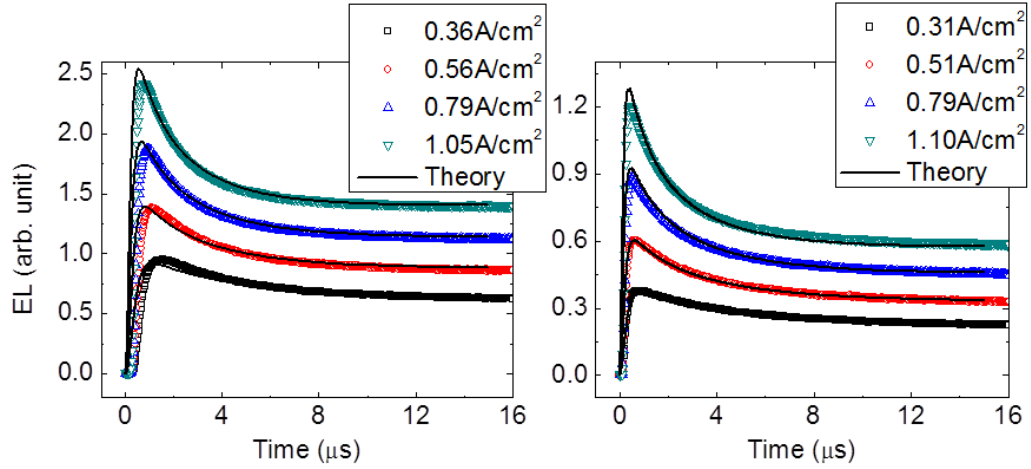


Figure 3.5 Transient electroluminescence (EL) of devices with 3% DCM:Alq₃ (left, device A1) and 8% TBP:ADN (right, device B2) in response to 100 μ s current pulses of different amplitudes. The steady state current density is indicated. Solid lines are the fits to the STA model, which determine the STA rate of 1.9×10^{-10} cm³/s and 1.2×10^{-10} cm³/s for A1 and B2, respectively. Similar fits are obtained for all four devices with results summarized in Table 3.1.

peak increases with doping concentration.

Fits to the data according to Eq. (3.4), (3.6), and (3.8) using the parameters in Table 3.1 are indicated by solid lines. We note that the exciton formation region for the four devices is located at the interface between the HTL and EML [123, 124]. Hence, only the electron mobility is required in Eq. (3.5), which is extracted from the transient EL turn-on delays in Fig. 3.5. Furthermore, triplet non-radiative decay and TTA in Eq. (3.6) are neglected since these processes are negligible compared to TPA during the device turn-on.

In the fits In Fig. 3.5, we assume that k_{TP} and k_{ST} are independent of pulse amplitude. The steady state current density range for the model fit is from 0.1 A/cm² to

1.0 A/cm², over which the EL peaks are prominent. The predicted EL slightly deviates from the experiment for the initial 1 μ s due to our neglect of the charge transit time in Eq. (3.4). From Table 3.1, the STA rates are unchanged for a given guest-host combination, regardless of doping concentration. This is expected since STA is a Förster type interaction (Eq. (2.26)) that only depends on the absorption spectrum of the triplet and the emission spectrum of the singlet [4]. Note that our value for the DCM:Alq₃ STA rate is in agreement with values obtained from optical excitation (1.9×10^{-10} cm³/s) of this mixture [4]. Furthermore, the \sim 50% decrease in the STA rate from 3% TBP:ADN to 8% TBP:ADN results since TBP acts as a triplet or polaron trap, which decreases the triplet-polaron collision probability as the TBP density decreases.

The turn-on peak recovery following the double pulse with varying delay times is shown in Fig. 3.6 (a) for device B2. We observe that a $>$ 600 μ s delay is necessary for the full recovery of the EL peak intensity. Fits of the data in Fig. 3.6 (a) to Eq. (3.4), (3.6), and (3.8) provide the triplet density as a function of delay time shown in Fig. 3.6 (b). A

Table 3.1 Fitting parameters for transient ELs from the OLEDs

EML	τ_S (ns)	k_{TP} (cm ³ /s)	k_{TS} (cm ³ /s)	μ (cm ² /V/s)
3% DCM:Alq ₃	1.2 \pm 0.1	(5.6 \pm 0.4) $\times 10^{-13}$	(1.9 \pm 0.2) $\times 10^{-10}$	(1.2 \pm 0.2) $\times 10^{-5}$
8% DCM:Alq ₃	1.1 \pm 0.1	(6.3 \pm 0.5) $\times 10^{-13}$	(1.8 \pm 0.2) $\times 10^{-10}$	(1.2 \pm 0.2) $\times 10^{-5}$
3% TBP:ADN	2.3 \pm 0.1	(13 \pm 2) $\times 10^{-13}$	(1.1 \pm 0.2) $\times 10^{-10}$	(1.6 \pm 0.3) $\times 10^{-5}$
8% TBP:ADN	2.1 \pm 0.1	(7.4 \pm 0.3) $\times 10^{-13}$	(1.2 \pm 0.1) $\times 10^{-10}$	(1.6 \pm 0.3) $\times 10^{-5}$

similar measurement was used to study device A1, and its peak recovery ($> 900 \mu\text{s}$) was slightly longer than for device B2.

The time required for recovery of the EL turn-on peak during the double pulse experiments is determined by temporal relaxation of the triplet density. When the double pulse delay is short compared to the triplet decay time, the triplet density remains large at the beginning of the second pulse, and STA suppresses the turn-on peak. It is worth noting here that the triplets are confined in the EML due to the large energy barriers of the adjacent HTL and ETL. That is, the NPD (2.29 eV) and BA1q (2.18 eV) triplet energies are higher than the triplet energies of the hosts, Alq₃ (2.03 eV) and ADN (~ 1.8 eV) [56, 125, 126]. Figure 3.6 (b) shows the triplet density as a function of time for 8%

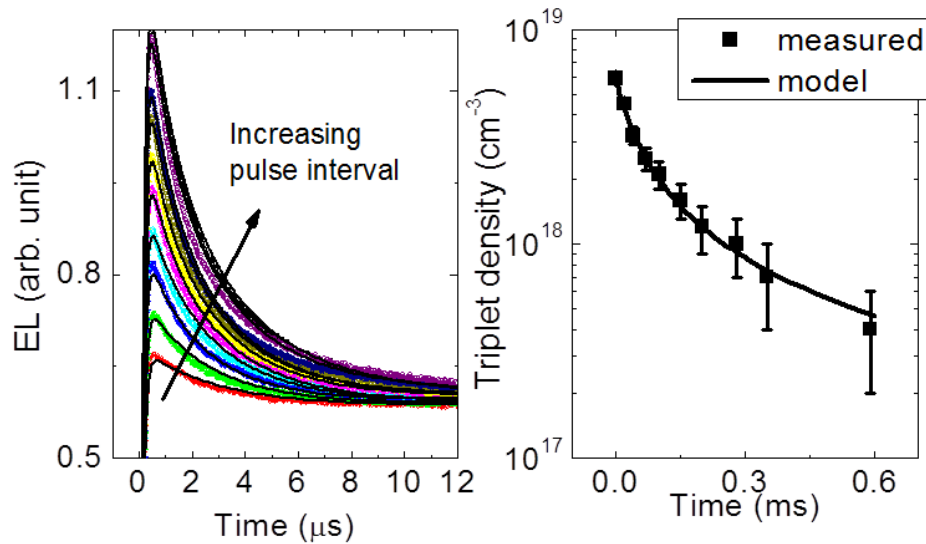


Figure 3.6 (a) Recovery of the turn-on peaks under double pulse current injection for device B2. All pulses are $100 \mu\text{s}$ in width. The data correspond to double pulse intervals (beginning from the lowest pulse) of 20, 40, 70, 100, 150, 200, 280, 350, $590 \mu\text{s}$. The fits are obtained using the model described in text. All parameters used in the fits are listed in Table 3.1. (b) Triplet density as a function of time following the device turn-off. This density decay is due to triplet-triplet annihilation (TTA).

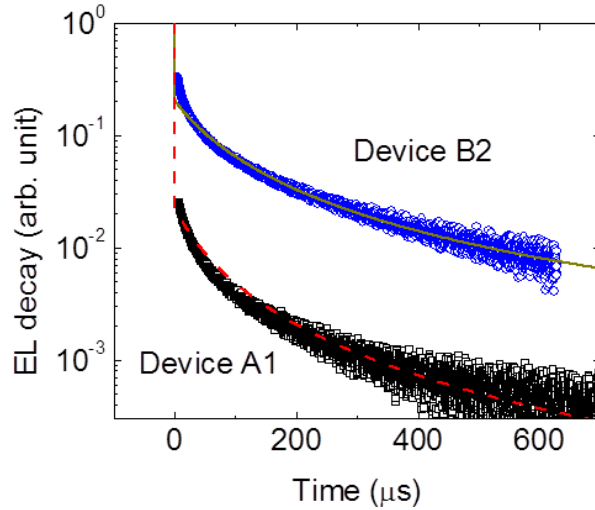


Figure 3.7 Delayed fluorescence from devices A1 and B2 after the turn-off of a current pulse with $100\mu\text{s}$ width. The steady state EL is normalized at the pulse onset. Lines are fits to TTA described in text. TTA rates of $(2.2\pm 0.2)\times 10^{-15}\text{ cm}^3/\text{s}$ and $(3.0\pm 0.3)\times 10^{-15}\text{ cm}^3/\text{s}$ are extracted for fits to the data for device A1 and B2, respectively.

TBP:ADN (device B2) after the end of the first current pulse. By fitting the triplet density following the device turn-off (solid line in Fig. 3.6 (b)), TTA rates of $2.4\times 10^{-15}\text{ cm}^3/\text{s}$ and $3.3\times 10^{-15}\text{ cm}^3/\text{s}$ are extracted for A1 and B2, respectively.

As expected from TTA, delayed fluorescence following the device turn-off was observed, and is shown in Fig. 3.7 for devices A1 and B2. By fitting the delayed fluorescence according to Eq. (3.4), (3.6), and (3.8) at $J=0$ and the corresponding initial polaron and exciton densities, TTA rates of $2.2\times 10^{-15}\text{ cm}^3/\text{s}$ and $3.0\times 10^{-15}\text{ cm}^3/\text{s}$ are extracted for A1 and B2. The TTA rates from the independent experiments of both peak recovery (Fig. 3.6) and delayed fluorescence are in agreement.

The TTA rates confirm the assumption that TTA is less efficient than TPA during device turn-on. Taking device B2 as an example and using the conditions in Fig. 3.5, the

TPA rate, $k_{TP}nT$ ($1.5 \times 10^{24}/\text{cm}^3/\text{s}$), is approximately ten times larger than the TTA rate, $\frac{5}{4}k_{TT}T^2$ ($1.3 \times 10^{23}/\text{cm}^3/\text{s}$). Similar conclusions can be drawn for all four devices.

The turn-on decay in an analogous device to A1 and A2 here [127] was previously attributed to recombination between injected holes and pre-trapped electrons on the dopant molecules. Since the hole mobility in the HTL is several orders of magnitude higher than the electron mobility in ETL [128]. For that case, the EL turn-on decay in the doped device is expected to be shorter than in un-doped devices, which was not observed [127]. Moreover, since the EL transients are unaffected by an applied reverse bias offset of up to 10V, we conclude that the density of trapped electrons must be insufficient to cause the observed fall-off in intensity. Alternatively, Ruhstaller et al. [90] explained the EL turn-on decay in an un-doped OLED based on the temporal imbalance of charges in the EML. However, the EL peak-to-steady-state intensity ratio inferred from their model (~ 1.2) is much smaller than observed here (2), and does not anticipate the double pulse peak recovery time.

3.3 Use of a Phosphorescent Dopant to Reduce STA

To further test the importance of triplet-mediated annihilation, we fabricated a device where the EML consists of the near infrared emitting phosphorescent dopant, 1% vol Pt-tetraphenyltetrabenzoporphyrin (Pt(TPBP)) [129] (see Appendix A for the chemical structure) co-doped with 8 vol% TBP in the ADN host. The lifetime and energy of Pt(TPBP) triplet is $50\mu\text{s}$ and $< 1.7\text{eV}$, respectively [129]. The transient EL response and spectrum of this device, along with that of device B2 at the same steady state light

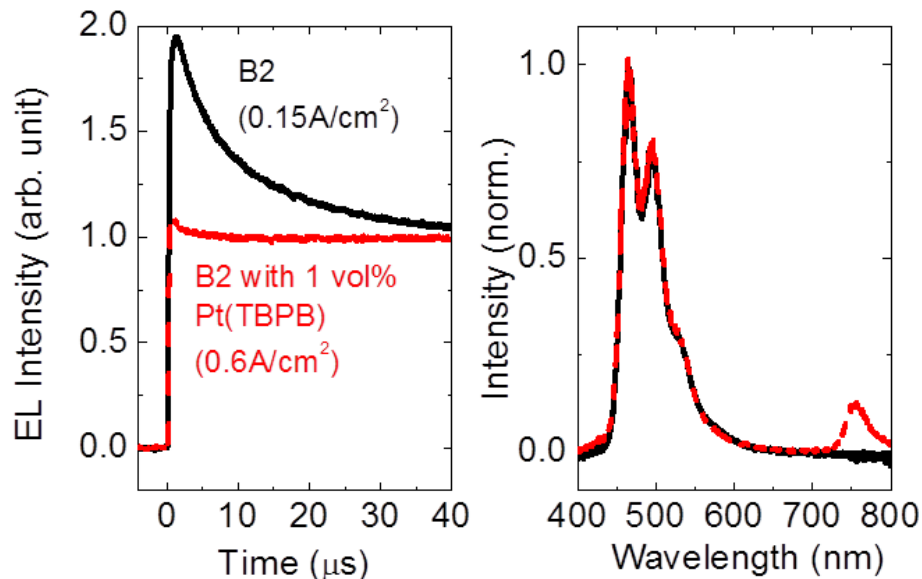


Figure 3.8 (a) Electroluminescence transient of 1% Pt(TBPB) and 8% TBP co-doped with the host and, and the control device (8% TBP:ADN, device B2) measured at the same steady state light output. (b) Spectra of these two devices.

intensity are given in Fig. 3.8 (a). Here, Pt(TBPB) traps triplets in the fluorescent OLED EML, thereby lowering the triplet density. From Fig. 3.8 (a) it is evident that the EL turn-on peak is substantially lower in the co-doped device than in the control at the same steady state EL output, consistent with our model. The spectral peak at a wavelength of $\lambda = 760$ nm in the co-doped device (Fig. 3.8 (b)) confirms the triplet energy transfer from to Pt(TBPB).

Ideally, the steady-state EQE of the co-doped device should be higher than in device B2 due to reduced STA; however, as seen in Fig. 3.8 (a), the doped device EQE is only 25% that of device B2. This is due to the narrow transport gap of Pt(TBPB) [129], and hence this molecule also acts as a polaron trap and non-radiative recombination center. Hence, the requirements for an ideal triplet-trapping phosphor are: 1. The triplet

energy of the phosphor is lower than the host or the dopant; 2. The transport gap of the phosphor is no less than that of the host; 3. The phosphor does not strongly absorb the fluorescent emission; and 4. the lifetime of the phosphor is short compared to the triplet decay time in the host. When co-doped in the fluorescent OLED EML, such a phosphor is expected to both suppress the STA and improve the device efficiency.

To conclude this chapter, electroluminescence transient turn-on peaks in doped fluorescent OLEDs are observed and quantitatively attributed to STA. The transient EL of DCM:Alq₃ and TBP:ADN OLEDs with different doping concentrations are fit to a model that includes STA, TTA and TPA. The STA rate is found to be independent of doping concentration, which confirms the Förster transfer nature of this interaction. By studying the recovery of the peak, the triplet density decay is found to follow the TTA after the current turn-off, which is further confirmed by the device delayed fluorescence. By co-doping a near infrared phosphor along with the fluorescent dopant in the EML, we observed a decrease the STA, and thus eliminated the turn-on intensity transient. This device architecture can potentially lead to increased EQE of fluorescent OLEDs at high luminance.

Chapter 4

Managing Triplets in Fluorescent OLEDs

We see from Chapter 3 that singlet-triplet annihilation (STA) in fluorescent OLEDs results in electroluminescence (EL) transient turn-on decay, thus contributing to a loss mechanism to efficiency. Although co-doping of a phosphor into the fluorescent OLED EML reduces the transient EL decay, the overall OLED efficiency is reduced as a result of charge and exciton trapping, as well as absorption due to the phosphor. In this chapter, it is shown that both suppressed STA and improved OLED efficiency can be achieved by a triplet management strategy, i.e. co-doping of a fluorescent molecule, called the triplet manager, in the fluorescent OLED EML. In section 4.1, we introduce the concept of triplet management in fluorescent OLEDs, followed by an experimental demonstration of this strategy in sections 4.2 and 4.3.

4.1 Concept of Triplet Management

Efficiency loss in fluorescent organic light emitting diodes (OLEDs) has been variously identified as resulting from singlet-polaron annihilation (SPA) [115, 130], charge imbalance [131], and singlet-triplet annihilation (STA) [118]. In the case of STA, according to Eq. (3.8), the efficiency reduction is proportional to the product of the triplet

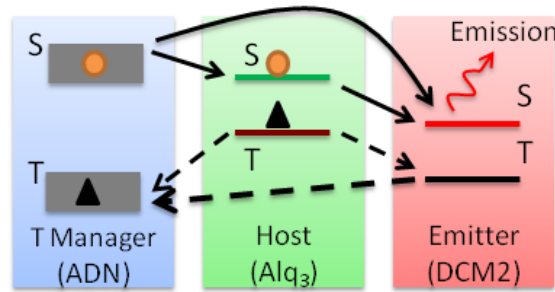


Figure 4.1 (a) Proposed singlet (S) and triplet (T) energy transfers in a fluorescent OLED using a T manager. Here, singlets (circles) and triplets (triangles) are generated on both the host and T manager. Singlets Förster-transfer (solid lines) to the guest, and triplets Dexter-transfer (dashed lines) to the manager. The shaded regions on the T manager indicate the required energy level ranges.

density and the annihilation rate. Since 75% of the injected charge results in the formation of non-radiative triplets [55] with relatively long lifetimes (typically > 1 ms) compared to radiative singlets (~ 1 -10 ns), triplets in fluorescent OLEDs can reach a high density ($> 10^{18}$ cm^{-3}). Also, fluorescent OLEDs often utilize a laser dye as the emitter [123], which usually has a overlap between the singlet emission and triplet absorption spectra, leading to a large STA rate [4]. The combined large triplet density and high STA rate can reduce the OLED efficiency [118].

The conventional emission layer (EML) of a fluorescent OLED consists of a conductive host and an emissive guest. Because the guest often has lower singlet and triplet energies than the host, both excitonic species formed on the host upon electrical excitation transfer to the guest where STA occurs. One strategy [118] to reduce quenching is to blend a third molecule called a “triplet manager” into the EML to collect triplets, as shown in Fig. 4.1. If the triplet manager has a higher singlet and lower triplet energy than the guest, it facilitates Förster transfer of singlet excitons to the guest, and

Dexter transfer of triplet excitons from the guest to the manager, thereby eliminating guest STA.

Therefore the requirements and the corresponding rationales for an ideal triplet manager are: 1. The triplet energy of the manager is lower than the host or the emissive guest so that triplets can exothermically transfer to the manager; 2. The transport gap of the manager is no less than that of the host so that the manager does not act as traps for charge transport; 3. To maintain the high guest fluorescent yield, the manager should have negligible absorption of the guest emission; and 4. To ensure vacant managers to collect detrimental triplets, the triplet lifetime of the manager should be short compared to the triplet decay time in the host or the dopant.

4.2 Suppressed EL Turn-on Decay through Triplet Management

To demonstrate the effectiveness of such a strategy, we fabricate OLEDs with EMLs comprising a tris(8-hydroxyquinoline)aluminum (Alq₃) host, doped with 2 vol% of the red emitting guest, 4-(dicyanomethylene)-2-methyl-6-julolidyl-9-enyl-4H-pyran (DCM2). Various concentrations ($0 \leq x \leq 70$ vol%) of 9,10-di(naphtha-2-yl)anthracene (ADN) are blended in the EML for triplet management.

The OLEDs were fabricated in vacuum ($\sim 10^{-7}$ Torr) by thermal evaporation on pre-patterned indium-tin-oxide (ITO)-coated glass substrates following standard procedures [131]. The 25 nm EML is sandwiched between a 35 nm 4,4'-bis[N-(1-naphthyl)-N-phenyl-amino]-biphenyl (NPD) hole transport layer (HTL), and a 25 nm bathocuproine (BCP) electron transport layer. The chemical structures for these

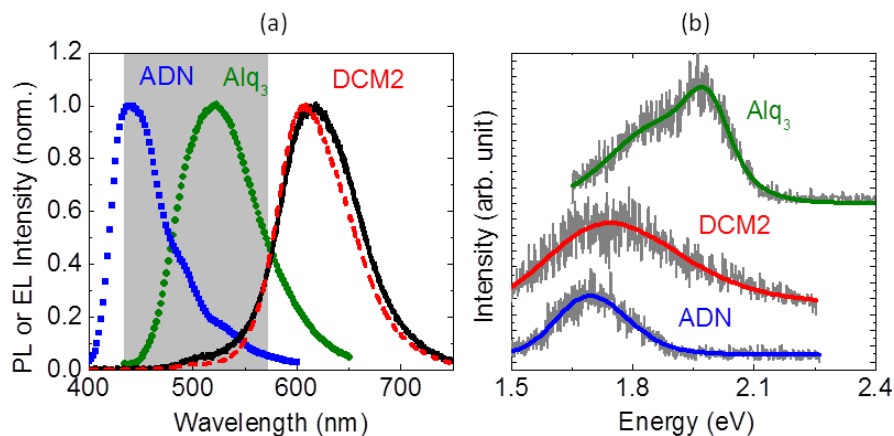


Figure 4.2 (a) Photoluminescence (PL) spectrum of ADN (squares) and Alq₃ (circles) film, and electroluminescence (EL) spectrum of organic light emitting diodes with emission layers consisting of 2% DCM2 doped Alq₃ (solid line) and ADN (50%)/Alq₃ (50%) (dashed line). The absorption range of DCM2 is in the shaded region. (b) Sensitized triplet emission from Alq₃, DCM2, and ADN measured at 14 K, the fits are to double-peak Gaussian for Alq₃ and single-peak Gaussians for the rest.

molecules are shown in Appendix A. The array of 1 mm² devices is completed by depositing 0.8 nm thick LiF and 100 nm thick Al through a shadow mask to define the cathodes. The steady state current density-voltage-luminance (*J-V-L*) characteristics were measured at < 0.3 A/cm² using a parameter analyzer and a calibrated Si photodetector. At higher currents of 0.1-2.5 A/cm², the electroluminescence (EL) intensity was measured using a pulse generator (100 μs pulse width) and an avalanche photodiode whose signal was monitored by an oscilloscope.

Figure 4.2 (a) shows the photoluminescence (PL) spectra of ADN and Alq₃ films, and the EL spectra for OLEDs with EMLs with *x*=0 and 50% ADN. The PL spectral overlap with the DCM2 absorption (shaded box), and the pure DCM2 OLED emission confirm the complete Förster transfer of singlets to the guest. Since the emissions of the

three molecules are from their singlets, their singlet energies are consistent with the illustration in Fig. 4.1.

Due to the negligible triplet emission from the three fluorescent molecules, two triplet sensitizers: *tris*(2-phenylpyridine)Ir(III) (Ir(ppy)₃), T = 2.4 eV [132] and *bis*(2-phenylquinoline) (acetylacetonate)Ir(III) (PQIr), T = 2.1 eV [133] are co-doped with these molecules to probe their triplet energies. These sensitizers enable efficient transfer of photo-generated triplets to the fluorescent molecules, thereby overcoming the low intersystem crossing rate in fluorescent molecules [126]. Photoluminescence at 14 K from the blend films: Alq₃ (25 vol%)/ Ir(ppy)₃ (75 vol%), DCM2 (50 vol%) / PQIr (50%), and ADN (50%)/ Ir(ppy)₃ (50%) using a N₂ pump laser (1 ns pulse) are measured using a streak camera. The delayed emission spectra from triplets at 0.4 ms to 9 ms after the pump pulses are shown in Fig. 4.2 (b). Triplet energies of Alq₃ (1.99 eV), DCM2 (1.74 eV), and ADN (1.69 eV) are extracted from fits to Gaussians (solid lines). The Alq₃ triplet energy is consistent with that obtained by Tanaka, et al [126]. Therefore, these energy assignments are consistent with the requirements in Fig. 4.1.

Figure 4.3 (a) shows the transient ELs for a series of OLEDs with different ADN fractions, x , following the onset of a $J = 2 \text{ A/cm}^2$ current step. For the control device ($x = 0$), the EL rapidly reaches a peak and then decays to a steady state intensity ~50% of its initial value during the following 20 μs . Since the EL intensity is proportional to the singlet density, the transient decay is an indication of STA as discussed in Chapter 3 [118]. Following the onset of the current pulse, the singlet density rapidly approaches its peak in the absence of triplets. As current is maintained, the long lifetime (~ms) triplet density increases, resulting in increased STA, and thus a decreased singlet density.

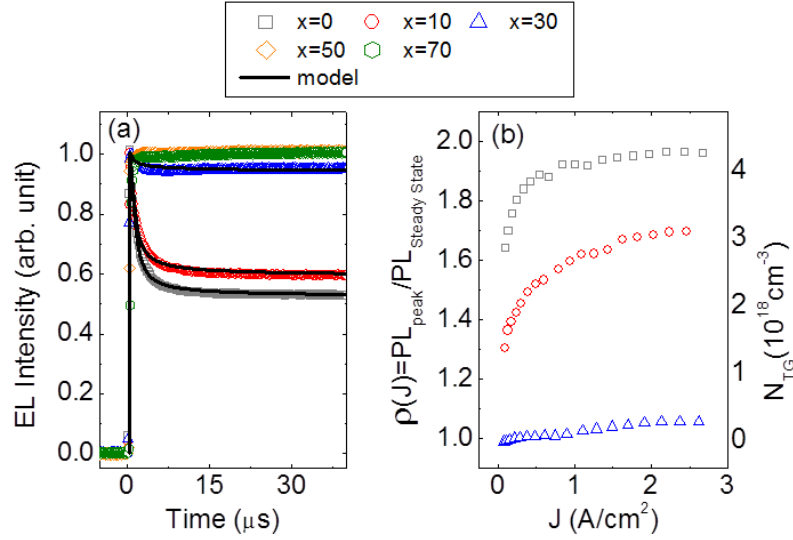


Figure 4.3 (a) Electroluminescence (EL) transients of OLEDs at various concentrations of ADN as a triplet manager pumped at $2\text{A}/\text{cm}^2$ using rectangular current pulses. Lines are fits to the model. (b) Intensity peak-to-steady-state ratio (ρ on left axis) as a function of current density for OLEDs with different triplet manager concentrations. The corresponding guest triplet densities (N_{GT} on right axis) are calculated as in text.

Finally, when the guest triplet density approaches steady state, STA also stabilizes, giving rise to a reduced singlet density.

In the presence of the triplet manager, the magnitude of the EL transient decay reduces with increasing x , and disappears for $x \geq 50\%$, indicating the complete suppression of STA. Figure 4.3 (b) shows the EL intensity peak-to-steady-state ratio, $\rho(J)$ for OLEDs in Fig. 4.3 (a). We find that $\rho(J)$ decreases with increased manager concentration, and $\rho(J) = 1$ for $x \geq 50\%$, corresponding to zero transient decay.

Two processes dominate energy transfer in OLEDs with triplet managers, namely guest STA, $S + T_G \rightarrow S_0 + T_G$ (S_0 is the ground state), and host-to-guest triplet Dexter transfer, $T_H \rightarrow T_G$ (where T_H includes both Alq_3 and ADN triplets). We model the EL using:

$$\frac{dS(t)}{dt} = b \frac{1}{4} \frac{J}{ed} - \frac{S(t)}{\tau_s} - k_{ST} S(t) T_G(t) \quad (4.1)$$

$$\frac{dT_H(t)}{dt} = b \frac{3}{4} \frac{J}{ed} - k_{HG} \exp\left(-\frac{2}{L} \sqrt[3]{\frac{1}{N_{GT}(J) - T_G(t)}}\right) T_H(t) \quad (4.2)$$

$$\frac{dT_G(t)}{dt} = k_{HG} \exp\left(-\frac{2}{L} \sqrt[3]{\frac{1}{N_{GT}(J) - T_G(t)}}\right) T_H(t) \quad (4.3)$$

where b is the charge imbalance factor [131], e is electron charge, d the EML thickness assuming that excitons are uniformly distributed across this layer, τ_s is the singlet natural decay lifetime, and k_{ST} is the STA rate. Also, k_{HG} and L are the host-to-guest triplet transfer rate coefficient and van der Waals radius, respectively, and $N_{GT}(J)$ is the saturation guest T population; i.e. when $T_G(t) \rightarrow N_{GT}(J)$, the transfer stops and $dT_G/dt = 0$. This treatment assumes 25% of injected charges form singlets [55]. The exponential factors are due to diffusive transfer of excitons between molecules consistent with the Dexter process [134]. Eventually, T_H saturates due to triplet-triplet annihilation (TTA) and natural decay, but these processes are much slower [118] (~ 1 ms) than the time window of interest (~ 30 μ s), and are thus neglected. Singlet-singlet annihilation is not considered since it is negligible at such low densities [135, 136]. Finally, SPA is also possible; however, it cannot result in the observed EL transients since the polaron density reaches steady state within tens of ns following the onset of the current pulse [118].

Assuming the boundary condition that $T_G = 0$ at $t = 0$, and $T_G = N_{GT}$ as $t \rightarrow \infty$ in Eq. (4.1), $\rho(J)$ is:

$$\rho(J) = 1 + \tau_s k_{ST} N_{GT}(J) \quad (4.4)$$

The external quantum efficiency roll-off is then given by $EQE(J) = \eta_0 \eta_c(J) \eta_T(J)$, where η_0 is EQE with perfect charge balance and no singlet quenching, $\eta_c(J)$ is the roll-off due to charge imbalance and SPA, and $\eta_T(J) = 1/\rho(J)$ is the roll-off due to STA.

From the PL transients measured for 50nm thick films using a N₂ laser pump, $\tau_s = 1.5 \pm 0.2$ ns for DCM2, independent of the manager concentration. For a 2 vol% DCM2 concentration, $L \approx 3$ nm as determined from the average distance between dopant molecules. With the constraint on $N_{GT}(J)$ given by Eq. (4.4), and for perfect charge balance ($b = 1$), the EL transients are fit by Eq. (4.1) - (4.3) as shown by the solid lines in Fig. 4.3 (a). From the fits, $k_{ST} = 1.5 \times 10^{-10}$ cm³/s, independent of host and manager concentrations, and is similar to previous values obtained [4, 118] for DCM:Alq₃. Also, we find $k_{HG} = 2.5 \times 10^7$ s⁻¹ for $x = 0$ and 10%, and $k_{HG} = 3 \times 10^8$ s⁻¹ for $x = 30\%$ ADN.

With these fits, we obtain N_{GT} using Eq. (4.4), with results also indicated in Fig. 2(b). Clearly, the introduction of the triplet manager substantially reduces N_{GT} . For example, at $J = 0.5-2.5$ A/cm², $N_{GT}(J)$ is reduced from 4×10^{18} cm⁻³ ($x = 0$) to $< 3 \times 10^{17}$ cm⁻³ ($x = 30\%$) and 0 cm⁻³ ($x \geq 50\%$).

4.3 Enhanced OLEDs Efficiency through Triplet Management

Since transient EL turn-on decay and thus STA are suppressed by using ADN as a triplet manager, it is expected that the fluorescent OLED efficiency should be improved

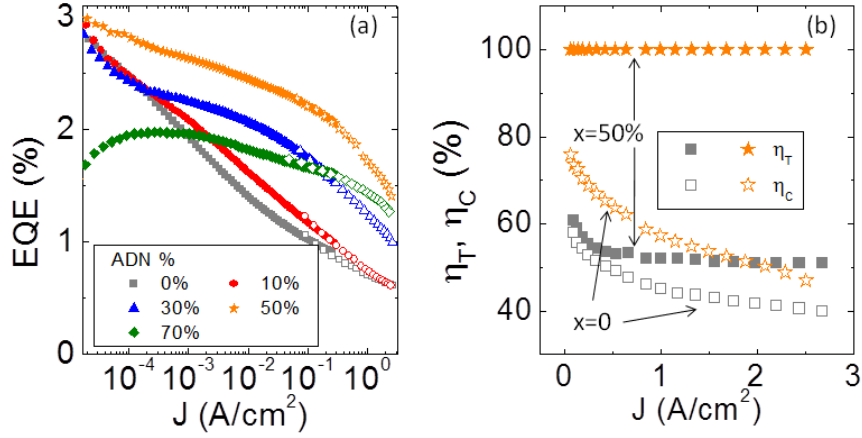


Figure 4.4 (a) External quantum efficiency (EQE) of triplet-managed OLEDs vs. of ADN concentration (x). The filled symbols are from steady-state measurements, and open symbols are from transient measurements. (b) Triplet (η_T) and polaron (η_C) induced EQE roll-off for $x=0$ and 50% OLEDs obtained from Eq. (4.4).

as a result. Figure 4.4 (a) shows $EQE(J)$ for different ADN concentrations. For $x = 0-50\%$, the $EQEs$ at low J ($< 10^{-4}$ A/cm²) are similar at $\sim 3\%$, while the EQE roll-off with J is reduced at higher x . At high currents ($J = 0.1-2.5$ A/cm²), the EQE at $x = 50\%$ is enhanced by more than 100% from $x = 0$ due to reduced roll-off. The separate contributions from polaron- and triplet-induced roll-off are plotted in Fig. 4.4 (b). Here, $\eta_T(J)$ is obtained from $\rho(J)$, while $\eta_C(J)$ is solved assuming $\eta_0 = 3\%$ obtained at $J \rightarrow 0$. From Fig. 4.4 (b), reduced STA is the major contribution for the enhanced EQE at $x = 50\%$, while polaron-induced roll-off is also slightly reduced at $x = 50\%$ due to bipolar charge transport in ADN. That is, while both ADN and Alq₃ are good electron transporting materials, ADN has a higher hole mobility [137]. This can result in more efficient recombination, and thus a smaller free carrier density in the EML. In turn, this reduces the SPA and thus slightly increases $\eta_C(J)$.

In contrast, EQE decreases when x increases from 50% to 70%, though in both cases, $\rho = 1$. This is attributed to reduced $\eta_c(J)$ at $x=70\%$ due to charge imbalance. Since the NPD lowest unoccupied molecular orbital (LUMO) energy is at 2.3 eV [124], the electron *blocking* barrier at the HTL/EML interface is smaller for ADN (with a LUMO at 2.6 eV) than that of Alq₃ (LUMO = 3.1eV). Thus at high ADN concentrations, electrons preferentially transport on ADN and more readily escape from the EML without recombination. Thus, the host (Alq₃) cannot be completely replaced by triplet manager to ensure that charge balance is maintained.

Liu et al. [138] have used ADN and rubrene as co-hosts in an OLED based on the fluorophore, 4-(dicyanomethylene)-2-t-butyl-6-(1,1,7,7-tetramethyljulolidyl-9-enyl)-4H-pyran (DCJTB), doped into Alq₃ to reduce the high intensity, steady state EQE roll-off. In that work, the enhanced EQE was explained by reduced SPA. Our analysis differs from that of Liu, et al. due to the measurement of the transient efficiency. This shows the

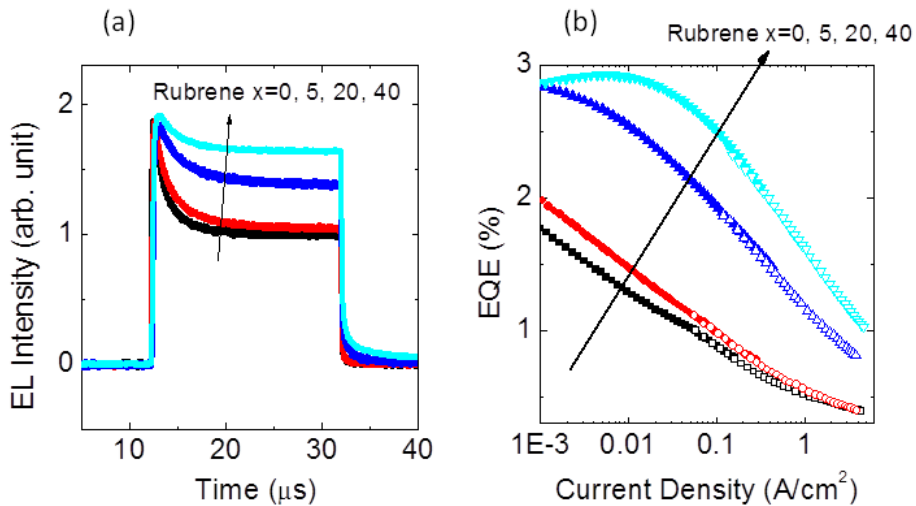


Figure 4.5 (a) EL transients for OLEDs with different rubrene concentrations ($x\%$) as a triplet manager measured at 2 A/cm^2 . (b) EQE of the triplet managed devices.

reduced STA is the principal cause of the enhanced *EQE*. Indeed, it is the transient EL data that provides the essential insights that lead to the triplet management concept presented here.

Rubrene has a triplet energy of 1.1 eV [139], which also satisfies the requirement as a triplet manager. Figure 4.5 shows the result of using rubrene at different doping concentrations in the EMLs of the same architecture as for ADN. From the transient EL (Figure 4.5 (a)), the EL turn-on decay is reduced with increasing the rubrene concentration. Also, *EQE* for triplet managed devices show significant improvement over the control device, consistent with our model.

In conclusion, we have demonstrated that triplet managers blended into the EML of conventional fluorescent OLEDs can lead to a significant increase in quantum efficiency at high current density. The manager molecules promote efficient triplet transfer from the guest, thereby reducing STA. Such a management strategy can be generally applied to fluorescent OLEDs that suffer STA to achieve very high luminance.

Chapter 5

Organic Semiconductor Lasers (OSLs) With a Continuous-wave Threshold

Following the demonstration of suppressed STA and thus improved EQE in fluorescent OLEDs through triplet management in Chapter 4, we show in this chapter that the same strategy leads to a significantly extended lasing duration in organic semiconductor lasers (OSLs). Indeed, triplets in OSLs not only annihilate with singlets (thus decreasing the cavity gain) but also absorb the lasing photons (thus introducing an additional cavity optical loss). Therefore, triplet-induced losses are more detrimental in OSLs than in fluorescent OLEDs. In section 5.1, we derive the existence of a continuous-wave (CW) lasing threshold unique to OSLs based on the saturation of triplet-induced losses. Then, experiments on OSLs with extended lasing durations through triplet management are presented. Finally, using the triplet management strategy, we show an experimental demonstration of a triplet managed OSL operating above the CW lasing threshold. The work presented in this chapter solves a long existing problem of triplet losses, thus removing a significant barrier toward the demonstration of an electrically pumped organic laser.

5.1 Theory for Continuous-wave (CW) Lasing in OSLs

Optically pumped organic semiconductor lasers (OSLs) with low thresholds and wide spectral tuning ranges have attracted interest since their demonstration 15 years ago [63-65, 140]. A variety of pulsed optical pump sources has been adopted; such as nitrogen laser [65, 140-142], pulsed Nd:YAG lasers [14, 63, 64, 143, 144], inorganic laser diodes and LEDs [6, 141]. However, a significant obstacle to the application of OSLs has been their limitation to only pulsed operation with a maximum duration of several tens of nanoseconds [4, 66, 67]. This limitation is imposed by the build-up of non-emissive triplet excitons in the gain region that are generated from intersystem crossing (ISC) of radiative singlet excitons [4, 70, 115]. Since the relaxation from triplet-to-ground state is quantum mechanically forbidden [134], the lifetime of triplets is large (~ms) compared to singlets (~ns) and the triplet density can accumulate over time. The high triplet density, together with overlapping singlet emission and triplet absorption, results in singlet triplet annihilation (STA) and photon absorption that ultimately shut down lasing.

To understand the lasing duration limitation in OSLs, we model the lasing dynamics through the following coupled density dynamics of singlets (S), host triplets (T_H), guest triplets (T_G), and lasing mode photons (P),

$$\frac{dS}{dt} = \frac{\eta I}{e_p d} - k_S S - k_{ISC} S - k_{ST} S T_G - \gamma \frac{c}{n_{eff}} P, \quad (5.1)$$

$$\frac{dT_H}{dt} = k_{ISC} S - k_{HG} \exp\left(-\frac{2}{L} \sqrt{\frac{1}{N_0 - T_G}}\right) T_H, \quad (5.2)$$

$$\frac{dT_G}{dt} = k_{HG} \exp\left(-\frac{2}{L} \sqrt{\frac{1}{N_0 - T_G}}\right) T_H, \quad (5.3)$$

$$\frac{dP}{dt} = (\Gamma\gamma - \alpha_{CAV} - \Gamma\sigma_{TT}T_G) \frac{c}{n_{eff}} P + \Gamma\beta k_S S, \quad (5.4)$$

where t is time, η is the fraction of the pump emission absorbed by the organic film, I is the pump intensity, e_p is the pump photon energy, d is the OSL gain medium thickness, k_S is the guest S natural decay rate, k_{ISC} is the host ISC rate, k_{ST} is the guest S-T annihilation rate, $\gamma = \sigma_{stim} S$ is the gain, σ_{stim} is the stimulated emission cross-section, c is the speed of light, and n_{eff} and Γ are the effective refractive index and optical confinement factor for the waveguide structure [145]. Also, k_{HG} is the host-guest Dexter transfer coefficient, L is the guest-host van der Waals radius, N_0 is the guest triplet saturation density, α_{CAV} is the cavity loss without contributions from triplet absorption, α_{TT} , and σ_{TT} is the guest triplet absorption cross-section, and $\beta \approx 10^{-4}$ is the spontaneous emission factor [146].

Then, the lasing condition for an OSL is calculated by its net gain,

$$g(t) = \Gamma\sigma_{stim}S(t) - \alpha_{CAV} - \Gamma\sigma_{TT}T_G(t) = 0 \quad (5.5)$$

thereby determining the threshold singlet density dynamics, $S(t) = S_{TH}(t)$. In Fig. 5.1 (a),

Table 5.1 Parameters for the lasing threshold calculation in Figure 5.1

d (nm)	200	L (nm)	1
k_S (s ⁻¹)	6.7×10^8	N_0 (cm ⁻³)	9.2×10^{17}
k_{ISC} (s ⁻¹)	1.3×10^7	α_{CAV} (cm ⁻¹)	10.4
k_{ST} (cm ³ s ⁻¹)	2×10^{-12}	Γ	0.69
n_{eff}	1.6	σ_{TT} (cm ²)	4.1×10^{-17}
k_{HG} (s ⁻¹)	5×10^{15}	σ_{stim} (cm ²)	2.3×10^{-16}

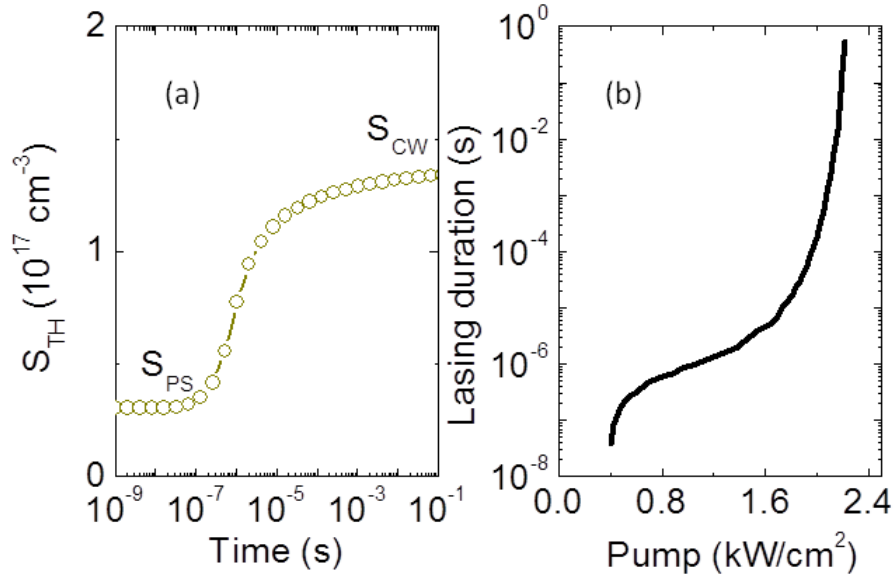


Figure 5.1 (a) Calculated singlet density threshold S_{TH} as a function of time after the turn-on of a step optical pump for parameters listed in Table 5.1. Note that two quasi-stable threshold densities exist: the pulsed threshold density S_{PS} and the continuous-wave threshold density S_{CW} . (b) Calculated lasing duration as a function of pump intensity.

we calculate $S_{TH}(t)$ using Eq. (5.1) – (5.5) and parameters given in Table 5.1. It is evident that $S_{TH}(t)$ is an increasing function of time, as expected from the dynamics of $T_G(t)$. Interestingly, two distinct threshold singlet densities emerge, with a CW threshold density (S_{CW}) occurring at a density larger than that needed for pulsed lasing (S_{PS}). As $t \rightarrow 0$, triplet loss $\Gamma \sigma_{TT} T_G \ll \alpha_{CAV}$, giving $S_{PS} = \alpha_{CAV} / (\Gamma \sigma_{stim})$. With time, T_G increases, concomitantly increasing the associated loss until $\Gamma \sigma_{TT} T_G > \alpha_{CAV}$. Finally, T_G reaches its saturation density, N_0 , at which point the triplet loss can no longer increase, giving $S_{CW} = (\alpha_{CAV} + \Gamma \sigma_{TT} N_0) / (\Gamma \sigma_{stim})$.

Neglecting the change in singlet density due to stimulated emission (see Eq. (5.1)), the CW threshold is approximately:

$$I_{CW}(N_0) = e_p d(k_s + k_{ISC} + k_{ST}N_0) \frac{\alpha_{CAV} + \Gamma \sigma_{TT} N_0}{\eta \Gamma \sigma_{stim}}, \quad (5.6)$$

compared to the pulse threshold $I_{PS} = I_{CW}(N_0 \approx 0)$. From Eq. (5.6), I_{CW} is a *quadratic* function of guest triplet saturation density: $k_{ST}N_0$ is from STA that reduces the gain; and $\Gamma \sigma_{TT} N_0$ is due to triplet absorption increasing loss. From the parameters in Table 5.1, $I_{CW} = 2.4 \text{ kW/cm}^2$. Figure 5.1 (b) calculates the lasing duration as a function of pump intensities for an OSL with parameters in Table 5.1, and the existence of the two thresholds is evident from the plot.

We note that the CW threshold described by Eq. (5.6) is general to all OSLs due to the temporal increase and saturation of triplet induced losses. However, no observation of CW lasing in OSLs was reported, due to the large $I_{CW} (> 30 \text{ kW/cm}^2)$ in conventional OSLs caused by a large triplet saturation density. As we show in the next section, this limitation can be overcome by use of triplet management in the gain medium of an OSL.

5.2 Fabrication and Measurement of OSLs

Organic lasers were fabricated by depositing organic thin films on grating substrates formed on SiO₂-on-Si substrates using interference lithography followed by a wet etch process. The workflow for grating substrate fabrication is as follows. The first step is to spincoat diluted photo resist (S1805 diluted with thinner at 1/6 ratio) at a spinning rate of ~ 5000 rpm onto a 2 μm-SiO₂-on-Si substrate. The thickness of the photo resist is 30 - 50 nm. The second step is expose the substrate to an interference setup using

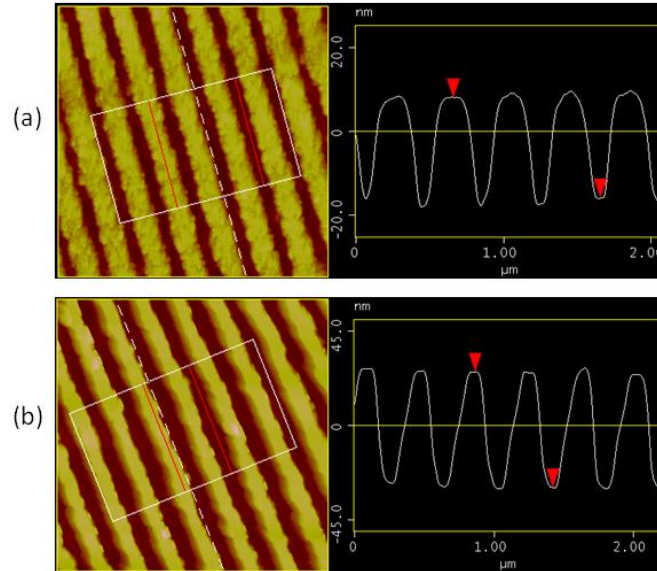


Figure 5.2 Atomic Force Microscope (AFM) images of the grating substrate before (a) and after (b) the wet-etch process.

an Argon ion laser and Lloyd mirror at the wavelength $\lambda = 457 \text{ nm}$ and the intensity of approximately 1 mW/cm^2 . The third step is to develop the photo resist in the developer MF-319 for 6 sec. The fourth step is to wet-etch the substrate in buffered oxide etchant (JTB5334-03) for 50 sec and rinse with de-ionized water. The final step is to rinse the substrate in acetone and then isopropanol to remove the photo resist. Atomic force microscope (AFM) images of representative gratings before and after the web-etch process is shown in Fig. 5.2.

Figure 5.3 shows the interference setup. The single wavelength output of the Argon ion laser is first filtered with a spatial filter to yield a clean optical wave-front. Subsequently, the direct beam interferes with the reflected beam (by a Lloyd mirror [69]) at the surface of the substrate under exposure, and the fringe period Λ is determined by

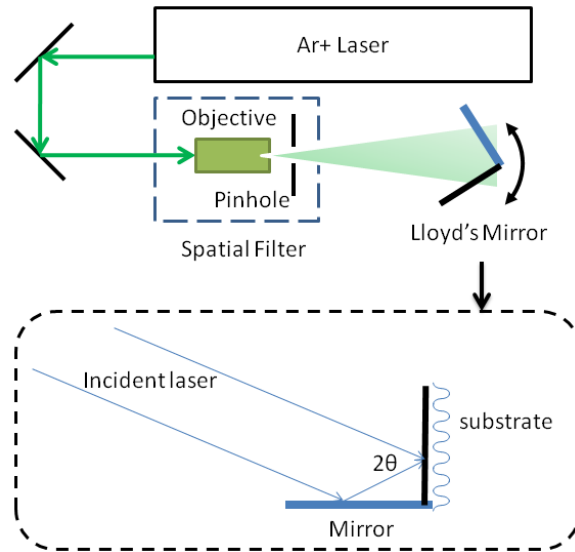


Figure 5.3 Interference exposure setup using an Argon ion laser and a Lloyd mirror for grating fabrication.

$\Lambda = \frac{\lambda}{2\sin\theta}$, where λ is the laser wavelength, and 2θ is the angle between the interference beams.

As illustrated in Fig. 5.4 (a), the OSL on 2nd order distributed feedback (DFB) grating is pumped through an ultraviolet laser at approximately 30° angle from the substrate normal direction. The emission from the OSL is measured by a photodetector or a spectrometer.

5.3 Extended Lasing Duration in OSLs with Triplet Management

The concept of triplet management in OSLs is identical to fluorescent OLEDs as discussed in section 4.1. For this demonstration, we use identical host, guest, and triplet manager molecules as in Chapter 4. The OSLs gain medium consists of the manager,

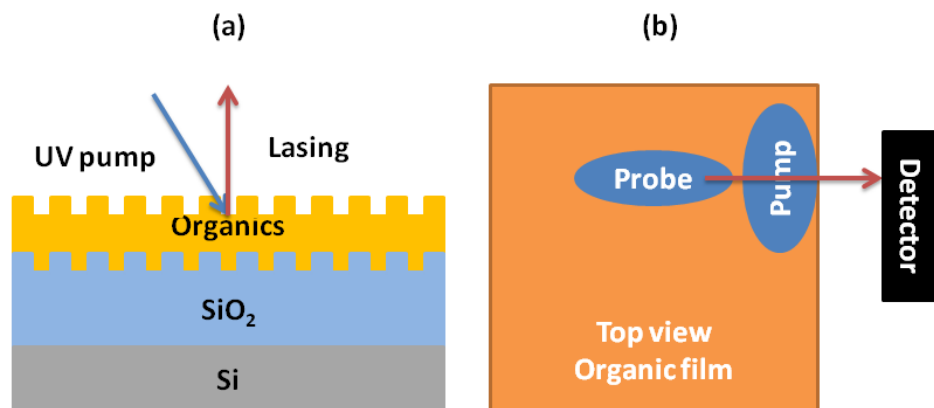


Figure 5.4 (a) Structure and operation of the organic semiconductor laser (OSLs) deposited on 2nd order SiO₂-on-Si distributed feedback grating. (b) Setup for measuring triplet absorption in an organic thin film.

9,10-di(naphtha-2-yl)anthracene (ADN), co-deposited into the conventional guest-host gain medium consisting of 2 vol% of the red emitting 4-(dicyanomethylene)-2-methyl-6-julolidyl-9-enyl-4H-pyran (DCM2) in tris(8-hydroxyquinoline) aluminum (Alq₃). The chemical structures for these molecules are shown in Appendix A.

The manager concentration in (100-x) vol% Alq₃ is x vol% ADN (x=0, 10, 30, 50, 70, 100). Blended films were deposited by thermal evaporation in high vacuum ($\sim 10^{-7}$ Torr) on quartz, Si, and 2 μm thick SiO₂-on-Si substrates for characterizing absorption, photoluminescence (PL), and triplet absorption, respectively. The same films were deposited on gratings with a period of (430 ± 5) nm and a 50 nm depth on the SiO₂-on-Si to form DFB OSLs. Output from a 0.6 W laser diode at wavelength $\lambda=405$ nm was focused to a 150 μm x 250 μm spot to optically pump the thin film. Alq₃ and ADN pure film absorption coefficients were measured to be $4.8 \times 10^4 \text{ cm}^{-1}$ and $9.1 \times 10^{-4} \text{ cm}^{-1}$ at $\lambda=405$ nm, and are assumed to contribute to the total blend film absorption proportionate to

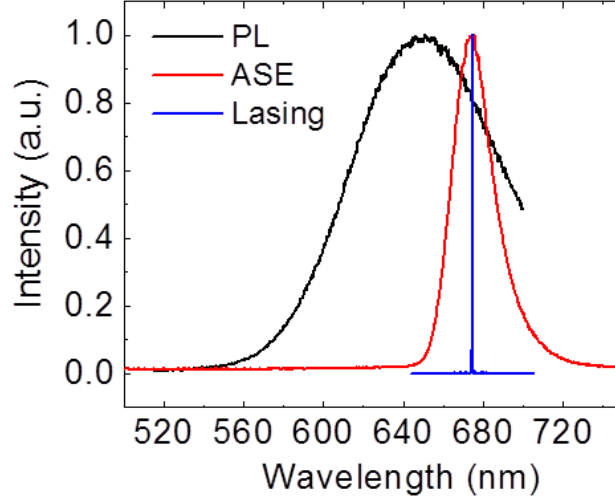


Figure 5.5 Photoluminescence (PL), amplified spontaneous emission (ASE), and lasing spectra of 2 vol% DCM2 doped Alq₃ thin film.

their volume. All measurements were performed in N₂ ambient to minimize film degradation.

Figure 5.5 shows the representative PL, amplified spontaneous emission (ASE), and lasing spectra from the gain medium with no triplet manager ($x = 0$), and mixing of triplet manager only has a minor effect on these spectra. The gain spectrum of OSLs closely resembles the ASE spectrum [147], and the period Λ of the grating substrate (430 nm) for OSLs is chosen to match the peak of the ASE spectrum through [66],

$$m\lambda = 2n_{eff}\Lambda \quad (5.7)$$

where $m = 2$ is chosen to achieve a second order surface emitting OSL.

To confirm the reduction of detrimental triplets on DCM2 through triplet management, we measure triplet absorption through spatially separated pump probe experiment proposed by Lehnhardt et al. [148] (see Fig. 5.4 (b)). The pump pulse from a

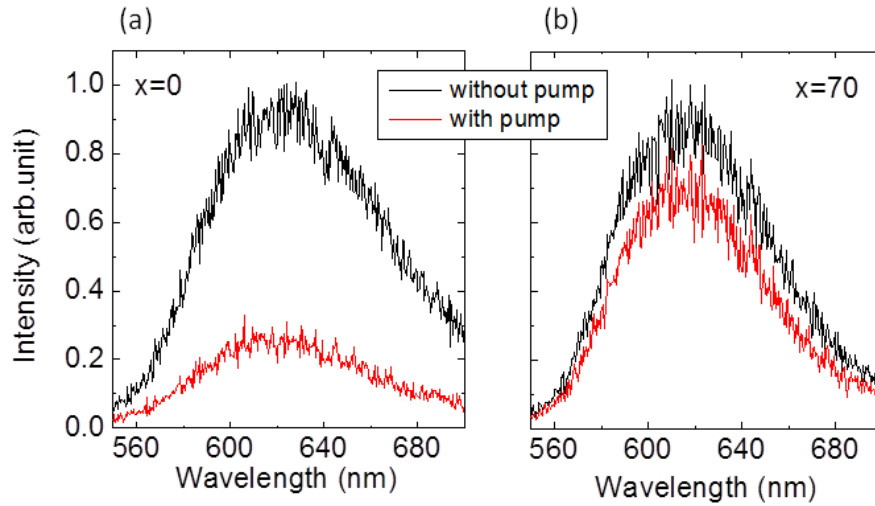


Figure 5.6 Probe pulse PL spectrum with and without the pump pulse for $x=0$ (a) and $x=70$ (b) films. The 200nm film was grown on SiO_2 ($2\mu\text{m}$)/Si substrate.

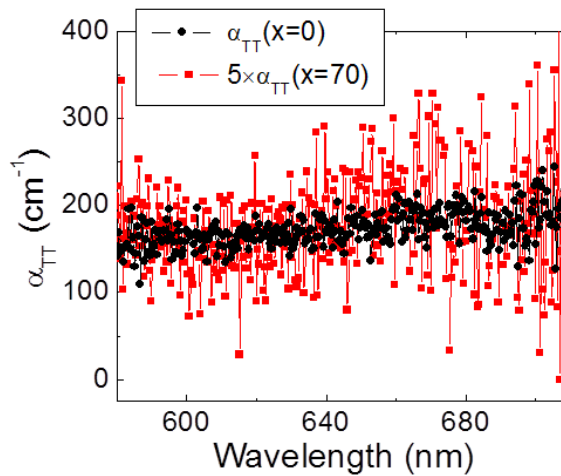


Figure 5.7 Absorption coefficient calculated for $x = 0$ and 70 from the data in Fig. 5.6.

$\lambda = 405$ nm laser diode has $50 \mu\text{s}$ duration, saturating the guest triplet; the probe pulse from a N_2 (1.5 ns width) laser is applied 100 ns after the turn-off of the pump. The film PL is collected from the film edge by either a streak camera (Hamamatsu C4334) for absorption spectrum $\alpha_{\text{TT}}(\lambda)$ measurement, or through a $\lambda = 680 \pm 5$ nm band-pass filter by

an avalanche photodiode (C5658) for α_{TT} near the lasing wavelength with a smaller error. Figure 5.6 shows the PL intensity from the probe with and without the pump pulse for $x=0$ and 70 films. We can see the triplet absorption is significantly reduced with introducing the triplet manager. From Fig. 5.6, two similar broad and featureless $\alpha_{TT}(\lambda)$ are obtained in Fig. 5.7, confirming that the absorptions are from the same excited state (guest triplet).

Figures 5.8 (a) and (b) show the PL and lasing transients pumped at 1.6 kW/cm^2 , respectively. From Fig. 5.8 (a), the Alq_3 host undergoes a 55% reduction in PL to its steady state value within $30 \mu\text{s}$ of the onset of the pump. Similar to the transient electroluminescence decay discussed in Chapter 3 and 4, this intensity roll-off is due to singlet quenching from STA. [4, 118] That is, following the onset, the singlet density rapidly reaches a peak and subsequently decays due to annihilation by the slowly

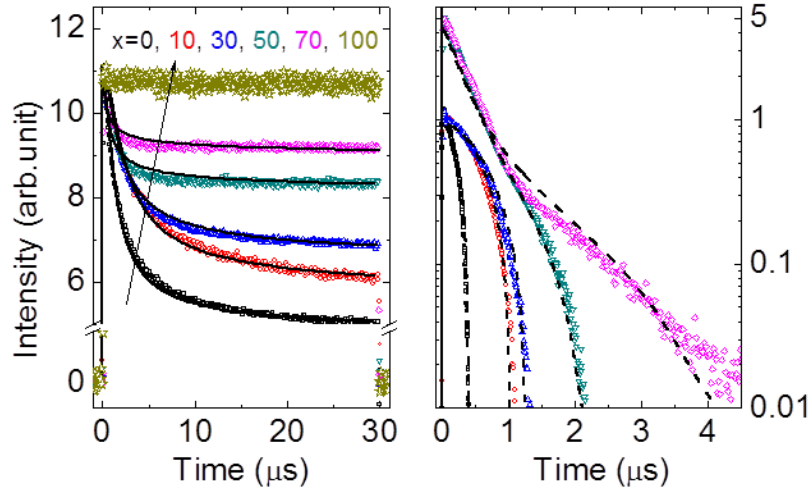


Figure 5.8 (a) PL and (b) lasing transients measured at 1.6 kW/cm^2 pump intensity for different host blends. The PL transients are normalized by the peak intensities, and lasing transients are normalized to 1 for $x = 0, 10,$ and 30 ADN blends, and to 5 for $x = 50$ and 70 . The fits are obtained by the model described in section 5.1 with parameters summarized in Table 5.2. Inset: Lasing spectrum of an $x = 70$ OSL.

increasing triplet density [118]. The existence of the long-term steady state PL intensity below its peak suggests saturation of the guest triplets. By including the ADN manger into the host blend with $x = 10$ to 70, the PL transient quenching is reduced to 17%. Further increasing to $x > 70$ can eliminate quenching entirely. We infer, therefore, that triplets are transferred from Alq₃ to DCM2, while the transfer from ADN to DCM2 is forbidden. Note, however, that morphology degradation under high pump intensity occurs for $x > 50$, consistent with the previous observation of morphological instability of ADN [149].

In Fig. 5.8 (b), more than a ten-fold increase in lasing durations (from approximately 400 ns to 4.5 μ s) is observed when x increases from 0 to 70. Lasing is not observed for $x = 100$ due to degradation. The threshold pulsed pump intensity, I_{PS} (characterized by an abrupt spectral narrowing from > 30 nm to < 0.5 nm, and a significant increase in the slope efficiency) was obtained using a 30 ns pump pulse (Table 5.2).

To understand quantitatively the PL and lasing dynamics, we fit the transients in Fig. 5.8 to Eq. (5.1) – (5.4), using the parameters provided in Table 5.2. Free parameters k_{ST} , k_{ISC} , k_{HG} , and N_0 are used in fitting the PL transients in Fig. 5.8 (a). For all films, $k_{ST} = 2.0 \times 10^{10}$ cm³/s, as expected for guest STA due to resonant energy transfer that is only dependent on DCM2 singlet emission and triplet absorption. As x increases, fewer triplets are transferred from Alq₃ to DCM2 and more are trapped on ADN; thus N_0 decreases from 5.0×10^{18} cm⁻³ to 9.2×10^{17} cm⁻³ when $x = 70$, leading to decreased PL transient roll-off. The $\sim 10^5$ increase in k_{HG} seems surprising, however, the Dexter transfer

rate is determined by $k_{Dex} = k_{HG} \exp\left[-\frac{2}{L} \sqrt[3]{\frac{1}{N_0 - T_G}}\right]$. Thus, for $T_G = 0.7N_0$, k_{Dex} only increases from $7.6 \times 10^4/\text{s}$ ($x=0$) to $4.4 \times 10^5/\text{s}$ ($x=70$), consistent with the shorter PL quenching time for higher x .

To model the lasing transients in Fig. 5.8 (b), three additional parameters: σ_{TT} , σ_{stim} , and α_{CAV} are required. Here, $\sigma_{TT} = \alpha_{TT}/N_0$ is shown in Table 1 at $\lambda = 680$ nm. Furthermore, $\alpha_{CAV} = \Gamma \sigma_{stim} S_{PS}$, where $S_{PS} = \eta I_{PS}/(e_p dk_s)$ is the pulse threshold singlet density, where triplet build-up under short excitation pulses is negligible. With these

Table 5.2 Parameters for analyzing the PL and lasing transients

Common fixed fit parameters					
d (nm)	200	L (nm)	1	n_{eff}	1.6
k_S (s^{-1})	6.7×10^8	Γ	0.69		
Parameters for PL transient fits in Fig. 5.5 (a)					
	x=0	x=10	x=30	x=50	x=70
k_{ST} ($\text{cm}^3 \text{s}^{-1}$)	2.0×10^{-12}	2.0×10^{-12}	2.0×10^{-12}	2.0×10^{-12}	2.0×10^{-12}
N_0 (10^{18} cm^{-3})	5.0 ± 0.4	3.9 ± 0.3	2.8 ± 0.3	1.5 ± 0.2	0.92 ± 0.08
k_{HG} (10^{10} s^{-1})	4.0	3.5	13	3.0×10^3	3.0×10^5
k_{ISC} (10^7 s^{-1})	3.3	2.6	2.3	1.7	1.3
Parameters for the lasing transient fit in Fig. 5.5 (b)					
	x=0	x=10	x=30	x=50	x=70
σ_{TT} (cm^2)	4.0 ± 0.3	3.8 ± 0.3	3.6 ± 0.4	4.3 ± 0.6	4.1 ± 0.4
σ_{stim} (cm^2)	1.9	2.0	2.4	2.1	2.3
Measured pulsed lasing and calculated CW lasing thresholds					
	x=0	x=10	x=30	x=50	x=70
I_{PS} (kW/cm^2)	0.93	0.75	0.72	0.45	0.43
I_{CW} (kW/cm^2)	32	19	8.8	3.7	2.2

measurements and assumptions, the lasing transients are fit using only a single free parameter σ_{stim} . We note that the effect of ADN as a triplet manager lies in its ability to decrease N_0 , while k_{ST} and σ_{TT} remain unchanged since they are intrinsic to DCM2.

5.4 Observation of the CW Threshold in an OSL

From the parameters in Table 5.2, and Eq. (5.6), the CW threshold can be calculated for the OSLs: $I_{CW} = 32, 19, 8.8, 3.7,$ and 2.2 kW/cm^2 for $x = 0, 10, 30, 50,$ and 70 respectively. Thus, due to organic film damage at high optical pump intensity, the high I_{CW} for the conventional OSL (i.e. $x = 0$) explains the lack of previous report on CW lasing in OSLs. In contrast, for OSLs with triplet management, I_{CW} can be significantly reduced, thus allowing for a direct observation.

To test the existence of this CW regime, we excited an $x = 70$ OSL at 2.4 kW/cm^2 , or just above the calculated value of $I_{CW} = 2.2 \text{ kW/cm}^2$. Figure 5.9 shows a streak camera image of this emission over $20 \mu\text{s}$ duration. Lasing intensity becomes weaker with time (leading to the apparent spectral narrowing) but does not turn off at the end of the long pulse, consistent with CW lasing theory. Indeed, we observed nearly $100 \mu\text{s}$ lasing duration when pumped by a single pulse, although film degradation due to high optical pump intensities ultimately limits the lasing duration. Hence, while this OSL has clearly exceeded its CW threshold, the laser operates quasi-CW due to material degradation.

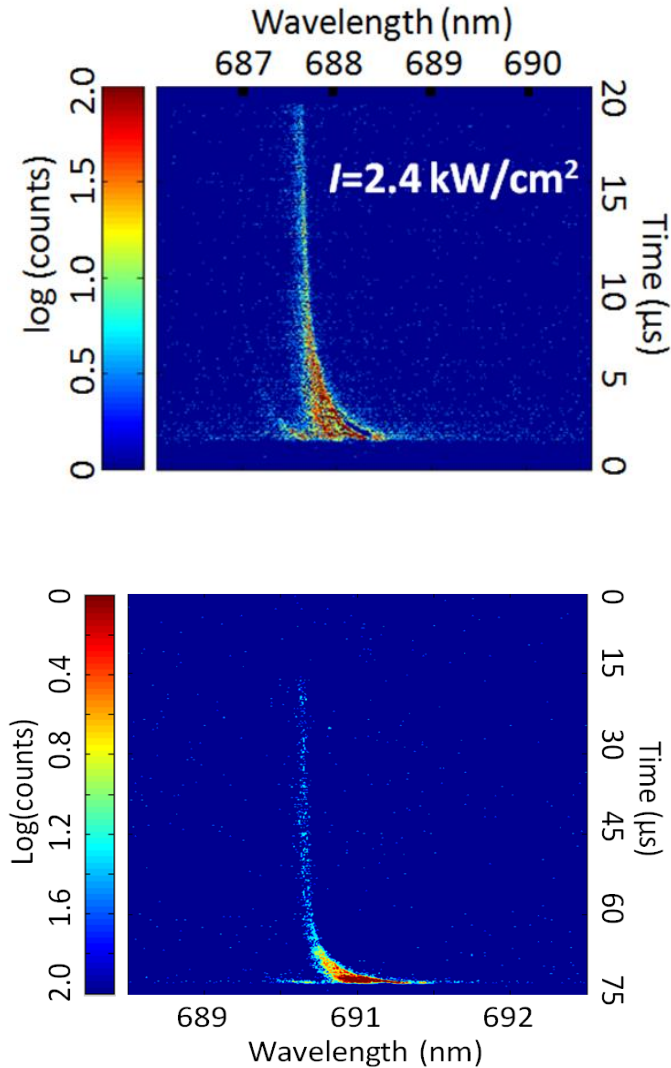


Figure 5.9 Lasing transients at a pump intensity $I = 2.4 \text{ kW/cm}^2$ (above the CW threshold) measured by a streak camera. The two figures are measurements from two OSLs with $x=70$ and slightly different organic film thickness ($\sim 200 \text{ nm}$), thus explaining the slightly different lasing wavelength.

Interestingly, the lasing wavelength shows blue-shift from $\lambda = 688.1 \text{ nm}$ to 687.7 nm during the lasing period. Wavelength shifts have been observed in liquid dye lasers [150] where they have been attributed to the competition of triplet absorption with the gain spectrum. In thin film single mode DFB OSLs where the triplet absorption is largely

constant, the shift is more likely due to changes in the effective refractive index with increasing T density.

We note that I_{CW} can be further reduced and the lasing time extended by using a more stable, lower triplet energy manager, and with a better match between the manager emission and the guest absorption than is achieved with ADN. Then, the smaller saturation guest triplet density contributes negligible loss, in which case $I_{CW} \rightarrow I_{PS}$. The design concept can be applied to the eventual development of electrically pumped organic semiconductor lasers, where 75% of the injected electrons result in triplets [55] compared to only a few percent in optical pumping.

In conclusion, we show the existence of a CW threshold at a higher pump intensity than the pulsed threshold observed in all previous OSL studies. Based on our analysis, we demonstrate a lasing duration of up to 100 μs by introducing a triplet manager into the OSL gain medium. The reduced triplet-induced loss of the triplet managed OSL decreases I_{CW} from 32 kW/cm^2 to a more practical value of 2.2 kW/cm^2 observed here.

Chapter 6

Triplet Contributions to Fluorescent OLED Efficiency

In Chapters 3 and 4, it is shown that non-radiative triplets in fluorescent OLEDs can lead to decreased efficiency due to singlet-triplet annihilation (STA). In contrast, triplet-triplet annihilation (TTA) results in the generation of radiative singlets, thus improving the fluorescent OLED efficiency. In this chapter, we study the trade-off between the two processes in a fluorescent OLED comprising a tetraphenyldibenzoperiflanthene (DBP) doped rubrene emissive layer with efficient TTA. In Section 6.1, we show experimental observation of both STA and TTA in the fluorescent OLED through transient electroluminescence, which are analyzed by the exciton dynamics model. The high OLED peak external quantum efficiency of 6.7% and rapid efficiency roll-off with current density are quantitatively explained by TTA and STA, respectively. In section 6.2, we introduce the concept of effective triplet current density as a figure of merit to evaluate the role of triplets in fluorescent OLEDs. The model suggests optimal materials properties needed for achieving high efficiency at high brightness in fluorescent OLEDs.

6.1 Fluorescent OLEDs with both STA and TTA

Recently, two types of exciton interactions, triplet-triplet annihilation (TTA), and singlet-triplet annihilation (STA) were separately found to significantly influence the efficiency of fluorescent OLEDs. TTA [119, 151] can generate singlets, thus increasing the theoretical limit of the *IQE* from 25%, to a maximum of 62.5% [57, 152-154]. On the other hand, STA [4, 155] reduces the singlet density, thereby lowering the efficiency by as much as 50% at high brightness [118, 156]. However, the relative importance of these two effects has not, to our knowledge, been studied, and the role of triplets remains largely unexplained.

Here, we study both TTA and STA in a fluorescent OLED based on its electroluminescence (EL) transients. We find that triplets can increase OLED efficiency via TTA at low current density (J), while it decreases the efficiency by STA at high J .

Triplet-triplet annihilation follows one of two pathways [107, 157, 158]:



where T is the triplet, S is the singlet, S_0 is the molecular ground state. By conservation of total spin angular momentum, formation of quintets is also an allowed process in TTA; however, since the quintet energy is usually significantly higher than twice the triplet energy, it is typically forbidden at room temperature [56, 157, 158]. The rates governing the relative importance of processes (6.1) and (6.2) are αk_{TT} and $(1-\alpha)k_{TT}$, respectively, where α is the fraction of annihilation events that follow processes (6.1) vs. (6.2), k_{TT} is the TTA rate constant. Process (6.1) contributes to

fluorescent OLED efficiency by creating additional singlets from non-radiative triplets. Several recent reports [56, 57, 152] have shown $\alpha > 0$, resulting in fluorescent OLEDs whose *IQE* exceed the 25% spin-statistical limit [55].

Additionally, STA is governed by [107]:



with the rate constant of k_{ST} . Process (6.1) occurs at rate $\alpha k_{TT} T^2$; process (6.2) at rate $(1-\alpha)k_{TT} T^2$; and process (6.3) at rate $k_{ST} ST$. Thus, the singlet and triplet density dynamics are described by:

$$\frac{dS}{dt} = \gamma(J) \frac{J}{4ed} - k_S S - k_{ST} ST + \alpha k_{TT} T^2 \quad (6.4)$$

$$\frac{dT}{dt} = \gamma(J) \frac{3J}{4ed} - k_T T - (1+\alpha)k_{TT} T^2, \quad (6.5)$$

where $\gamma(J)$ is the charge balance factor [89, 131], e is the electron charge, d is the charge recombination layer (i.e. emissive layer) thickness, and k_S and k_T are the singlet and triplet natural decay rates. In steady state, the external quantum efficiency, *EQE* can then be calculated from $S(t = \infty, J)$ to give:

$$EQE(J) = \eta_{OUT} \eta_S \frac{k_S S(t = \infty, J)}{J/(ed)}, \quad (6.6)$$

where η_{OUT} is the out-coupling efficiency [53] and η_S is the radiative efficiency of the singlet.

In rubrene (Fig. 6.1), the singlet energy ($E_S \sim 2.2$ eV) is twice the triplet energy ($E_T \sim 1.1$ eV), thereby enabling a high, resonant TTA (through process (6.1)) efficiency [56, 159]. Hence, in this work, tetraphenyldibenzoperiflanthene (DBP) [160, 161] is doped at 1 vol% in rubrene as the OLED emissive layer. During operation, excitons are

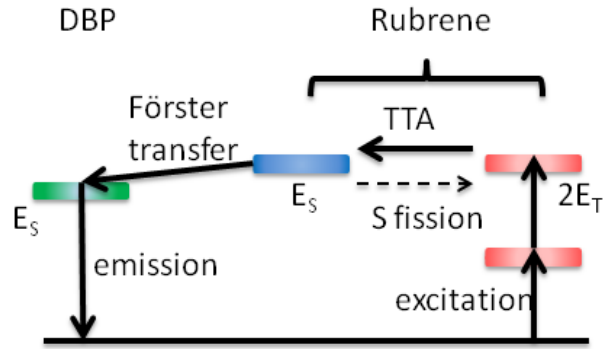


Figure 6.1 Energetics of a DBP doped rubrene mixture. In rubrene, the singlet energy, E_S , is twice that of the triplet ($2E_T$). In this case, singlet formation through triplet-triplet annihilation (TTA) is a resonant process. The use of a DBP dopant allows the Förster transfer of singlets from rubrene to DBP, which dominates over rubrene singlet fission.

formed on rubrene. Then, singlets can resonantly (by Förster process as in Eq. (2.25)) transfer to DBP and emit. Triplets are trapped on rubrene because its triplet energy is ~ 0.2 eV lower than DBP [56]. The 1 mm^2 square OLEDs were grown on indium-tin-oxide (ITO, as the anode) coated glass substrate by thermal evaporation of organic molecules [34] at a base pressure $< 5 \times 10^{-7}$ Torr. The OLED consists of a 40 nm thick 4,4'-bis[N-(1-naphthyl)-N-phenyl-amino]-biphenyl hole transport layer, a 35 nm thick emissive layer, a 40 nm thick rubrene electron transport layer, a 5 nm thick bathophenanthroline electron injection layer, and a 0.8 nm thick LiF layer followed by a 80 nm thick Al cathode. The chemical structures for the molecules are shown in Appendix A.

The EL transients following current density steps of magnitudes ranging from 4 mA/cm^2 to 57 A/cm^2 , and with rise and fall times of < 20 ns, were measured by an avalanche photodetector and an oscilloscope with < 5 ns time resolution. The current pulse widths were monotonically decreased from $100 \text{ }\mu\text{s}$ at $J = 4 \text{ mA/cm}^2$ to $5 \text{ }\mu\text{s}$ at $J =$

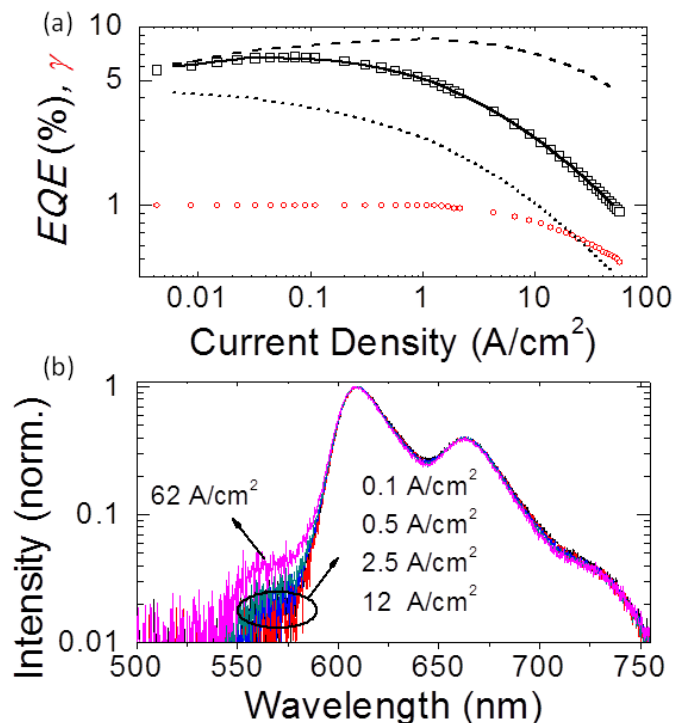


Figure 6.2 (a) External quantum efficiency (EQE , squares) and charge balance factor (γ , circles) vs. current density, J for the organic light emitting diode (OLED). The lines correspond to the calculated EQE from the model described in text; i.e. with both TTA and singlet-triplet annihilation (STA) present (solid line), in the absence of TTA (dotted line), and in the absence of STA (dashed line). (b) Emission spectra for the OLED at different J .

57 A/cm² to ensure the OLED EL intensity reached steady state, but did not undergo thermal or electrical breakdown. The emission intensity at $J = 4$ mA/cm² was calibrated using a Si photodetector whose area is significantly larger than that of the OLED [122]. All measurements were performed under N₂ ambient.

The OLED shows a peak $EQE = 6.7\%$ at $J = 75$ mA/cm² (Fig. 6.2 (a)), clearly exceeding the spin statistically limited $EQE = 5\%$ [162] assuming a random orientation of molecular dipoles. The EQE undergoes a rapid roll-off with increasing J , decreasing to only 0.9% at 57 A/cm². The EL spectrum of the OLED shows pure DBP emission with

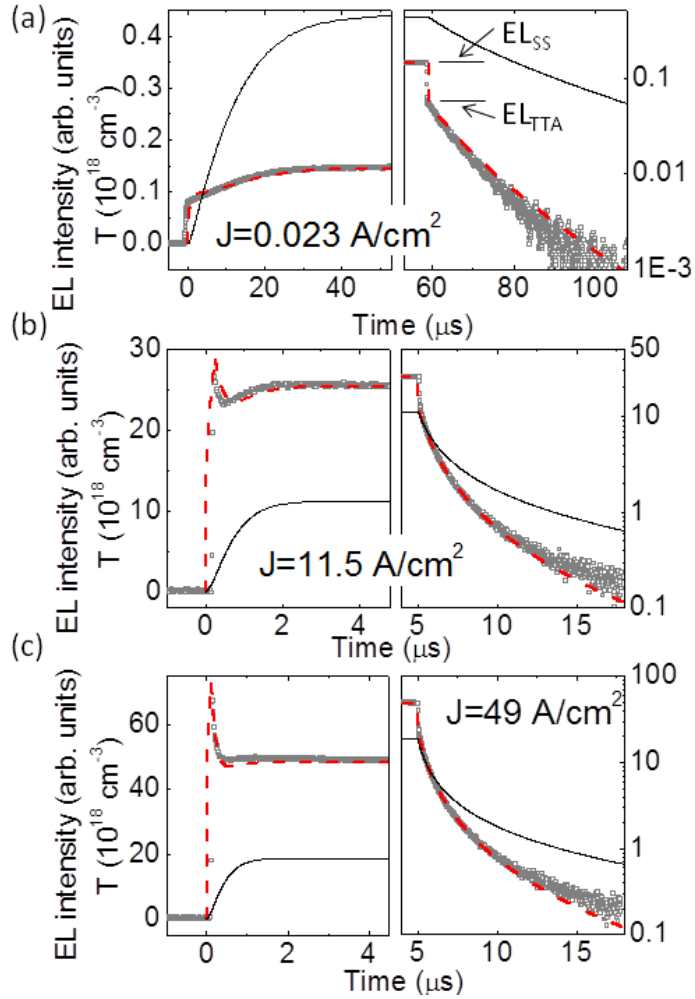


Figure 6.3 Electroluminescence (EL) turn-on (left graphs) and turn-off (right graphs) transients (grey squares) for the DBP doped rubrene OLED under a current density pulse at (a) $J=0.023 \text{ A/cm}^2$; (b) $J=11.5 \text{ A/cm}^2$; and (c) $J=49 \text{ A/cm}^2$. The red dashed lines are EL intensities assumed to be proportional to the singlet densities, and black solid lines are the corresponding triplet densities.

a peak wavelength of $\lambda = 610 \text{ nm}$ [161], as shown in Fig. 6.2 (b), with almost no change over the entire range of J studied.

To understand the high peak EQE followed by a rapid roll-off, we investigated the transient EL response. Figure 6.3 shows three representative EL transients at 0.023, 11.5 and 49 A/cm^2 . The EL turn-on transients have distinct behaviors at low (Fig. 6.3 (a),

left) vs. high (Fig. 6.3 (c), left) current densities. At low J , the EL intensity gradually increases to a steady state over tens of microseconds. This is consistent with TTA since the triplet density slowly increases over this time scale. In contrast, the transient in Fig. 6.3 (c) rapidly peaks and then gradually decays to a steady-state intensity approximately 70% of its peak value. This is a signature of STA [118], whereby the singlet density decreases with increasing triplet density. Figure 6.3 (b), left shows a mixture of both TTA and STA. The EL turn-off transients for all current densities show delayed fluorescence (right graphs in Fig. 6.3) due to TTA [56, 118]. The steady-state EL intensity, EL_{SS} , and the initial delayed fluorescence intensity, EL_{TTA} (see Fig. 6.3 (a), right), are related by the ratio, $\rho(J) = EL_{TTA} / EL_{SS}$ (as plotted in Fig. 6.4), which characterizes the fraction of TTA-generated-emission relative to the total emission intensity.

To quantitatively determine the relative contributions of TTA and STA, Eq's. (6.4) and (6.5) are fit to the experimental EL transients (where EL intensity is proportional to S) over $4 \text{ mA/cm}^2 < J < 57 \text{ A/cm}^2$. In these fits, the variables $\gamma(J)$, k_{ST} , and k_{TT} , are unknown, while k_S , k_T , and α can be independently measured. Here, $k_S = 1/\tau_S = (2.6 \pm 0.1 \text{ ns})^{-1}$ is obtained from the transient photoluminescence data for a 1% DBP: rubrene film [163]. Also, the rate $k_T = 1/\tau_T = (35 \pm 5 \text{ } \mu\text{s})^{-1}$ is determined from the triplet lifetime, equal to twice the EL decay time constant at $J = 4 \text{ mA/cm}^2$ at $>50 \text{ } \mu\text{s}$ from the current turn-off when TTA is much less efficient than the triplet natural decay [119]. Finally, $\alpha = 0.53$ is obtained from $\rho(J \rightarrow \infty) = 0.51$ (see Fig. 6.4) using Eq's. (6.4) and (6.5):

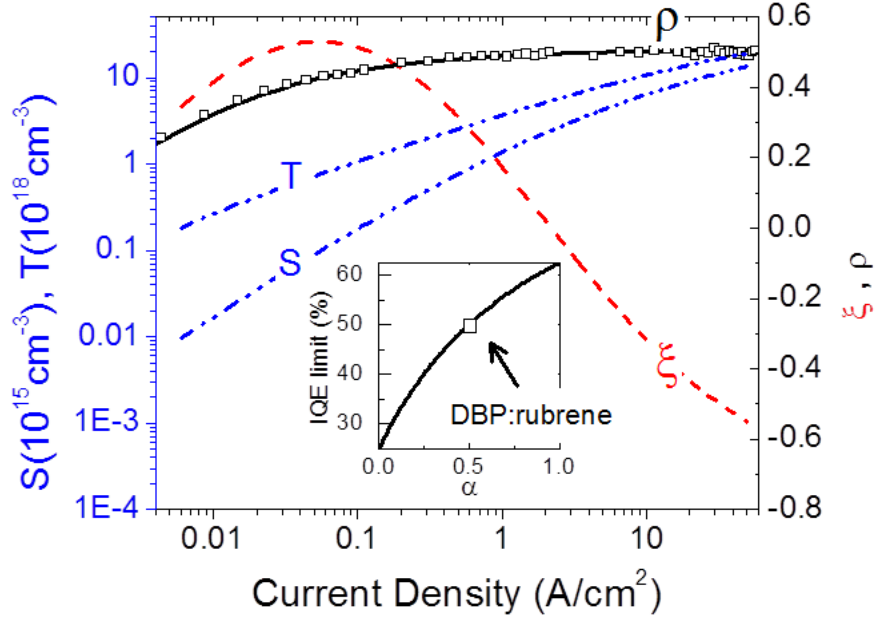


Figure 6.4 Calculated singlet (S) and triplet (T) densities (left axis), experimental (squares) and calculated (solid line) ratios of the delayed fluorescence EL to total EL (ρ , right axis), and the ratio ξ of the effective triplet current density (J_T) to J . Inset: Maximum internal quantum efficiency (IQE_{max}) for fluorescent OLEDs vs. the TTA generation ratio (α). The square shows IQE_{max} for the DBP doped rubrene OLED of this work.

$$\rho(J) = \frac{3\alpha k_{TT} T^2}{k_r T + (1 + \alpha) k_{TT} T^2 + 3\alpha k_{TT} T^2} \quad (6.7)$$

where, as $J \rightarrow \infty$, $k_r T$ is negligible, leading to $\lim_{J \rightarrow \infty} \rho = \frac{3\alpha}{4\alpha + 1}$.

According to Giebink, et al. [131], $\gamma(J)$ decreases with increasing J ; hence we assume $\gamma(J) = 1$ at $J = 4 \text{ mA/cm}^2$. From these measurements and assumptions, we can accurately determine $\gamma(J)$, k_{ST} , and k_{TT} by fitting the EL transients for all J .

The modeled EL transients closely follow the data in Fig. 6.3. By including both TTA and STA, the model fits the entire EL transient rather than just the turn-off, as in

previous reports [56, 57, 153]. From the fits, we find $k_{ST} = 7.1 \times 10^{-11} \text{ cm}^{-3} \text{ s}^{-1}$, $k_{TT} = 6.0 \times 10^{-14} \text{ cm}^{-3} \text{ s}^{-1}$, and $g(J)$ whose values are shown in Fig. 6.2 (a) (open circles). Since triplets are trapped on rubrene, DBP singlets are efficiently quenched by rubrene triplets. Also, since TTA is a short-range Dexter interaction, the high k_{TT} in rubrene suggests a high triplet diffusivity [107]. Finally, we find $g(J) \approx 1$ except at $J > 1 \text{ A/cm}^2$, after which it decreases due to charge leakage through the emissive layer, and field-induced exciton dissociation [131]. The leakage is evident in Fig. 6.2 (b), where the emission spectrum shows noticeable increase in the contribution from rubrene (at $\lambda = 550 \text{ nm}$) [164] at $J = 62 \text{ A/cm}^2$. We note that exciton-polaron annihilation [107, 115, 118] is also possible in fluorescent OLEDs; however, since inclusion of the process is not needed in the fits to the data, it is not anticipated to play a significant role.

With these experimentally determined rates, steady-state values for S and T are calculated and shown in Fig. 6.4. The model $EQE(J)$ in Fig. 6.2 (a) is then derived from S according to Eq. (6.7) using $\eta_{OUT} \eta_S = 17.3 \%$ obtained from the magnitude of $EQE(J)$. The peak $EQE > 5\%$ is a result of TTA, the scale of which can be characterized by ρ , also shown in Fig. 6.4. At $J < 0.1 \text{ A/cm}^2$, $k_{TT}T$ is comparable to k_T and increasing with J , resulting in the monotonic increase of $\rho(J)$. At $J > 1 \text{ A/cm}^2$, $k_{TT}T \gg k_T$ and thus ρ saturates according to Eq. (6.7). In general, the upper limit of

IQE is set by, $IQE_{max} = \frac{25\%}{(1-\rho)} = 25\% \times \frac{4\alpha+1}{\alpha+1}$, as plotted in the inset of Fig. 6.3. For the

OLED in this work, $\alpha = 0.53$, corresponding to $IQE_{max} = 51\%$. When $\alpha = 1$,

$IQE_{max}=62.5\%$, consistent with the result of Kodakov, et al. [56]. This upper limit can only be reached for $k_{TT}T \ll k_T$ and negligible STA.

6.2 Evaluation of the Role of Triplets in Fluorescent OLEDs

To evaluate the overall contribution of triplets to fluorescent OLED efficiency, we put both TTA and STA into the same context and define the effective triplet current density as:

$$J_T = \frac{4ed}{\gamma(J)} (\alpha k_{TT} T^2 - k_{ST} ST). \quad (6.8)$$

Then, Eq. (6.4) can be simplified to $\frac{dS}{dt} = \gamma(J) \frac{J}{4ed} [1 + \xi] - k_s S$ using the ratio, $\xi = J_T / J$. J_T (and also ξ) can be either positive or negative, depending on whether TTA or STA dominates. Note that when $\gamma(J) = 1$, $IQE = 25 \times (1 + \xi)\%$. Then, J_T (and also ξ) can generally be used as a figure-of-merit to evaluate the role of triplet in fluorescent OLEDs.

The calculated ξ for the OLED studied is shown in Fig. 6.4. With increasing J , ξ is initially positive and increases due to TTA to a peak of $\xi = 0.53$ at $J = 50 \text{ mA/cm}^2$; and then decreases due to the increased rate of STA. A critical current density, J_C can be defined when $\xi = 0$, and thus the effects of TTA and STA are equal. Above $J_C = 2.2 \text{ A/cm}^2$, ξ becomes negative and triplets lead to a decrease in quantum efficiency.

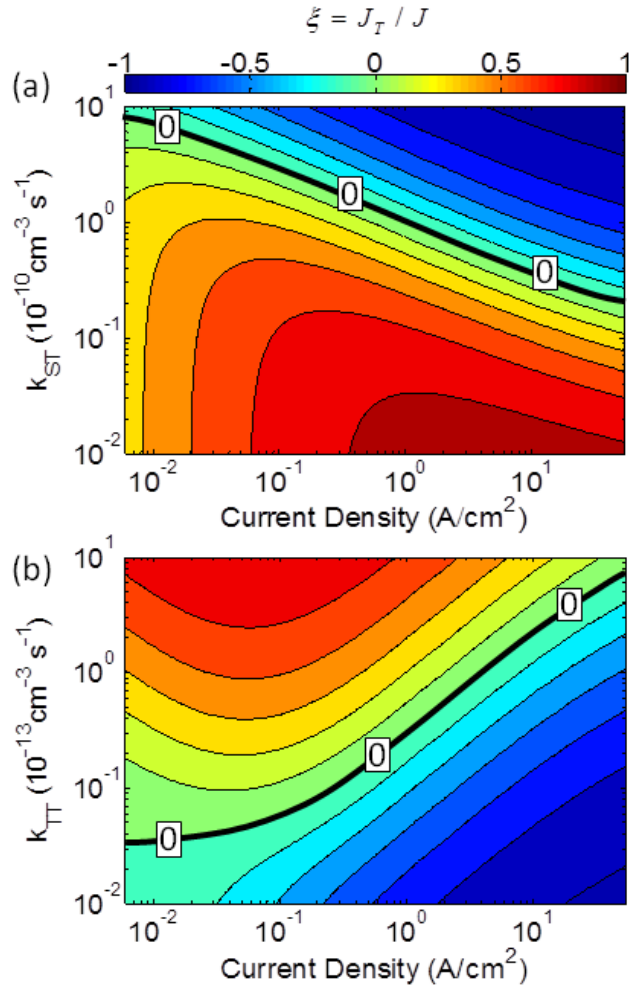


Figure 6.5 Ratio ξ vs. J , as a function of the (a) STA rate k_{ST} and (b) TTA rate k_{TT} , keeping other parameters as found for the DBP doped rubrene OLED. Here, “0” indicates the contour where triplets show no net contribution to OLED efficiency. Also, ξ changes by 0.15 between adjacent contours.

The dependence of ξ on J changes with k_{ST} and k_{TT} . In Fig. 6.5 (a), ξ vs. J is calculated for different k_{ST} while keeping other parameters constant. As k_{ST} increases, J_C decreases, as does ξ . In contrast, with increasing k_{TT} , both ξ and J_C increase (Fig. 6.5 (b)). Thus, besides requiring that $E_S \leq 2E_T$ to achieve a large α [56], fluorescent OLEDs with high EQE at high brightness also require a large k_{TT} and small k_{ST} . Now

k_{TT} is proportional to the triplet diffusivity [107] which increases with crystalline order [165], and k_{ST} is proportional to the overlap between the singlet emission and triplet absorption spectra, [4, 107] providing guidance in choosing materials that can lead to a high efficiency.

Based on J_T , two limiting cases of EQE in Fig. 6.2 (a) are calculated; one for $\alpha = 0$ (where TTA does not generate singlets according to Eq. (6.1)), and the other for $k_{ST} = 0$ (no STA). The differences between these calculated EQE 's and the data show the relative effects of TTA and STA that are responsible for the high peak EQE and rapid roll-off with J , respectively.

Singlet fission is a process in which one singlet shares its energy with a neighboring ground state, and both are converted into triplets [107, 166]. It requires that $E_S \geq 2E_T$. For each absorbed photon, two electron-hole pairs can be harvested, and thus fission has the potential of doubling the efficiency of excitonic solar cells [166-169]. In contrast, TTA through Eq. (1) is the reverse process of singlet fission, where we require that $E_S \leq 2E_T$. For rubrene, the singlet and triplet energies are in resonance, i.e. $E_S = 2E_T$ (Fig. 6.1). In this case, both efficient TTA and singlet fission can co-exist and compete [170]. When a rubrene-only emissive layer is used, then $EQE < 0.2\%$, indicating that singlet fission dominates over rubrene emission. On the other hand, resonant (Förster) singlet transfer from rubrene to DBP suppresses rubrene singlet fission, and thus the use of DBP as a dopant yields a peak EQE of 6.7%. From another perspective, fast Förster transfer of singlets represents a significant loss mechanism for singlet fission in excitonic solar cells, and should be avoided in those devices.

In conclusion, we develop a model that accurately describes singlet and triplet density dynamics in fluorescent OLEDs over more than four decades of current density. Based on this model, the dependence of the internal quantum efficiency limits of fluorescent OLEDs on TTA is obtained, explaining the high peak efficiency of 6.7% experimentally observed. The overall effect of triplets, including TTA and STA, is understood by introducing the concept of an effective triplet current density that is used to describe the efficiency roll-off at high current densities and brightness. Our model provides guidance for the appropriate design of molecules and device structures that can be used for high efficiency fluorescent OLEDs as well as organic photovoltaics employing singlet fission.

Chapter 7

Triplet Annihilation in Phosphorescent OLEDs:

Dexter-Mediated Triplet Diffusion

Although triplet-triplet annihilation (TTA) improves the efficiency of fluorescent OLEDs by generating singlets, it severely reduces the efficiency of phosphorescent OLEDs at high brightness. In this chapter, we study TTA in phosphorescent organic emitters by transient photoluminescence (PL) experiment. Previously, two distinct physical processes are used to explain the mechanism of TTA, namely, diffusion dominated TTA and triplet-to-triplet energy transfer dominated TTA. In section 7.1, by fitting PL to these two processes, we find that TTA in three representative phosphorescent emitters is diffusion dominated. Further, we show in section 7.2 that triplet diffusion in phosphorescent emitters occurs through Dexter-type exchange interactions, suggesting triplet radiative decay and TTA are independent processes. Based on the model, it is suggested in section 7.3 that minimizing the PL and absorption spectral overlap in phosphorescent emitters can lead to a significantly decreased TTA rate, and thus suppressed efficiency roll-off in phosphorescent organic light emitting diodes at high brightness.

7.1 Transient Photoluminescence in Phosphorescent Emitters

As shown in section 2.3, phosphorescent OLEDs (PHOLEDs) suffer efficiency roll-off (i.e. a decrease in external quantum efficiency (EQE) when the current density J increases) due to exciton interactions. Although some recent reports demonstrated PHOLEDs with reduced efficiency roll-off [61, 171-173], significant effort is required to reduce the efficiency roll-off at $> 3000 \text{ cd/m}^2$ required in high intensity applications such as lighting [174]. OLED displays also require low efficiency roll-off to compensate for losses due to limited pixel aperture ratios, luminance losses due to the use of circular polarizers and color filters, and losses due to the low light out-coupling for OLEDs deposited on large area substrates.

Factors causing PHOLED efficiency roll-off include charge imbalance, bimolecular triplet-polaron annihilation (TPA), and triplet-triplet annihilation (TTA) [52, 116, 117]. Among them, TTA has been identified as an intrinsic limit associated only with the phosphorescent emitter. In section 2.3, we show OLED efficiency drops to 50% of the peak value due to TTA when at a critical current density, $J_0 = \frac{2edk_T^2}{k_{TT}}$, where e is the electron charge, d is the OLED emissive layer width, k_T is the triplet decay rate, and k_{TT} is the TTA rate. Although TTA in phosphorescent systems has been studied by many [116, 117, 175, 176] in the past 15 years, there is not a clear path on how it is related to the phosphorescent emitter's photophysical properties. Thus, a simple emitter design rule to achieve low TTA does not exist.

In emitters with rapid singlet-to-triplet intersystem crossing, a single TTA event follows Eq. (2.42): $T + T \rightarrow S_0 + T^* \rightarrow S_0 + T$, where the first triplet T transfers its

energy to the second triplet, exciting it to T'' , which rapidly relaxes back to T , and S_0 represents the ground state. Since the rate of this reaction is a decreasing function of the distance between the two interacting triplets, a description of cumulative TTA events should include both triplet diffusion and triplet-to-triplet energy transfer.

Previously, Baldo et al. [116] analyzed TTA in phosphorescent thin films doped with archetype Pt and Ir complexes using a diffusion-based model. That analysis has been widely adopted in studying the photoluminescence (PL) transients and PHOLED efficiency roll-off. More recently, Staroske et al. [177] proposed a triplet-to-triplet energy transfer model that is consistent with PL transients in octaethylporphine platinum (PtOEP) doped in 4,4'-N,N'-dicarbazole-biphenyl (CBP) at low concentrations. Here, we evaluate the relative dominance of the two processes. Using PL transient data, we find that TTA is primarily the result of triplet diffusion for emitter concentrations practical for high efficiency PHOLEDs.

We adopt the model of Baldo et al. [116] for diffusion dominated TTA, which results from Smoluchowski's theory of coagulation [113] (see Eq. (2.33) – (2.37)):

$$\frac{dT}{dt} = -\frac{T}{\tau} - \frac{1}{2}k_{TT}T^2, \quad (7.1)$$

where T is the triplet density, t is time, τ is the triplet natural lifetime, and k_{TT} is the TTA rate constant. Equation (7.1) assumes that the triplet-to-triplet energy transfer rate is infinite when two triplets are within a capture radius, R_C , and zero outside [113]. The quadratic dependence of TTA on triplet density arises from counting the flux of triplets

onto the capture radius of each other during diffusion. Then, k_{TT} is related to triplet diffusivity, D , via [113]:

$$k_{TT} = 8\pi R_C D. \quad (7.2)$$

In the case of energy-transfer-dominated TTA where triplets are assumed to be immobile, Staroske et al. [177] and Engel et al. [178] derived a time dependent expression for k_{TT} from Förster transfer of energy between triplets,

$$k_{TT} = \gamma(t) = \frac{2}{3} \pi R_{FTT}^3 \sqrt{\frac{\pi}{\tau t}} \quad (7.3)$$

where R_{FTT} is the Förster radius for energy transfer from one triplet to another triplet, determined by,

$$R_{FTT} = \left[\frac{3\hbar^4 c^4}{4\pi n^4} \int \frac{1}{E^4} F_T(E) \sigma_T(E) dE \right]^{1/6} \quad (7.4)$$

where \hbar is the reduced Planck constant, c is the speed of light, E is the photon energy, n is the refractive index, $F_T(E)$ is the triplet emission spectrum normalized to its PL efficiency, Φ_{PL} (or $\int F_T(E) dE = \Phi_{PL}$), $\sigma_T(E)$ is the triplet absorption cross-section (in cm^2) calculated through its molar absorptivity via $\varepsilon = \sigma_T \times 6.02 \times 10^{20} \text{ M}^{-1} \text{cm}^{-1}$.

However, Eq. (7.3) in these previous reports is inaccurate due to inconsistencies in the derivations. For example, the derivation in [178] follows exciton donor-to-acceptor energy transfer dynamics first solved by Förster [179] and reviewed by many [180-182], in which the excited donor density $N_D(t)$ following a pulsed excitation are given by:

$$N_D(t) = n_0 \exp \left[-\frac{t}{\tau_D} - \frac{4}{3} \pi R_{DA}^3 \sqrt{\frac{\pi t}{\tau}} N_A \right], \quad (7.5)$$

where n_0 is the initial excited donor density, τ_D is its lifetime, R_{DA} is the donor-to-acceptor Förster radius (corresponding to the R_{FTT} for triplet-to-triplet energy transfer), and N_A is the density of acceptor sites which is time independent. Starting from Eq. (7.5), the authors of Ref. [178] assert a time dependent density of acceptor sites whereby $N_A = N_D$, leading to inconsistencies in their annihilation model. Such inconsistency is evident by solving Eq. (7.1) using Eq. (7.3) and (7.5) and setting $n(t) = T(t)$, which yields,

$$\text{left-hand side} = -T(t) \times \left[\frac{1}{\tau} + \gamma(t)T(t) + 2t\gamma(t) \frac{dT}{dt} \right], \quad (7.6)$$

$$\text{right-hand side} = -T(t) \times \left[\frac{1}{\tau} + \gamma(t)T(t) \right]. \quad (7.7)$$

Equation (7.7) differs from Eq. (7.6) by a factor related to $\frac{dT}{dt}$.

To derive triplet density dynamics of the triplet-to-triplet Förster transfer process, we assume triplets are evenly distributed on cubic lattice. The de-excitation rate of one triplet due to all other triplets is:

$$k_{FTT} = \frac{1}{\tau} \left(\frac{R_{FTT}}{a_T} \right)^6 \times \left[\frac{6}{(\sqrt{1})^6} + \frac{12}{(\sqrt{2})^6} + \frac{8}{(\sqrt{3})^6} + \dots \right], \quad (7.8)$$

where a_T is the average lattice constant given by $a_T = 1/\sqrt[3]{T}$. The series in Eq. (7.8) counts the contributions from the six nearest neighbors, the twelve second nearest neighbors, etc., and rapidly converges. Thus:

$$\frac{dT}{dt} = -\frac{T}{\tau} - \frac{1}{2} \beta_{TT} T^3, \quad (7.9)$$

where $\beta_{TT} \approx \frac{8}{\tau} R_{FTT}^6$ (7.10)

is the annihilation constant calculated from Eq. (7.8). In the following discussion, we refer to Eq. (7.1) as the diffusion model, and Eq. (7.9) as the triplet-to-triplet transfer model.

To compare the predictions of Eq. (7.1) and (7.9), we study three archetype phosphorescent emitters: tris (2-phenylpyridine) iridium ($\text{Ir}(\text{ppy})_3$) [51, 183], bis (2-phenylpyridine) (acetylacetonate) iridium ($\text{Ir}(\text{ppy})_2(\text{acac})$) [53, 183] and octaethylporphine platinum (PtOEP) [52], doped into a 4,4'-N,N'-dicarbazole-biphenyl (CBP) host. The chemical structures of these molecules are shown in Appendix A. A total of twelve 40 nm thick films with volume emitter concentrations $C = 2\%$, 4% , 8% , and 16% of each dopant were grown by vacuum thermal evaporation at base pressure $< 5 \times 10^{-7}$ Torr on quartz substrates. The films were excited using the output of a 20 Hz repetition rate, and 1 ns pulse width nitrogen laser at a wavelength of $\lambda = 337$ nm under an ultrahigh purity nitrogen environment. The laser beam focused on the films had a Gaussian profile with a full width at half maximum of $300 \mu\text{m}$, and its intensity was controlled by neutral density filters. The resulting PL transients were measured by a streak camera (Hamamatsu C4334) with a temporal resolution of 1 ns.

The PL transients for all twelve films with varied pump intensities are measured, and Fig. 7.1 show representative transients for 8% $\text{Ir}(\text{ppy})_3$ doped in CBP. The PL transient at the lowest pump intensity shows no TTA (corresponding to only a mono-exponential decay transient), while at the highest pump intensity, only negligible host emission is observed. An initial 2-D Gaussian triplet distribution results from the pump beam profile following: $T(r) = T_{00} \cdot e^{-r^2/2\sigma^2}$. Under our experimental conditions, this corresponds to the peak triplet density, T_{00} , varied from $1 \times 10^{16} \text{ cm}^{-3}$ to $2 \times 10^{18} \text{ cm}^{-3}$.

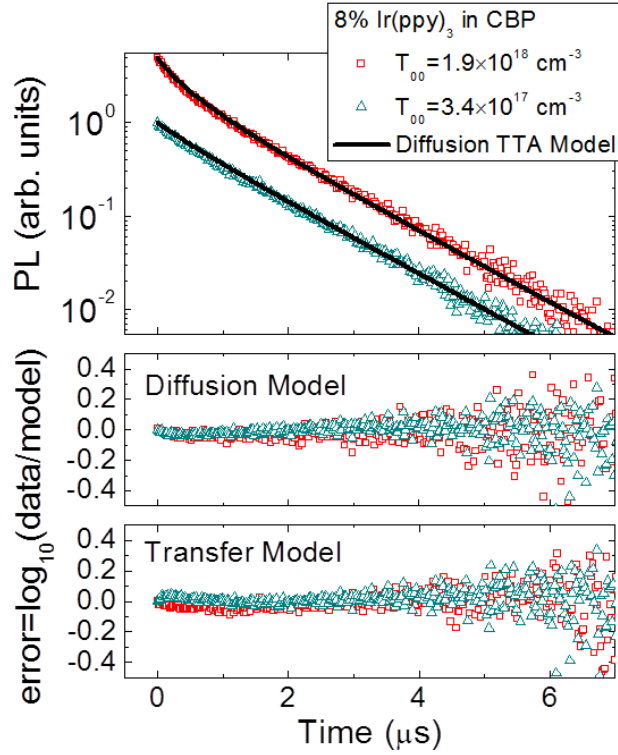


Figure 7.1 (a) Photoluminescence (PL) transients from 8% Ir(ppy)₃ doped in CBP with two different initial peak triplet densities. The solid lines are fits to the diffusion-dominated triplet-triplet annihilation (TTA) model. (b) and (c) show the residues of the fits based on diffusion and transfer models, respectively.

For the time ($\gg 1$ ns) and triplet density range studied, triplets only reside on the phosphorescent emitters due to the high CBP triplet energy of 2.6 eV compared to Ir(ppy)₃ (2.4 eV), Ir(ppy)₂(acac) (2.4 eV) and PtOEP (1.9 eV) [53, 132]. When using the diffusion or transfer model to fit the transients, we average the PL transients over the Gaussian profile. From Eq. (7.1), the PL transient is given by:

$$PL(t) = PL(t=0) \times \frac{2}{T_{00} k_{TT} \tau [\exp(t/\tau) - 1]} \times \ln \left[1 + \frac{1}{2} T_{00} k_{TT} \tau (1 - \exp(-t/\tau)) \right] \quad (7.11)$$

and from Eq. (7.9), the PL transient is:

Table 7.1 Parameters for the PL transients fits using the diffusion and transfer models

Vol %	τ (μs)	k_{TT} ($10^{-13} \text{ cm}^3\text{s}^{-1}$)	β_{TT} ($10^{-30} \text{ cm}^6\text{s}^{-1}$)	R_{FTT} (nm)
Ir(ppy)₃ in CBP				
2%	1.22±0.01	13±1	1.9±0.3	8.1
4%	1.19±0.01	21±1	3.3±0.4	8.9
8%	1.08±0.01	25±2	7.2±0.9	10.0
16%	0.94±0.01	36±4	17±3	11.2
Ir(ppy)₂(acac) in CBP				
2%	1.41±0.01	23±2	4.7±0.3	9.7
4%	1.22±0.01	32±2	8.9±1.1	10.5
8%	1.02±0.01	39±3	9.3±2.0	10.3
16%	0.67±0.01	50±5	28.1±4.0	11.5
PtOEP in CBP				
2%	98±2	0.13±0.02	(4.7±1.6)×10 ⁻³	6.2
4%	95±1	0.23±0.02	(7.7±1.5)×10 ⁻³	6.7
8%	88±1	0.41±0.03	(13±2)×10 ⁻³	7.2
16%	84±1	0.52±0.05	(9.4±2)×10 ⁻³	6.8

$$\begin{aligned}
 PL(t) = PL(t=0) \times \sqrt{\frac{2}{\tau T_{00}^2 \beta_{TT} (e^{2t/\tau} - 1)}} \times \\
 \ln \left[\sqrt{\frac{\tau T_{00}^2 \beta_{TT} (e^{2t/\tau} - 1)}{2e^{2t/\tau}}} + \sqrt{\frac{\tau T_{00}^2 \beta_{TT} (e^{2t/\tau} - 1)}{2e^{2t/\tau}} + 1} \right], \quad (7.12)
 \end{aligned}$$

where $PL(t)$ is the PL intensity proportional to total triplet population at time, t . We restrict the fit parameters τ , k_{TT} (diffusion model) or β_{TT} (transfer model) to be constant for a given film under different initial triplet densities, T_{00} . The fit results from all films are summarized in Table 7.1. Figure 7.1 (b) (c) show representative residues of

the fits to Eq. (7.11) and (7.12), respectively. The residues are small in both cases, and hence the two models cannot be distinguished based only on the fits.

7.2 Diffusion vs. Transfer Dominated Triplet Annihilation

From the transfer model results in Table 7.1, R_{FTT} can be calculated from τ and

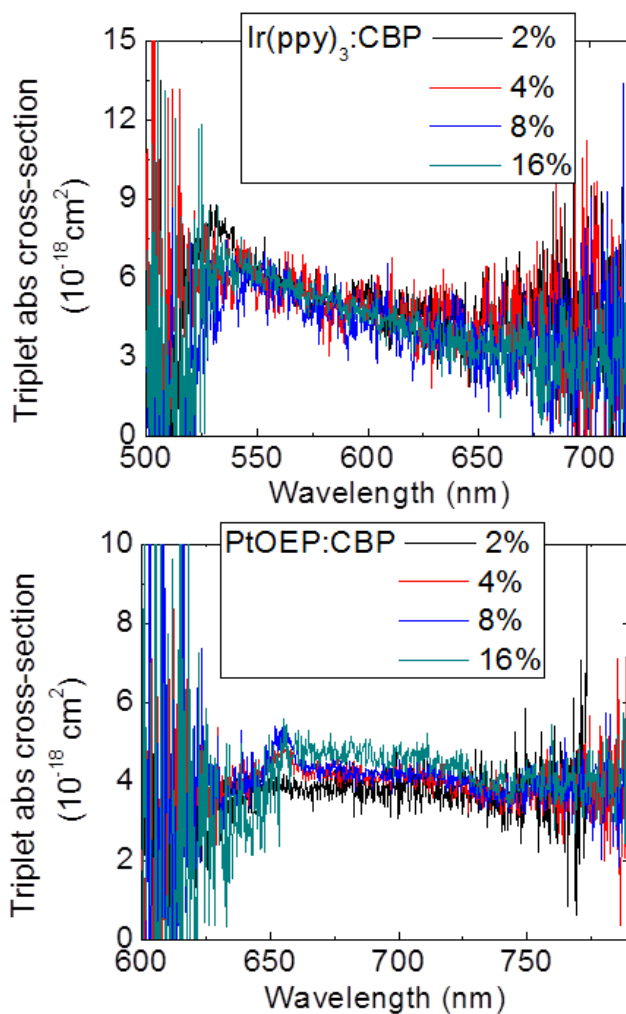


Figure 7.2 Triplet absorption cross-section spectra for Ir(ppy)₃ (top) and PtOEP (bottom) doped at different concentrations in CBP.

β_{TT} using Eq. (7.10), and is also shown in Table 7.1. The two Ir complexes show comparable R_{FTT} ranging from 8 nm to 12 nm, while the Pt complex shows a somewhat smaller $R_{FTT} \approx 7\text{nm}$. In all three cases, there is an increasing trend in R_{FTT} with doping concentration.

To understand the fit results, R_{FTT} can be estimated from Eq. (7.4) using the triplet emission and triplet absorption spectra. Figure 7.2 shows the triplet absorption spectra of Ir(ppy)₃ and PtOEP doped at different concentrations in CBP measured using the spatially separated pump-probe method [184]. Note that the PtOEP triplet absorption spectrum is similar in shape to that reported by Ponterini, et al. [185] for PtOEP in tetrahydrofuran solution, and close to the estimation of Staroske, et al. [177]. The spectra overlap between the triplet emission and absorption are plotted in Figure 7.3. Thus, using

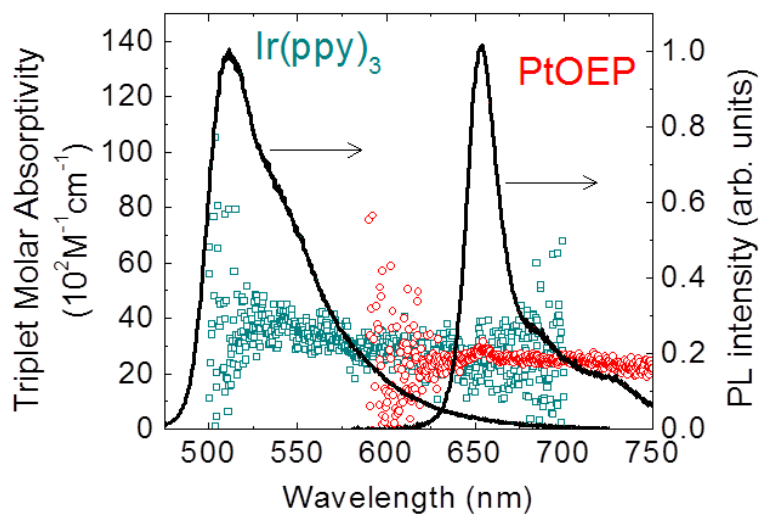


Figure 7.3 Molar absorptivity of triplets of Ir(ppy)₃ (open square) and PtOEP (open circle), as well as the corresponding PL spectra (lines). The spectra are measured from films at 8% doping concentration in CBP, although they are insensitive to doping (see Fig. 7.2).

literature values for Φ_{PL} ($\sim 100\%$ for the Ir-complexes [53, 186, 187] and $\sim 25\%$ for PtOEP [52, 55]), the Förster radius is calculated from Eq. (7.4) to be $R_{FTT} = 3.1$ nm for Ir(ppy)₃ and 2.7 nm for PtOEP.

Both the PL and triplet absorption are insensitive to doping concentrations [188]. Hence, the concentration dependence of R_{FTT} in Table 7.1 cannot be understood from the Förster transfer theory in Eq. (7.4). Furthermore, R_{FTT} obtained from the PL transient fits (Table 7.1) is larger than the calculation (in the previous paragraph) by a factor of 2 to 3, leading to 100-1000 times discrepancy in k_{FTT} or $\beta_{TT} \sim R_{FTT}^6$ (c.f. Eq. (7.10)). We note that although the cubic lattice model in Eq. (7.8) is an approximation, the significant difference between our fit and calculated k_{FTT} clearly invalidates the transfer model. Even at emitter concentrations as low as 0.1%, Staroske et al. [177] observed a factor of 1.44 discrepancy in Förster radii calculated from Eq. (7.4) and directly measured from PL transients, leading to nearly 10 times difference in Förster transfer rate. This large discrepancy was not considered significant by those authors.

The exciton diffusion model is based on triplet hopping from an excited to an unexcited emitter molecule. Two energy transfer mechanisms can be responsible for such hopping, Förster or Dexter-type [112, 163, 180], leading to two corresponding expressions for diffusivity:

$$D_F = a^2 k_{FH} = \frac{a^2}{\tau} \left(\frac{R_F}{a} \right)^6 \quad (7.13)$$

and
$$D_D = a^2 k_{DH} = a^2 KJ \exp\left(-\frac{2a}{L}\right), \quad (7.14)$$

where D_F and D_D are diffusivities due to Förster and Dexter transfer respectively, k_{FH} and k_{DH} are the corresponding hopping rates to a nearest neighbor, a is the dopant lattice constant related to C through $a = 1/\sqrt[3]{CN}$, where $N = 10^{21} \text{ cm}^{-3}$ is the film molecular density, R_F is the triplet-to-ground-state Förster radius, K is related to exchange interaction Hamiltonian, J is the density of states for energy transfer, and L is the effective Bohr radius. It is clear that the two mechanisms lead to significantly different functional dependence of D on a .

The experimental dependence of D on a can be derived from Eq. (7.2) and k_{TT} (see Table 7.1). Assuming R_C is independent of a , then Eqs. (7.2), (7.13), and (7.14)

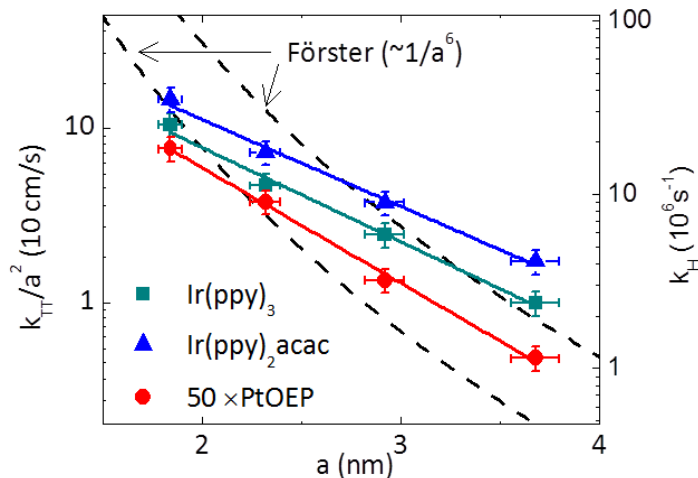


Figure 7.4 Comparison between two triplet diffusion mechanisms, Förster transfer (with $1/a^6$ dependence) and Dexter transfer (exponential dependence on a). The TTA rate constants, k_{TT} , are obtained from PL transient fit parameters in Table 7.1. The hopping rates, k_H , on the right-hand ordinate are calculated assuming a capture radius of 1 nm. Note that the data for PtOEP are multiplied by 50.

suggest that $k_{TT} / a^2 \sim 1/a^6$ for Förster-mediated diffusion, and follows an exponential function for Dexter diffusion. A comparison of the behavior of k_{TT} vs. a for the two mechanisms is shown in Fig. 7.4. For all three emitters, the data are consistent with Dexter diffusion; a conclusion consistent with Namdas, et al. [189] and Ribierre, et al. [176] for TTA in Ir-cored dendrimers. Assuming $R_C = 1$ nm, we also calculate the hopping rate $k_H = \frac{6k_{TT}}{8\pi a^2}$ on the right-hand ordinate of Fig. 7.4. From this we can estimate the average number of hopping steps that a triplet makes before collision with a second triplet by τk_H [176]. This process varies between 3 and 30 steps, depending on the doping concentration.

7.3 Emitter Design for High Brightness PHOLEDs

Interestingly, from Eq. (7.14), D_D and thus k_{TT} should be independent of τ ; however, k_{TT} for the two Ir-complexes is ~ 100 times greater for the Ir-complexes than for PtOEP, while their radiative lifetimes are only 1% of the PtOEP lifetime. This inverse correlation can be understood by evaluating J in Eq. (7.14) given by [112, 134]:

$$J = \int F_T(E) \sigma_{s_0}(E) dE \quad (7.15)$$

where $\sigma_{s_0}(E)$ is the absorption cross-section of the emitter molecular ground state.

Figure 7.5 shows absorption of a solution of Ir(ppy)₃, Ir(ppy)₂acac, or PtOEP dissolved in toluene at a concentration of 10^{-5} M. Here, diluted solution is adopted because a direct measurement of emitter absorption in host/emitter thin films is difficult,

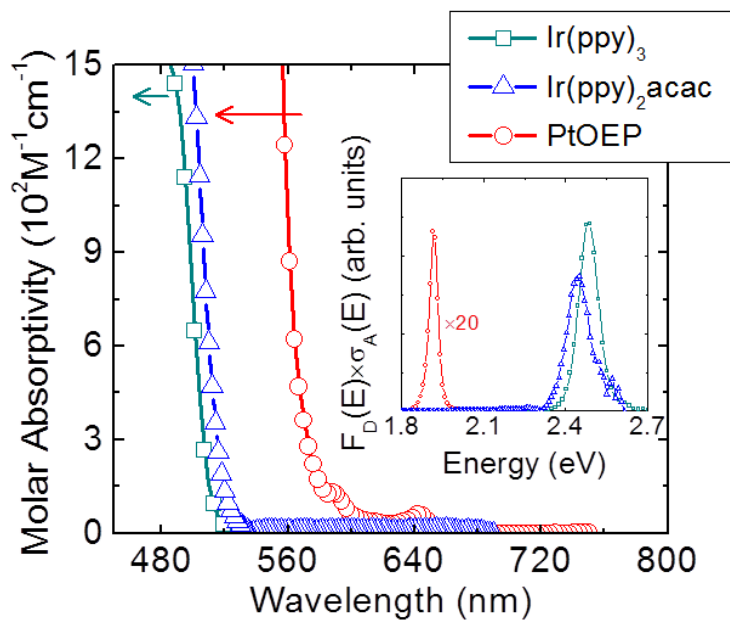


Figure 7.5 Absorption spectra of Ir(ppy)₃, Ir(ppy)₂acac, and PtOEP dissolved in toluene, shown only in the wavelength range of their corresponding PL spectra. The spectral overlap (or the product of the absorption and PL spectra at each photon energy) between the thin film PL and absorption in solution are shown in the inset.

and photophysical properties for these phosphorescent emitters' solutions typically resemble the amorphous films [190-192]. From the PL and absorption spectral overlaps (inset of Fig. 7.5), we find that $J(\text{Ir(ppy)}_3) \approx 50 \times J(\text{PtOEP})$. Since $k_{TT} \propto D_D \propto K \cdot J$ (Eq. (7.2) and (7.14)), then the difference in J between Ir(ppy)₃ and PtOEP must contribute to the observed ~100 times differences in the corresponding k_{TT} . On the other hand, Ir(ppy)₃ and Ir(ppy)₂acac have very similar spectral overlaps, which is consistent with their comparable k_{TT} values (Table. 7.1). That is, J for PtOEP is significantly smaller compared to that of the Ir-complexes because its absorption due to $S_0 \rightarrow T$ transition is weaker as a result of its reduced metal-ligand-charge-transfer (MLCT) contribution to the optical transitions characteristics of planar Pt compounds [51, 52, 190, 192].

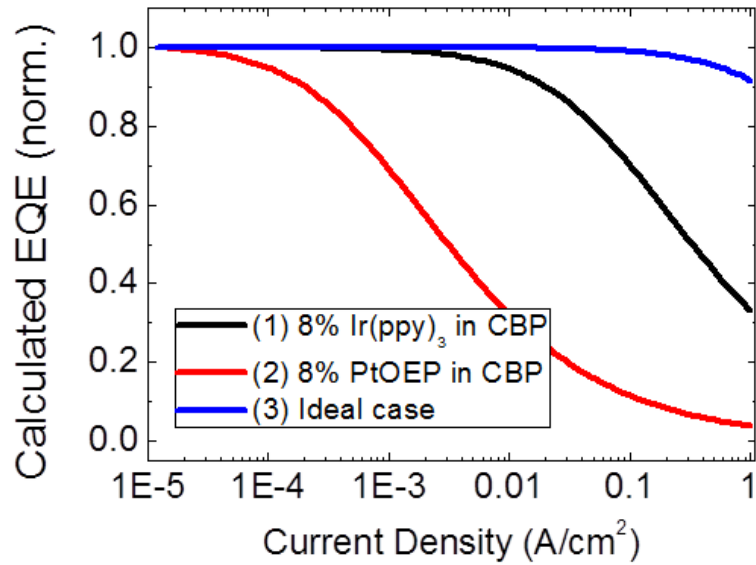


Figure 7.6 Calculated PHOLED efficiency roll-off due to TTA based on the parameters in Table 7.1. The ideal case is for an PHOLED emissive layer with triplet lifetime of 8% Ir(ppy)₃ in CBP and triplet-triplet annihilation rate of 8% PtOEP in CBP.

Since the “onset” current density for the roll-off in OLED efficiency at high current densities due to TTA is proportional to $1/(\tau^2 k_{TT})$ (see section 2.3 or [116]), the Dexter diffusion mechanism (Eqs. (7.2) and (7.14)) suggests that improved performance at high brightness is possible if τ and k_{TT} can be independently minimized. Figure 7.6 shows the calculated efficiency roll-off from Table 7.1 through Eq. (2.49) due to TTA for three PHOLEDs with 30 nm of EMLs consisting of (1) 8% Ir(ppy)₃:CBP, (2) 8% PtOEP:CBP, and (3) an ideal EML with τ of 8% Ir(ppy)₃:CBP and k_{TT} of 8% PtOEP:CBP. It is evident that simultaneous minimization of τ and k_{TT} is desirable for PHOLEDs operating at high current density (or luminance).

One means to accomplish this requires a high MLCT contribution to emission (leading to low τ) [134, 183] with a correspondingly large Stokes shift in the MLCT

absorption (leading to low k_{TT}). Previously [183], the importance of this Stokes shift has not been emphasized in phosphorescent emitter design since self-absorption is insignificant in PHOLEDs with doping concentrations and film thicknesses optimized for high efficiency emission.

The results here are in stark contrast to that of Staroske et al. [177], who conclude that TTA is dominated by triplet-to-triplet energy transfer, and proposed minimizing TTA through reducing the phosphorescent emitter PL and triplet-triplet absorption (from T to a higher triplet excited state) spectral overlap. Although at low emitter concentrations (< 1%), triplet-to-triplet energy transfer is more likely to dominate due to suppressed diffusion, the calculated [177] triplet-to-triplet transfer rate is off by nearly a factor of 10.

In conclusion, transient PL measurements in three prototype phosphorescent emitters suggests that TTA is dominated by triplet diffusion, and that direct triplet-to-triplet energy transfer [177], plays a considerably smaller role. Further, the diffusion of triplets follows the Dexter exchange interaction, in which the TTA rate is independent of triplet lifetime. Therefore, while maintaining the low triplet lifetime desirable for low efficiency roll-off in PHOLEDs, a reduced TTA rate can be achieved through decreasing the spectral overlap between the phosphorescent emitter absorption and emission. This understanding of energy transfer can be used to design efficient PHOLED emitters with reduced efficiency roll-off at high brightness.

Chapter 8

Controlling Triplet Dynamics to Extend the Operational Lifetime of Blue PHOLEDs

In previous chapters we studied exciton-exciton annihilation and its effects on the efficiency of OLEDs. Besides efficiency, operational lifetime is another significant figure-of-merit for OLED technology to gain commercial acceptance. Phosphorescent OLEDs (PHOLEDs) can harvest 100% of the electrical excitations, thereby having a significantly higher efficiency than fluorescent OLEDs. Unfortunately, the blue sub-pixels in OLED displays employ fluorescent OLEDs due to the short operational lifetime in blue PHOLEDs. In Section 8.1, we introduce the topic of OLED lifetime and review previous research on the degradation mechanisms of blue PHOLEDs. It has been suggested by Giebink et al. [193, 194] that triplet-polaron annihilation (TPA) between a triplet on the phosphorescent dopant and a polaron on the conductive host is the primary source of intrinsic degradation in blue PHOLEDs. In section 8.2, a novel PHOLED architecture is designed where the emissive layer (EML) consists of a linearly graded concentration phosphorescent dopant concentration profile. Grading results in low exciton density and thus suppressed TPA, leading to a significantly extended operational lifetime over conventional blue PHOLEDs. When two blue PHOLEDs are placed in a

series stack, as shown in section 8.3, this strategy leads to a 10-fold operational lifetime improvement over a conventional blue PHOLED.

8.1 Blue PHOLEDs Operational Lifetime: an Introduction

When an OLED operates under constant current with an initial luminance of L_0 , its operational lifetime ($T_X(L_0)$) is defined by the degradation time for the device efficiency to drop to X% of the initial efficiency. During the OLED luminance decay, its operational voltage continuously increases. Also, $T_X(L_0)$ decreases as L_0 increases.

Early reported OLED lifetimes based on Alq₃ as emitters are short. For example, Van Slyke et al. [195] reported a $T_{60}(510 \text{ cd/m}^2) \approx 3000 \text{ hrs}$, and Aziz et al. [196]

Table 8.1 Commercial OLED efficiency and lifetime

	CIE	Efficiency (cd/A)	T_{50} (1000 cd/m ²)
Phosphorescent OLEDs*			
Deep Red	[0.69, 0.31]	17	250,000
Red	[0.64, 0.36]	30	900,000
Yellow	[0.44, 0.54]	81	1,450,00
Green	[0.31, 0.63]	85	400,000
Cyan	[0.18, 0.42]	50	20,000
Fluorescent OLEDs**			
Red	[0.67, 0.33]	11	160,000
Green	[0.29, 0.64]	37	200,000
Blue	[0.14, 0.12]	9.9	11,000

*data from Universal Display Corp. <http://www.udcoled.com/> (2014)

**data from Idemitsu <http://www.idemitsu.com/> (2014)

reported a $T_{50}(1050 \text{ cd/m}^2) \approx 1000 \text{ hrs}$. After more than a decade of research, significant breakthroughs in green and red OLEDs lifetime have been achieved, with reported $T_{50}(1000 \text{ cd/m}^2)$ exceeding 10^6 hr [197-200]. Table 8.1 summarizes commercially produced OLED efficiencies and lifetimes. It is evident that red and green PHOLEDs are superior to analogous fluorescent OLEDs in both efficiency and lifetime. In contrast, progress in the improvement of blue PHOLED lifetime has been slow. For example, a $T_{50}(1000 \text{ cd/m}^2)$ of only several hours has been reported for a PHOLED with the blue emitting iridium (III) bis[(4,6-difluorophenyl)-pyridinato- N,C^2] picolinate (FIrpic) [201] as the emitter [202]. As a result, relatively inefficient blue fluorescent OLEDs remain dominant in OLED displays.

Factors leading to OLED degradation [31, 194, 196, 203] can be divided into two categories: extrinsic and intrinsic. Extrinsic factors include impurities in the molecules used for device fabrication, water and/or oxygen residues in the evaporation chamber (when pressure $> 5 \times 10^{-8}$ Torr), air leakage into the device package post-fabrication, etc. Intrinsic factors include molecular degradation (for example, bond cleavage) and organic film morphology change caused by charge transport, exciton non-radiative decay,

Table 8.2 Common molecular bond energy [3]

Bond	Energy (eV)	Bond	Energy (eV)
C-C	3.64	N-N	1.69
C-H	4.28	N-O	2.08
C-O	3.71	N-H	4.05
C-N	3.04	O-O	1.51
C-F	5.03	H-H	4.52

exciton-exciton annihilation, and exciton-polaron annihilation. Table 8.2 lists common molecular bond energies. It is clear that these energies (for example C-C, C-H, C-N) exceed 3 eV, which is higher than the first excited singlet or triplet energies typical in OLED materials. However, during exciton interactions (i.e. exciton-exciton or exciton-polaron annihilations), there is a possibility that twice the exciton energy can be thermally relaxed simultaneously onto a molecule, thereby breaking the bond.

Previously, Giebink et al. studied the degradation of a blue PHOLED with iridium (III) tris[3-(2,6-dimethylphenyl)-7-methylimidazo[1,2-f] phenanthridine] ($\text{Ir}(\text{dmp})_3$) doped in 4,4'-bis(3-methylcarbazol-9-yl)-2,2'-biphenyl (mCBP) as the emissive layer (EML). It was found that bimolecular triplet-polaron annihilation (TPA) is the intrinsic degradation mechanism in the blue PHOLED. As illustrated in Fig. 8.1, during TPA, the high energy blue triplet on $\text{Ir}(\text{dmp})_3$ transfers its energy to a polaron on mCBP, thereby exciton the polaron to a higher energy (i.e. as high as 6 eV) hot polaron

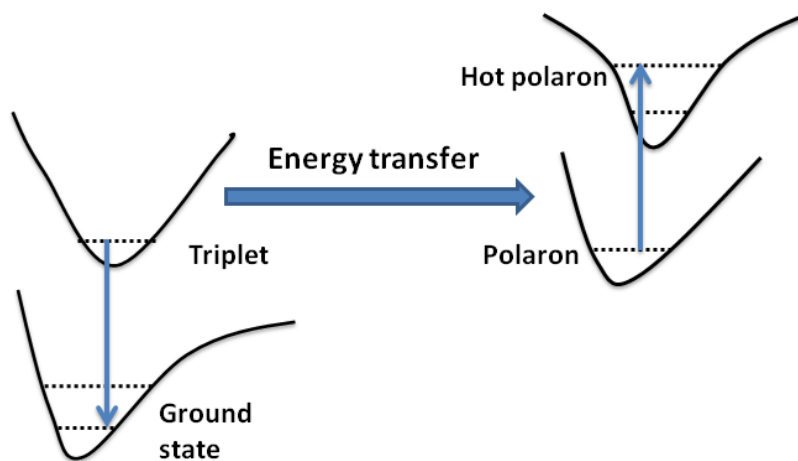


Figure 8.1 Illustration of triplet-polaron annihilation (TPA) and the formation of hot polaron. The hot polaron has approximately twice the triplet energy, which is enough to break molecular bonds.

state. The hot polaron, on thermalization, can break bonds on the molecule on which it resides, thus forming a defect in the EML, which can subsequently quench excitons as well as trap charges. The quantitative analysis of TPA induced PHOLED degradation is discussed in Section 8.3.

Due to their high triplet energy, excess energy dissipated through TPA in blue PHOLEDs is significantly higher than for red or green PHOLEDs, explaining the more rapid degradation in the former case. Furthermore, while blue fluorescent devices are by no means immune to this degradation path, their lower triplet energy leads to a proportionately greater probability for destructive exciton-polaron annihilation events to occur in phosphorescent devices.

8.2 Management of the Exciton Profile in PHOLEDs

While little progress has been made since these fundamental mechanisms were identified, it is possible that a route to reduce degradation via TPA is to decrease the exciton density in the PHOLED exciton formation zone. Recently, Erickson and Holmes [204] have demonstrated increased efficiency by the extension of the exciton formation zone in a green PHOLED from 15 nm to > 80 nm through graded mixing of electron and hole transporting host molecules. No lifetime data were reported in that work. Furthermore, the selection of stable host materials with high triplet energies for blue PHOLEDs is limited. Use of continuously or stepwise graded phosphorescent dopant profile in OLEDs was previously reported [205-207] to improve the OLED efficiency;

however, it is unclear whether the OLEDs exciton formation zones were extended in these reports and lifetime data were also unavailable.

In this section, we show that grading the blue *dopant* in the emitting layer (EML) of a PHOLED significantly extends the lifetime of the device by extending the exciton formation zone. The broadening of the exciton distribution, and hence the device lifetime, is further increased by using a sufficiently high dopant concentration, and with the dopant highest occupied molecular orbital level (HOMO) chosen above that of the host to allow for holes to conduct directly on the dopant. To our knowledge, this is the first report of an OLED with a graded doping profile that extends the distribution of excitons within the EML, thus significantly impacting device operational lifetime.

For this demonstration, we use the previously reported [194] blue dopant and host combination of Ir(dmp)₃ and mCBP, respectively. We compare three PHOLEDs (shown in Fig. 8.2) with the structures of 120 nm ITO/ 10 nm HATCN/ 50 nm X/ 5 nm mCBP/ 30 nm Alq₃/ 1.5nm Liq/ 100 nm aluminum:

in D1, X is 20 nm NPD/ 30 nm 13 vol% Ir(dmp)₃ doped in mCBP;

in D2, X is 50 nm 13 vol% Ir(dmp)₃ doped in mCBP;

in D3, X is 50 nm 18→8 vol% graded Ir(dmp)₃ doped in mCBP;

where ITO (indium-tin-oxide) is the anode, HATCN (hexaazatriphenylene hexacarbonitrile) is the hole injection layer (HIL), NPD (4,4'-bis[N-(1-naphthyl)-N-phenyl-amino]-biphenyl) is the hole transport layer (HTL), Ir(dmp)₃ doped mCBP is the EML, mCBP is the hole blocking layer (HBL), Alq₃ (tris(8-hydroxyquinolato) aluminum) is the electron transport layer (ETL), Liq (8-hydroxyquinolato lithium) is the electron injection layer (EIL), aluminum is the cathode. Device D4 is a two-unit

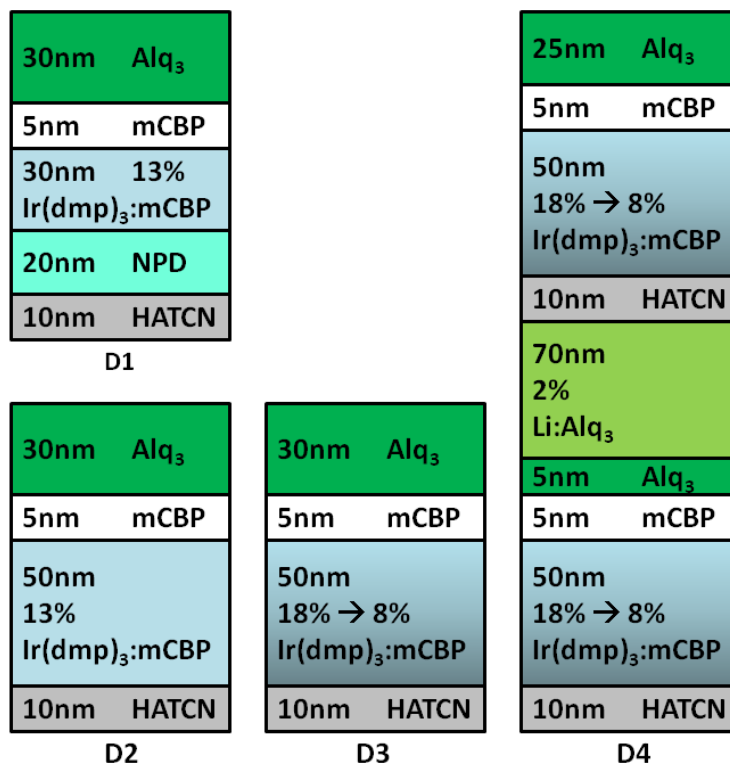


Figure 8.2 Structures of the blue phosphorescent organic light emitting diodes (PHOLEDs). Hexaazatriphenylene hexacarbonitrile (HATCN), 4,4'-bis[N-(1-naphthyl)-N-phenyl-amino]-biphenyl (NPD) and tris(8-hydroxyquinolinato)aluminum (Alq₃) are used for the hole injection (HIL), hole transport (HTL), and electron transport layer (ETL) materials, respectively. The EMLs of both D1 and D2 employ a 13 vol% doping concentration, and D2 replaces the HTL in D1 with EML. D3 has an EML with the doping concentration graded from 18 to 8 vol% with a maximum at the EML/HIL interface. D4 is a stacked OLED with two EMLs identical to D3.

stacked OLED (SOLED) with the structure: 120 nm ITO/ 10 nm HATCN/ 50 nm EML/ 5 nm mCBP/ 5 nm Alq₃/ 70 nm 2 vol% Li doped Alq₃/ 10 nm HATCN/ 50 nm EML/ 5 nm mCBP/ 25 nm Alq₃/ 1.5 nm Liq/ 100 nm aluminum, where the EMLs of the PHOLEDs comprising the stack are analogous to D3

Devices D1-D4 were deposited by thermal evaporation on pre-cleaned indium tin oxide (ITO)-on-glass substrates in a system with a background pressure of $\sim 5 \times 10^{-7}$ Torr. The PHOLEDs are packaged in an ultrahigh purity N₂-filled glovebox with < 0.5 ppm

oxygen and water concentration without exposure to air following film deposition, by attaching a glass lid to the substrate using an epoxy seal around the perimeter. Here, D1 is almost identical to the blue PHOLED reported previously [194], and serves as the control device.

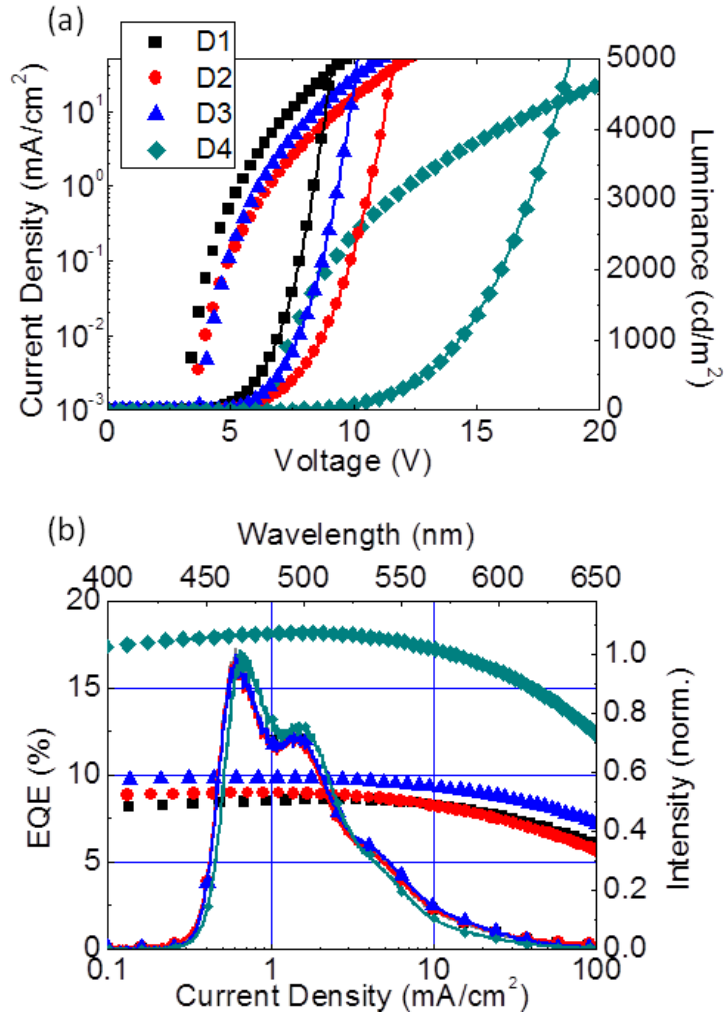


Figure 8.3 Performance characteristics of the blue PHOLEDs. (a) Current density-voltage (J - V , scattered markers) and luminance-voltage (L - V , line-connected markers) characteristics for D1-D4, where D4 is a stack of two blue emitting PHOLED whose EMLs are identical to D3. (b) External quantum efficiency (EQE) v.s. J (left axis) and emission spectra (right axis) for D1-D4.

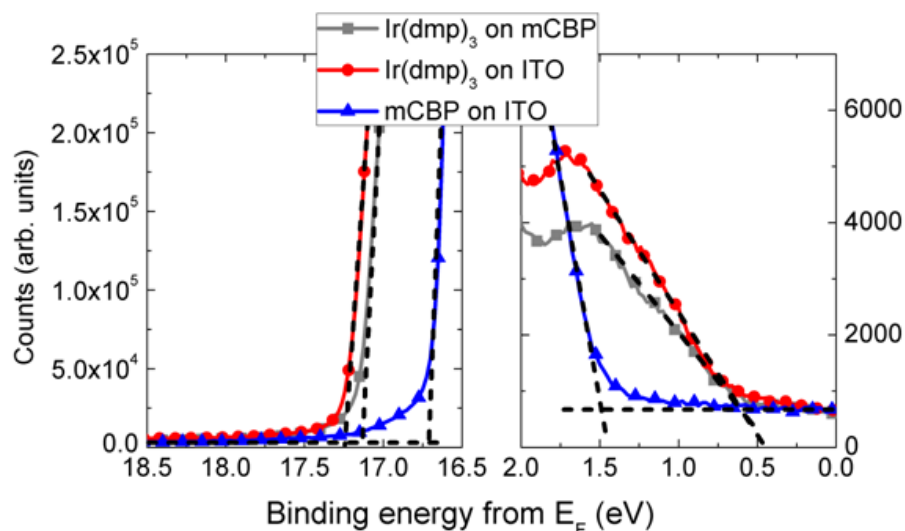


Figure 8.4 Ultraviolet photoelectron spectroscopy (UPS) data from molecules in the blue PHOLED emissive layer (EML)

Current density-voltage-luminance (J - V - L) characteristics were measured using a parameter analyzer (HP4145, Hewlett-Packard) and a calibrated photodiode (FDS1010-CAL from Thorlabs) following standard procedures [122]. Emission spectra were measured with a calibrated fiber-coupled spectrometer (USB4000, Ocean Optics) at $J = 10 \text{ mA/cm}^2$. The J - V - L , external quantum efficiency (EQE), and emission spectral characteristics of the four devices are shown in Fig. 8.3, and are summarized in Table 8.3. Replacing the HTL in D1 with an EML in D2 results in an increase in the operating voltage, as expected. Also, use of a graded doping profile in the EML (D3) decreases the voltage compared to the uniformly D2. Further, the emission spectra of all three devices are comparable, with the EQE of D1 and D2 being almost identical above 1 mA/cm^2 . The EQE of D3 is more than 10% higher than those of D1 and D2. As expected for a stacked OLED [208], D4 has approximately double the voltage and EQE compared with D3; for example, at 10 mA/cm^2 , D4 operates at a voltage of 17.4 V and $EQE = 17.2\%$ compared

Table 8.3 Characteristics at $L_0 = 1000 \text{ cd/m}^2$ for blue emitting PHOLEDs*

$L_0=1000 \text{ cd/m}^2$						
	CIE**	EQE	J	V	T_{80}	T_{50}
		(%)	(mA/cm^2)	(V)	(hr)	(hr)
D1	[0.16, 0.31]	8.5 ± 0.1	6.2	6.9 ± 0.2	56 ± 3	510 ± 15
D2	[0.16, 0.31]	8.5 ± 0.2	6.2	8.7 ± 0.3	-	-
D3	[0.16, 0.31]	9.5 ± 0.1	5.7	7.7 ± 0.2	213 ± 5	$1500^\dagger/1600^\ddagger$
D4	[0.15, 0.29]	18.0 ± 0.2	2.9	14.3 ± 0.1	616 ± 10	$3500^\dagger/3700^\ddagger$

* errors for EQE and V are standard deviations from at least 6 devices, errors for T_{80} and T_{50} are standard deviations from 3 devices

** Measured at 10 mA/cm^2

† Estimated from extrapolations using the triplet-polaron annihilation (TPA) model

‡ Estimated from extrapolation using the adjusted exponential (empirical) model

to 8.5 V and 9.3% for D3. This indicates a slight but measurable loss in the stacked device due to inefficiencies in charge generation in the layers between the stacked elements, and in the optical field distribution within the stack [209].

To understand the charge transport characteristics in the various EMLs, ultraviolet photoelectron spectra (UPS) were measured in an ultrahigh vacuum (UHV) analysis chamber using the illumination from the He I α line with 21.2 eV of energy. Figure 8.4 shows the UPS from 50 nm thick layers of mCBP and Ir(dmp)₃ on ITO, and 50nm-Ir(dmp)₃-on-50nm-mCBP on ITO. The highest occupied molecular orbital energies (HOMOs) of mCBP and Ir(dmp)₃ are $6.0 \pm 0.1 \text{ eV}$ and $4.6 \pm 0.1 \text{ eV}$ respectively. A dipole energy shift of $\sim 0.4 \text{ eV}$ is observed when Ir(dmp)₃ is deposited on mCBP, and thus the HOMO of Ir(dmp)₃ is $5.0 \pm 0.1 \text{ eV}$ on mCBP.

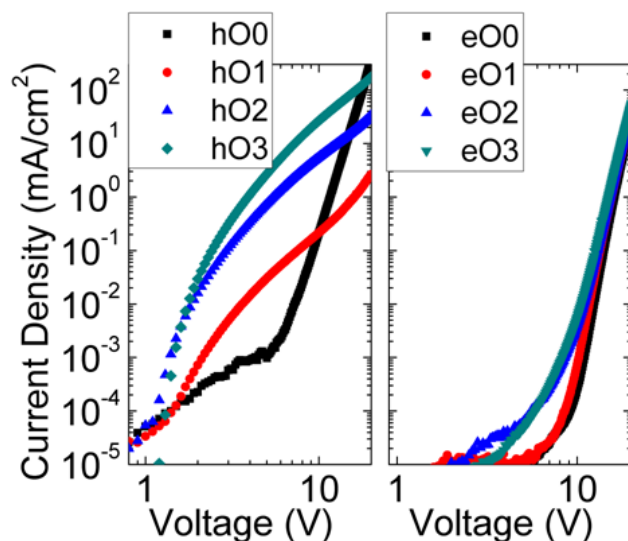


Figure 8.5 J - V characteristics of the hole-only (left) and electron-only (right) devices.

To further evaluate the electron and hole transport characteristics in the EMLs, hole-only (hO) devices with the structure: ITO/10 nm NPD/60 nm EML/10 nm NPD/100 nm Al, and electron-only (eO) devices with the structure: ITO/10 nm Alq₃/60 nm EML/10 nm Alq₃/1.5 nm Liq/100 nm Al were fabricated. The EMLs for these devices consisted of Ir(dmp)₃ doped mCBP at volume concentrations of 0% (hO0 and eO0), 8% (hO1 and eO1), 13% (hO2 and eO2), and 18% (hO3, hO3). Prior to the organic film depositions, the ITO-coated-glass substrates for hO0-hO3 were treated with UV-ozone for 10 min, whereas eO0-eO3 were not pre-treated.

The J - V characteristics for these devices are shown in Fig. 8.5. Clearly, J of hO devices increase with the increasing doping concentration of Ir(dmp)₃. This is consistent with the UPS result that hole transport in the EMLs is through Ir(dmp)₃. On the other hand, J of eO devices stays approximately the same at different Ir(dmp)₃ concentrations, suggesting that electron transport in the EMLs is through mCBP.

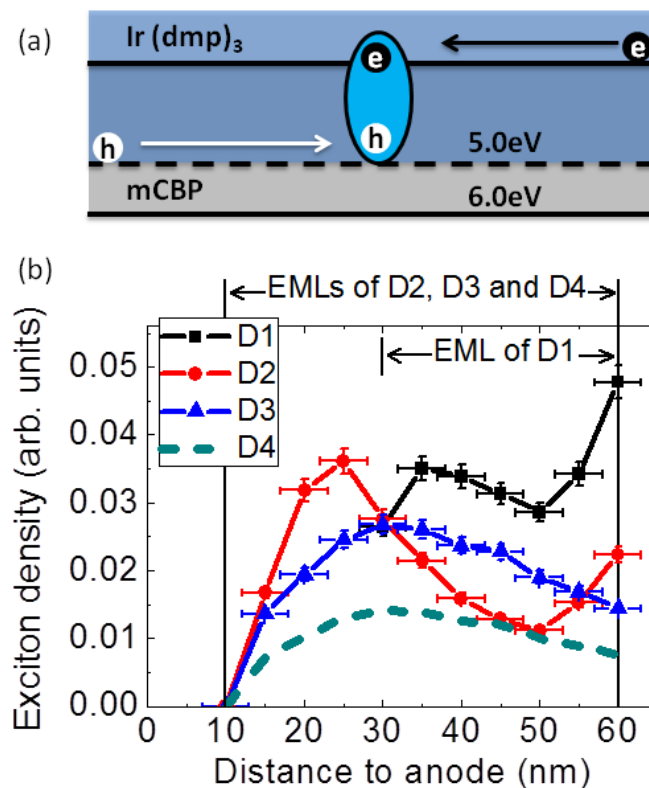


Figure 8.6 Energetics and exciton density profiles in the PHOLED EML. (a) Electron and hole transport and recombination energetics in the blue PHOLED EMLs. (b) Exciton density profile in the EMLs of D1-D3 calculated from “probe” devices employing iridium (III) bis(2-phenyl quinoly1-N,C²) acetylacetonate (PQIr) in the red light emitting sensing layer. The profiles are normalized to integrated exciton densities in the EMLs of unity. Also, the exciton density profile of D4 is calculated from the D3 profile.

In this unusual architecture, as shown in Fig. 8.6 (a) recombination occurs between an electron in the lowest unoccupied molecular orbital (LUMO) of mCBP, and a hole in the Ir(dmp)₃ HOMO, resulting in an exciplex. Since the PHOLED emission is solely from the phosphorescence of Ir(dmp)₃, the intermediate exciplex state rapidly transfers its energy to the Ir(dmp)₃ triplet. Note that the thermalization loss when an electron on mCBP recombines with a hole in Ir(dmp)₃ HOMO is 1.0 eV less than for a

hole in the mCBP HOMO, contributing to the relatively high operational stability in the blue PHOLEDs observed previously[194], and in D1 (see below).

The hole conductivity in the graded EML of D3 increases as the distance to the HIL/EML interface is decreased due to the increasing concentration of Ir(dmp)₃. In the opposite direction toward the EML/HBL interface, the hole conductivity decreases while the electron conductivity stays approximately constant. Thus, in contrast to the abrupt hole blocking by the EML/HBL interface in D1 and D2, in D3 the holes are gradually blocked by the hole conductivity gradient. As a consequence, exciton formation in D3 occurs over a more extended distance as compared to either D1 or D2.

To determine the hole blocking efficiency and thus the shape of the exciton formation zones in D1-D3, we fabricated a series of PHOLEDs with a thin, red emitting “sensing” layer using the dopant, iridium (III) bis(2-phenyl quinolyl-N,C^{2'}) acetylacetonate (PQIr) whose relative emission intensity can provide information about the spatial distribution of excitons in the EML. Here, PQIr is co-doped at 2 vol% at different positions separated by 5 nm in the EMLs of D1-D3, with a doping layer width of 1.5 nm. The HOMO and LUMO energies of PQIr are at 5.0 eV and 2.7 eV relative to the vacuum level, respectively [210]. Due to the low doping concentration and narrowness of the sensing layers, it should not significantly affect the charge transport or recombination properties in the EML. This is confirmed by the almost identical *J-V* characteristics between devices with and without sensing layers.

Local exciton densities $N(x)$ in the EMLs can be calculated from the measured emission spectra, external quantum efficiency, $EQE(x)$, and the calculated out-coupling

efficiency $\eta_R(x)$ (at a wavelength of 595 nm corresponding to the peak in the PQIr emission spectrum), from PHOLEDs with PQIr sensing layer at position x using:

$$N(x) = A \times EQE(x) \frac{N_R^{out}(x)}{N_R^{out}(x) + N_B^{out}(x)} \frac{1}{\eta_R(x)}. \quad (8.1)$$

Here, A is a normalization factor such that $\int_{EML} N(x) dx = 1$, $N_R^{out}(x)/N_B^{out}(x)$ is the out-

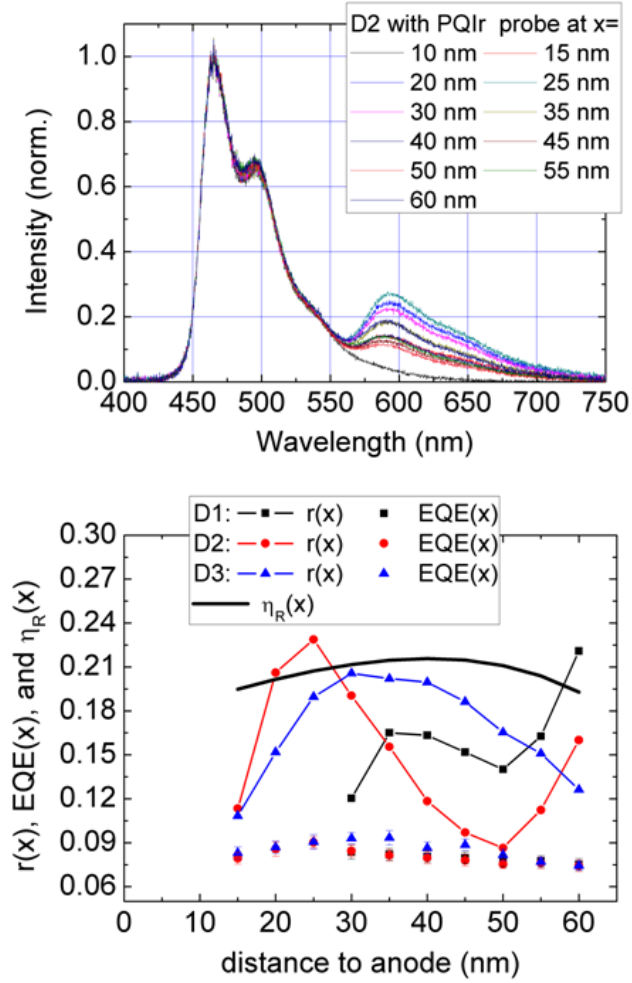


Figure 8.7 (top) Emission spectra from probe devices for D2 at $J = 10$ mA/cm^2 . (bottom) Parameters for calculating the exciton density profiles (see Eq. 8.1).

coupled photon number ratio from PQIr versus Ir(dmp)₃, obtained from the ratio of red

(I_R) and blue (I_B) peaks of the emission spectra through $\frac{N_R^{out}(x)}{N_B^{out}(x)} = \frac{I_R}{I_B} \frac{595\text{nm}}{466\text{nm}}$.

Representative emission spectra are shown in Fig. 8.7 (a) from the devices for the EML employed in D2. In Fig. 8.7 (b), we show $EQE(x)$ (at $J = 10 \text{ mA/cm}^2$),

$r(x) = \frac{N_R^{out}(x)}{N_R^{out}(x) + N_B^{out}(x)}$ (at $J = 10 \text{ mA/cm}^2$), and $\eta_R(x)$ (calculated following Celebi et

al. [211]) for the sensing OLEDs for D1-D3.

The calculated $N(x)$ from Eq. (8.1) is shown in Fig. 8.6 (b). In D1 (i.e. the conventional blue PHOLED), significant exciton accumulation occurs at the EML/HBL interface. In D2 where there is no HTL, the exciton density at the HIL/EML interface is reduced due to a correspondingly low concentration of holes. However, because of the reduced hole transport efficiency, electrons penetrate deep into the EML, resulting in a peak exciton density near the HIL/EML interface. In contrast, both efficient hole transport near the HIL/EML interface and the gradual hole blocking in the EML in D3 lead to a more uniform exciton distribution (and hence higher EQE) compared to D1 and D2, with a peak density near to the center of the EML. Since the EMLs of D3 and D4 are identical, also shown in Fig. 8.6 (b) is the exciton density profile of D4, estimated at 53% of the exciton density in D3 (at 10 mA/cm^2) due to the almost double EQE .

8.3 Ten-fold Improvement in the Lifetime of Blue PHOLEDs

Figure 8.8 shows the time evolution of the luminance, L , and the change in voltage from its initial value, $\Delta V = |V(t=0) - V(t)|$, for D1, D3, and D4 tested at room temperature and a constant current density for two initial luminances: $L_0 = 1000$ and 3000 cd/m^2 . Also, we show these same characteristics for D2 tested at $L = 3000$ cd/m^2 . The lifetimes show an increasing trend from D1 through D4. For example, $T_{80}(3000 \text{ cd/m}^2) = 11.5, 24.5, 39, \text{ and } 106$ hr, respectively, for D1-D4, consistent with the broadened exciton formation zone of the latter two devices (Fig. 8.6 (b)). Note that T_{80} for the control is consistent with similar results for this device reported previously⁶, and is only $\sim 29\%$ that of the graded device, D3. Further, $T_{80}(1000 \text{ cd/m}^2) = 616 \pm 10$ hr for D4, representing a more than 10 times improvement from the previously investigated [194] control, D1. The improvement in T_{50} for D4 is slightly less significant than T_{80} , leading to an approximately seven-fold increase from D1.

To establish a quantitative relationship between the exciton density profiles and operational lifetimes, we model L and ΔV as functions of time, t , following the model of Giebink et al. [194]. The model considers trap (with density $Q(x, t)$) formation due to TPA, and subsequent interactions with electrons with density $n(x, t)$, holes with density $p(x, t)$, and excitons with density $N(x, t)$:

$$G(x) - k_L n(x, t) p(x, t) - k_{Qn} Q(x, t) n(x, t) = 0 \quad (8.2)$$

$$G(x) - k_L n(x, t) p(x, t) - k_{Qp} Q(x, t) p(x, t) = 0 \quad (8.3)$$

$$k_L n(x, t) p(x, t) - \left(\frac{1}{\tau_N} + k_{QT} Q(x, t) \right) N(x, t) = 0 \quad (8.4)$$

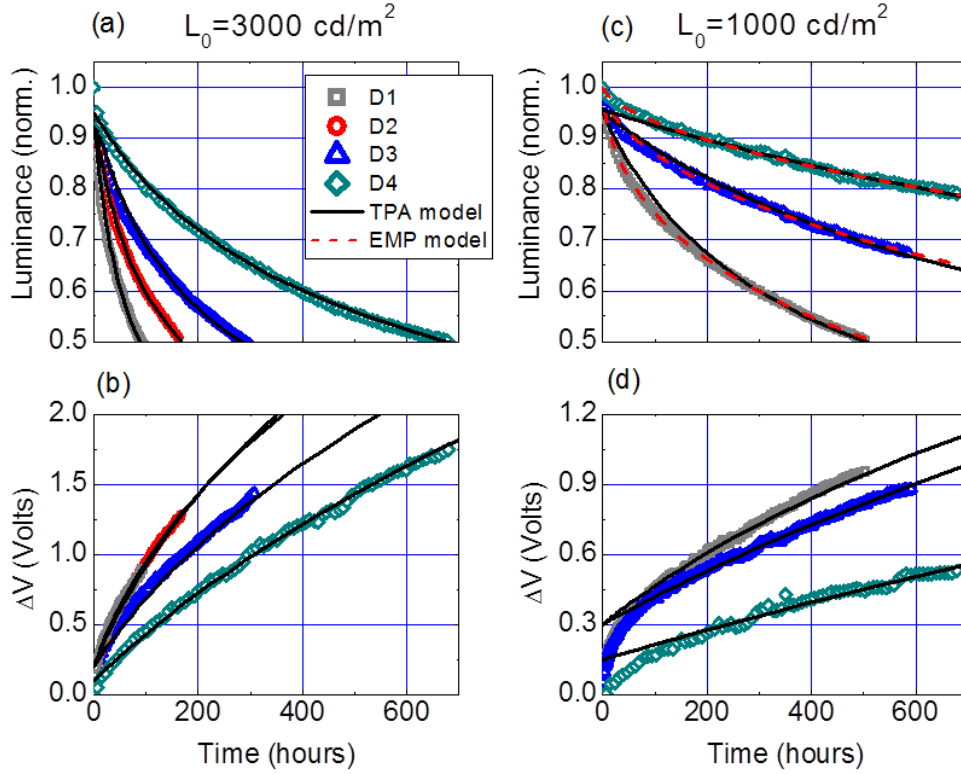


Figure 8.8 Time evolution of the normalized luminance, L , of blue PHOLEDs and change in operating voltage ΔV (offset to zero) at the initial luminance of $L_0 = 3000 \text{ cd/m}^2$ ((a) and (b)) and 1000 cd/m^2 ((c) and (d)). The data are fit to a triplet-polaron annihilation (TPA) model using the exciton density profiles in Fig 3 (b). The luminance for $L_0 = 1000 \text{ cd/m}^2$ (c) are also fit to the adjusted exponential (empirical, or EMP) model to estimate T50 (i.e. degradation time leading to 50% decrease in L_0).

where k_L is the Langevin recombination rate, k_{Qn} is the trap-electron interaction rate, k_{Qp} is the trap-hole interaction rate, k_{QT} is the trap-triplet annihilation rate, τ_N is the triplet lifetime, and $G(x)$ is the local recombination rate, calculated from the local exciton

density $N(x)$ using $G(x) = \frac{J}{e} \frac{N(x)}{\int N(x) dx}$, where e is the electron charge. Current densities

at $L_0 = 1000 \text{ cd/m}^2$ are provided in Table 1, and at 3000 cd/m^2 are $J = 21, 21, 17.5,$ and 9.1 mA/cm^2 for D1, D2, D3, and D4, respectively. Trap formation is attributed to TPA at a rate of k_Q using:

$$\frac{dQ(x,t)}{dt} = k_Q N(x,t) n(x,t) \quad (8.5)$$

Then, the OLED degradation can be calculated through,

$$L(t) = B \int N(x,t) \eta_B(x) dx \quad (8.6)$$

$$\Delta V(t) = \Delta V(0) + \int \frac{e}{\varepsilon \varepsilon_0} x Q(x,t) dx \quad (8.7)$$

where B is a normalization factor, $\eta_B(x)$ is the calculated out-coupling efficiency (for Ir(dmp)₃ emission peaked at 466 nm), $\varepsilon = 3$ is the relative permittivity, and ε_0 is the vacuum permittivity.

The model is fit to the degradation of D1-D4 with k_Q and k_{QR} as free parameters; all other parameters are as previously determined for this materials combination [194] (see Table 8.4). Yamamoto et al. [212] reported that water contamination of organic films during deposition leads to an accelerated initial degradation when the deposition background pressure is $> 5 \times 10^{-8}$ Torr for PHOLEDs almost identical to D1. In our case, organic films were deposited in a system with a base pressure of 5×10^{-7} Torr. However, the TPA model ignores extrinsic effects such as water contamination. To account for these effects in our fits, $t = 0$ corresponds to a normalized luminance of 0.95, and the initial value of ΔV was chosen to be nonzero (i.e. $\Delta V(0) = 0.2$ V (at 3000 cd/m²) and 0.3 V (at 1000 cd/m²) for D1-D3, and 0.1 V (at 3000 cd/m²) and 0.15 V (at 1000 cd/m²) for D4.).

From Table 8.4, k_Q and k_{QN} in D1 and D2 are almost identical, suggesting that improvement of the operational lifetime from D1 to D2 is simply a result of changes in

Table 8.4 Lifetime fitting parameters for blue emitting PHOLEDs

	D1	D2	D3	D4
Triplet-polaron annihilation (TPA) model				
Fixed parameters	$k_{Qn} = 1.44 \times 10^{-13} \text{ cm}^3 \text{ s}^{-1}$, $k_{Qp} = 4.8 \times 10^{-14} \text{ cm}^3 \text{ s}^{-1}$, $k_L = 1.7 \times 10^{-13} \text{ cm}^3 \text{ s}^{-1}$, $\tau_N = 1.1 \text{ } \mu\text{s}$			
$k_Q (10^{-11} \text{ cm}^3 \text{ s}^{-1})$	1.0±0.1	1.1±0.1	0.95±0.1	0.9±0.1
$k_{QT} (10^{-24} \text{ cm}^3 \text{ s}^{-1})$	7±1	7±1	6±1	7±1
Adjusted exponential (empirical) model				
$\tau (10^3 \text{ hrs})$	1.03±0.01	-	2.96±0.04	6.74±0.10
β	0.54±0.01	-	0.58±0.01	0.63±0.01

the exciton density profile. In D3, the significant increase in lifetime is due to the increase in *EQE* (leading to a decrease of *J* to achieve a given *L₀*), as well as to the significant spreading of the exciton formation zone compared to the former devices. Note that the TPA model considers degradation in the thin film bulk, but not at the interface [213]. Indeed, the low exciton density at the EML/HBL interface in D3 may also contribute to the observed increase in lifetime by reducing the rate of damage at this interface.

To estimate $T_{50}(1000 \text{ cd/m}^2)$ for D3 and D4, we extrapolate the times obtained from the TPA model fits. In addition, an empirical method often employed to model OLED degradation uses the adjusted exponential decay function: [214]

$$L(t) = \exp\left[-\left(t/t\right)^{\beta}\right].$$

Here, τ and β are phenomenological parameters. This model

also results in reasonable fits to the degradation data (Fig. 8.8 (c)), and provides extrapolated values for $T_{50}(1000 \text{ cd/m}^2)$ similar to those obtained from the physics-based TPA model (Table 8.3). From these fits, $T_{50}(1000 \text{ cd/m}^2) = 3500 \text{ hr}$ for D4, which

approaches that of blue fluorescent OLEDs with $T_{50}(1000 \text{ cd/m}^2) \sim 10^4 \text{ hr}$ (Table 8.1). Note that the emission from D1-D4 is light blue (although more saturated than the cyan color of FIrpic). However, color tuning to achieve more saturated blue emission is commonly achieved in fluorescent blue display sub-pixels through the use of microcavities[215, 216] and/or color filters. For example, a 70 nm thick anode of indium-tin oxide (ITO) yields Commission Internationale d'Eclairage chromaticity coordinates of [0.16, 0.26], compared to [0.16, 0.31] for a 120 nm thick ITO layer due to weak microcavity effects.

Although the blue PHOLED lifetime reported here remains substantially less than that of red and green PHOLEDs at similar luminances, blue sub-pixels in displays operate at a considerably lower luminance than either the red or green sub-pixels. For example, the required luminance to achieve an sRGB color gamut [217] for green is 9.9 times the luminance for blue. Thus, a comparison between blue and green PHOLED lifetimes for displays suggests that the blue PHOLED sub-pixel luminance needs to be only ~10% that of the green. Under such conditions, the TPA model estimates the blue PHOLED lifetime is $T_{50}(100 \text{ cd/m}^2) \approx 70,000 \text{ hr}$. Also, adopting a degradation acceleration factor that relates luminance to lifetime [214], *viz.*

$$T_{50}(100 \text{ cd/m}^2) = T_{50}(1000 \text{ cd/m}^2) \times \left[\frac{1000 \text{ cd/m}^2}{100 \text{ cd/m}^2} \right]^n \text{ and } n = 1.55, \text{ the extrapolated blue}$$

PHOLED lifetime is $T_{50}(100 \text{ cd/m}^2) \approx 1.3 \times 10^5 \text{ hr}$. These extrapolated lifetimes approach the commercial green PHOLED lifetime of $T_{50}(1000 \text{ cd/m}^2)$.

In summary, we demonstrated a ten-fold increase in blue PHOLED lifetime employing an extended exciton formation zone achieved by grading the concentration profile of the hole conducting phosphorescent dopant in the EML. Considering the

different color sub-pixel luminances used in displays, the improved blue PHOLED lifetimes achieved in stacked devices approaches that of green PHOLEDs under normal operating conditions. The novel device architecture employed is based on a fundamental physical understanding of the relationship between energy-driven triplet-polaron annihilation and device degradation, and hence should be generally applicable to a wide range of phosphorescent and fluorescent devices. Further lifetime improvements are anticipated by finding dopant/host combinations with conduction properties similar to the materials used here, and that minimize interactions between triplets on the dopant and polarons on the host molecules, therefore decreasing the probability of occurrence for high energy TPA interactions that lead to molecular decomposition.

Chapter 9

Future Work

The field of organic electronics is still in its infancy compared to the mature field of inorganic semiconductors. Many unique features of organics can be utilized for applications that are difficult or impossible to achieve with inorganic materials. This chapter explores the feasibility of two novel organic optoelectronic devices: a singlet fission organic coating for photovoltaics and an electrically pumped organic semiconductor laser.

9.1 A Singlet Fission Organic Coating for Photovoltaics

Singlet fission is a process where one singlet with high energy is converted to two triplets with lower energy [166], and is the reverse (Auger-like) process of triplet-triplet annihilation (TTA in Eq. 2.41). It is highly efficient in some organic materials and has the potential of doubling the external quantum efficiency (*EQE*) and thus increasing the power conversion efficiency (*PCE*) of organic photovoltaics (OPVs). However, although OPVs with *PCE* > 10% [73] have been demonstrated over the past two years, they are still far behind the inorganic PV performance.

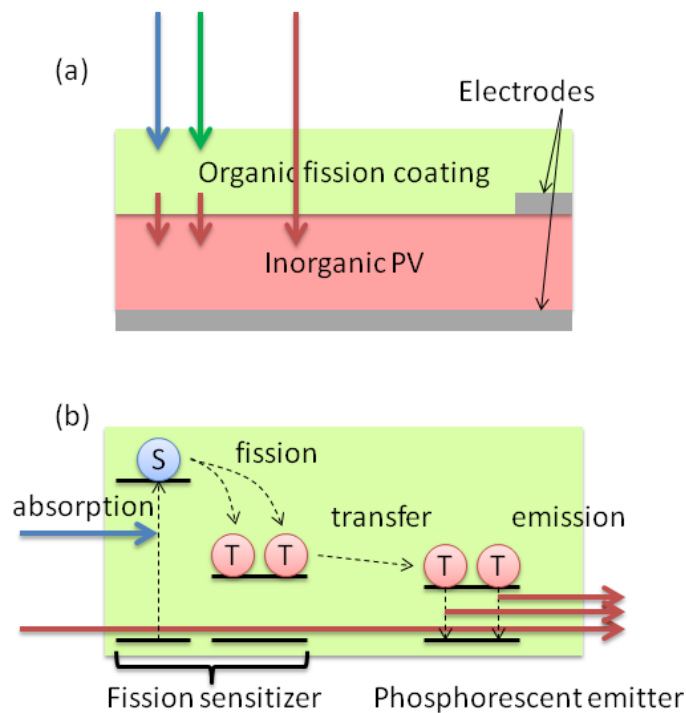


Figure 9.1 Structure (a) and operation principle (b) of the proposed singlet fission organic coating for photovoltaic applications.

A viable approach to combine the unique singlet fission process in organics and achieve a high PCE in inorganic PVs is shown in Fig. 9.1. Here, a organic “fission coating” is deposited on the front surface of an inorganic solar cell. The organic thin film consists of two types of molecules, a singlet fission sensitizer doped with a phosphorescent emitter. The fission sensitizer has a singlet energy higher than twice its triplet energy to facilitate resonant exothermic singlet fission [166], and the phosphorescent emitter has a lower triplet energy than the sensitizer. During operation, the ultraviolet (UV) and blue part of solar spectrum is absorbed by the sensitizing layer, where one singlet undergoes fission to form two triplets. The triplets on the sensitizer are transferred to the phosphorescent emitter and then decays radiatively, resulting in red or infrared (IR) emission subsequently absorbed by the inorganic PV. The green, red, and IR

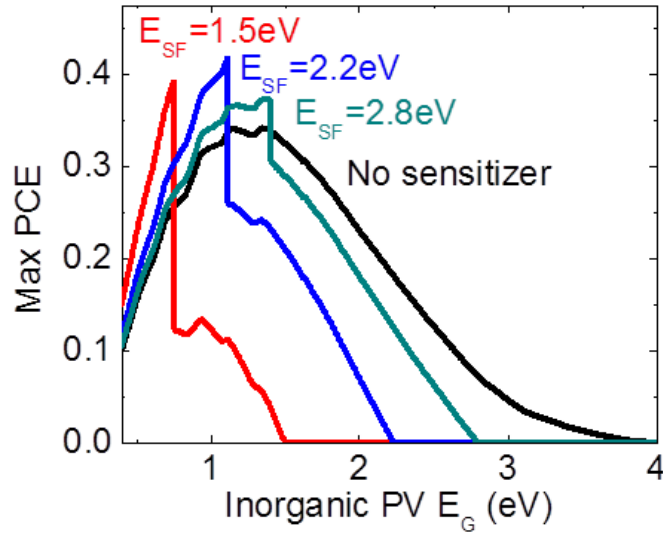


Figure 9.2 Calculated maximum power conversion efficiency (PCE) based on detailed balance theory [2] using an organic fission sensitizer with the singlet energy of E_{SF} on an inorganic photovoltaic (PV) cell with a band gap of E_G .

part of the solar spectrum transmits through the organic film and is directly absorbed by the inorganic PVs.

To evaluate the impact of this approach, we calculate the PV efficiency improvement based on the singlet fission coating. The calculation is based on the detailed balance approach of Shockley and Queisser [2] assuming that the organic film absorbs 100% of the solar spectrum above its bandgap of E_{SF} , and emits photons with the energy of $\frac{1}{2}E_{SF}$ at 200% photoluminescence quantum efficiency. Also, the inorganic solar cell bandgap is E_G , and the organic film is transparent to photon energies below E_{SF} . The calculated *PCE* limit as a function of E_G is shown in Fig. 9.2 for different E_{SF} . It is evident that the conventional SQ limit of 33.7% (black line) for single junction solar cell can be improve to as high as 42% (blue line) for the case of $E_{SF}=2.2$ eV and $E_G=1.1$ eV. Interestingly, this optimized inorganic band gap is the same as the bandgap of silicon.

The next question is whether such a combination of organic fission sensitizer and phosphorescent emitter already exists in the literature. Some promising combinations include the use of diphenylisobenzofuran ($E_S=2.8$ eV, $E_T=1.4$ eV) [218] or diphenyl tetracene ($E_S=2.5$ eV, $E_T=1.2$ eV) [191] as the fission sensitizer, and platinum complexes such as tetraphenyltetranaphtho platinum porphyrins ($E_T=1.4$ eV) [219, 220] as the phosphorescent emitter. Indeed, although there are many efficient phosphors for visible emission, highly efficiency infrared phosphorescent emitters are rarely reported in the literature. This is possibly due to a lack of motivation for synthesizing such emitters up to this time.

9.2 Feasibility of an Electrically Pumped OSL

Optically pumped organic semiconductor lasers (OSLs) were demonstrated more

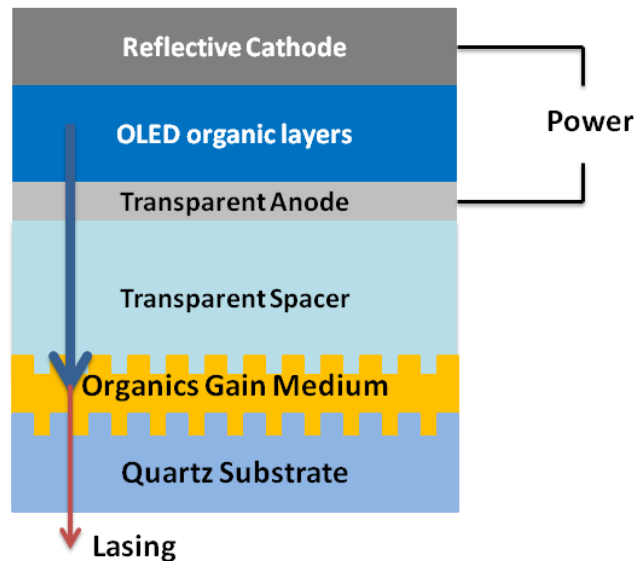


Figure 9.3 Proposed structure for an OLED-pumped-OSL

than 15 years ago [63-65] and it was predicted more than 10 years ago [67, 68] that an electrically pumped OSL could soon be realized. However, there has been no credible report of such a device so far. Difficulties associated with the demonstration of an electrical pumped OSL include significant losses from singlet-polaron annihilation (SPA), singlet-triplet annihilation (STA), large resistivity in organic films, and cavity loss due to electrodes.

A different approach to realize an all-organic electrically pumped laser is to use a high intensity OLED as an optical pump to excite a separate OSL section integrated with the OLED. This method could resolve the problems of SPA and electrode loss, because the spatially separated OSL is optically pumped and there is no charge transport process in its operation. A schematic of such an integrated organic laser is shown in Fig. 9.3. Here, the OSL gain medium is deposited on a DFB grating formed on quartz substrate. Then, a low index spacer is spin-cast on top of the OSL to planarize the surface. Lastly, a

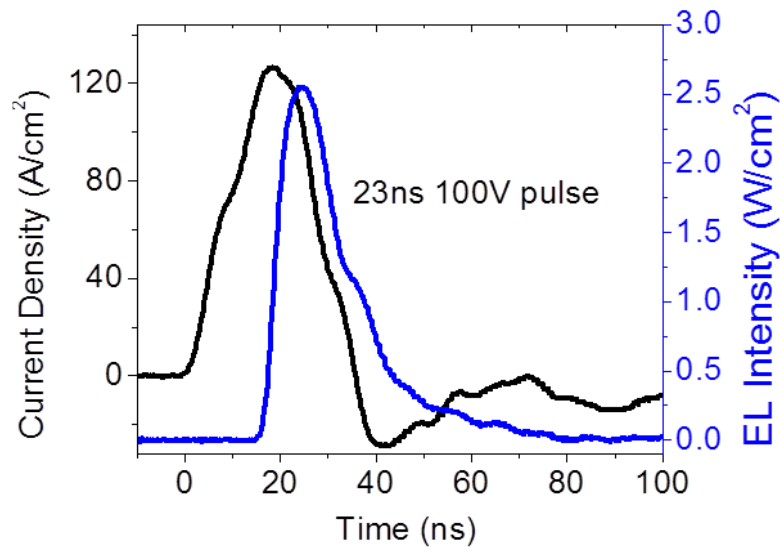


Figure 9.4 Transient current density and emission from a blue emitting OLED driven by a voltage pulse of 100 V

blue or green emitting OLED with a semitransparent bottom electrode and a reflective top electrode is grown on top of the spacer.

To evaluate the feasibility of such an approach, the maximum light output power from the OLED needs to be compared with the minimum optical pumping threshold from the OSL. Table 9.1 summarizes the reported thresholds for optically pumped thin film OSLs. Most notably, Karnutsch et al. demonstrated a threshold as low as 4 W/cm^2 in an OSL using poly[9,9-dioctylfluorene-co-9,9-di(4-methoxy-phenyl)fluorene] (F8DP) with a mixed order distributed feedback (DFB) structure as the gain medium. Although F8DP requires a UV optical pump, similar improvements in threshold can be expected from the same feedback structure, and thus a similar threshold can be expected from gain media such as Dow Red F (a proprietary polymer) or ADS233YE (a polyfluorene with structure available from <http://www.adsdyes.com/>).

To estimate the maximum light output from an OLED, we fabricate an blue emitting OLED on ITO-coated-glass substrate using 3 vol% 4,4'-bis(9-ethyl-3-carbazovinylene)-1,1'-biphenyl (BCzVBi) doped in 4,4'-bis(N-carbazolyl)biphenyl (CBP)

Table 9.1 Literature report on low threshold OSLs

Gain medium	Feedback	Pump Wavelength	Threshold (W/cm^2)	Ref.
Alq ₃ :DCM2	2 nd order DFB	350 nm	700	[4]
ADS233YE	2 nd order DFB	450 nm	217	[6]
Dow Red F	2 nd order 2d DFB	540 nm	110	[8]
BN-PFO	1 st order DFB	390 nm	13	[11]
F8DP	Mixed order DFB	390 nm	4	[13]
Y80F8:20F5	2 nd order DFB	390 nm	30	[14]

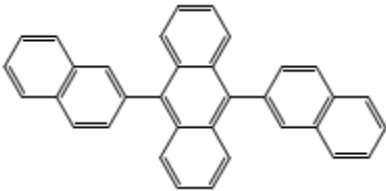
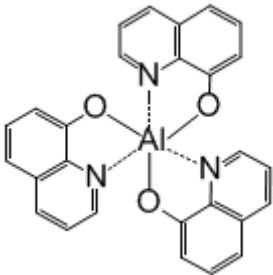
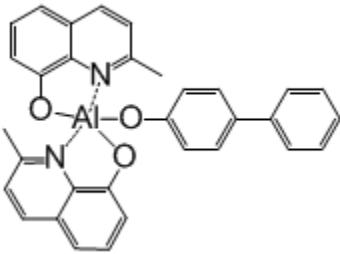
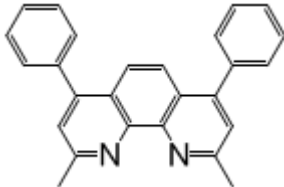
as the emissive layer (the chemical structures for these molecules are in Appendix A) following Sun et al. [221]. When operated using microsecond pulses, as shown in Fig. 9.4, the OLED output can reach 2.5 W/cm^2 at a 100V voltage. If we further consider the light out-coupling improvement in the structure of Fig. 9.3 due to direct harvesting of glass modes [222], the optical power to reach the OSL can exceed 4 W/cm^2 . Also, more efficient blue OLEDs [223] are available using new emitter materials, which can further increase the maximum power.

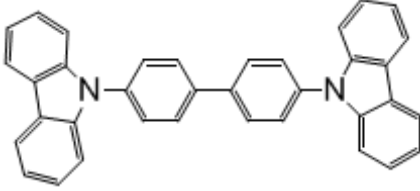
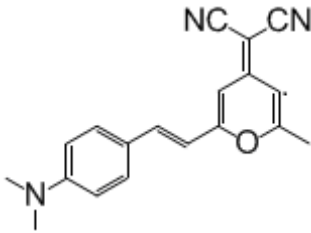
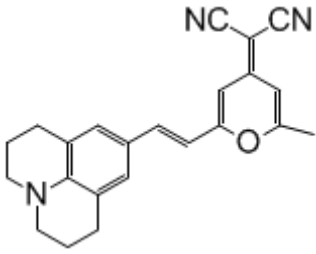
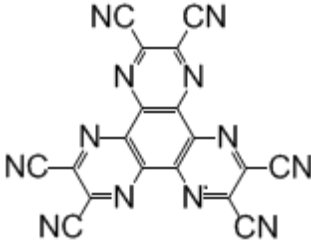
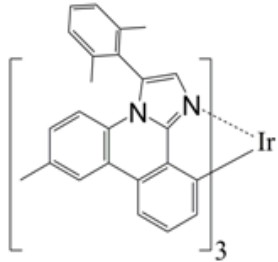
In addition, since the OLED emissive area can be significantly larger than the OSL active area, optical focusing can further increase the pump intensity from the OLED on the OSLs. The focusing strategy may be used for microcavity OLEDs [216], where the angular emission profile is concentrated towards the substrate normal direction. Thus, although a direct electrically pumped OSL may not be available in the near future, an OLED-pumped-OSL is feasible given the state-of-art of both high intensity OLEDs and low threshold OSLs.

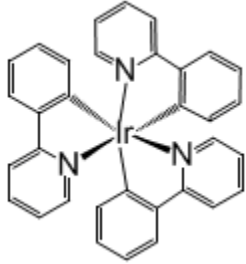
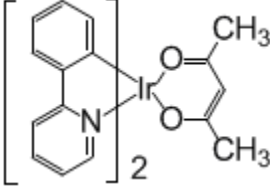
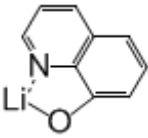
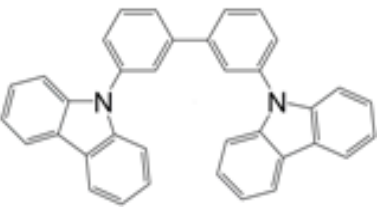
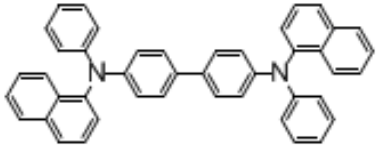
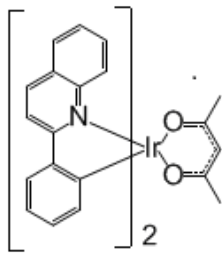
To summarize, the unique features of organic semiconductors will be continuously utilized in future electronic and optoelectronic devices to accomplish goals that conventional materials cannot achieve. The demonstration of transparent, curved, flexible, and stretchable organic devices with performance comparable to, or even surpassing their inorganic counterparts is just a beginning of the era of organic semiconductors. Further, the superior photophysical properties of organic semiconductors can be combined with the desirable electrical properties of inorganic semiconductors in hybrid organic-inorganic devices [6, 108, 224, 225], which are important from both fundamental and practical perspectives.

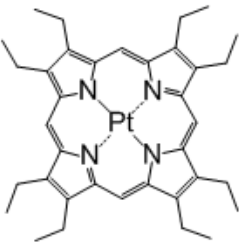
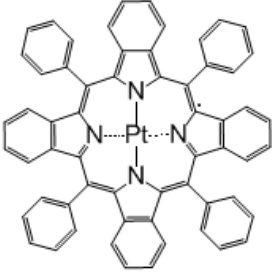
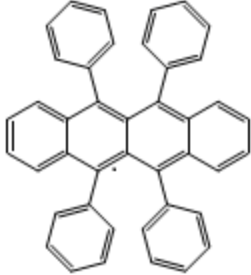
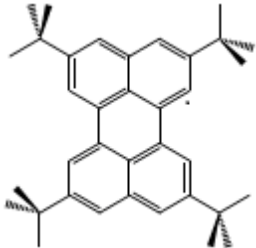
Appendix A

Chemical Structures for Organic Molecules

Short name	Full chemical name	Chemical structure
ADN	9,10-Di(naphth-2-yl)anthracene	
Alq ₃	tris(8-hydroxyquinoline)aluminum	
BAIq	bis(2-methyl-8-quinolinolate)-4-(phenylphenolato)aluminum	
BCP	Bathocuproine	

CBP	4,4'-N,N'-dicarbazole-biphenyl	
DCM	4-dicyanomethylene-2-methyl-6-(<i>p</i> -dimethylaminostyryl)-4 <i>H</i> -pyran	
DCM2	4-(dicyanomethylene)-2-methyl-6-julolidyl-9-enyl-4 <i>H</i> -pyran	
HATCN	hexaazatriphenylene hexacarbonitrile	
Ir(dmp) ₃	iridium (III) tris[3-(2,6-dimethylphenyl)-7-methylimidazo[1,2- <i>f</i>] phenanthridine]	

Ir(ppy) ₃	tris (2-phenylpyridine) iridium	
Ir(ppy) ₂ acac	bis (2-phenylpyridine) (acetylacetonate) iridium	
Liq	8-hydroxyquinolinato lithium	
mCBP	4,4'-bis(3-methylcarbazol-9-yl)-2,2'-biphenyl	
NPD	4,4'-bis[N-(1-naphthyl)-N-phenyl-amino]-biphenyl	
PQIr	<i>bis</i> (2-phenylquinoline) (acetylacetonate)Ir(III)	

PtOEP	octaethylporphine platinum	
Pt(TPBP)	tetraphenyltetrabenzoporphyrin platinum	
Rubrene	rubrene	
TBP	2,5,8,11-tetra-tert-butylperylene	

Appendix B

List of Publications, Conference Presentations and Patents

Publications

1. Yifan Zhang, Jaesang Lee, and Stephen R. Forrest, “Ten-Fold Increase in the Lifetime of Blue Phosphorescent Organic Light Emitting Diodes”, submitted (2014)
2. Yifan Zhang and Stephen R. Forrest, “Triplet Diffusion Leads to Triplet–Triplet Annihilation in Organic Phosphorescent Emitters”, *Chemical Physics Letters* **590**, 106 (2013)
3. Michael Sloatsky, Yifan Zhang, and Stephen R. Forrest, “Temperature Dependence of Polariton Lasing in a Crystalline Anthracene Microcavity”, *Physical Review B* **86**, 045312 (2012)
4. Yifan Zhang and Stephen R. Forrest, “Triplets Contribute to Both an Increase and Loss in Fluorescent Yield in Organic Light Emitting Diodes”, *Physical Review Letters* **108**, 267404 (2012)
5. Yifan Zhang and Stephen R. Forrest, “Existence of Continuous-Wave Threshold for Organic Semiconductor Lasers”, *Physical Review B* **84**, 241301 (2011)

6. Yifan Zhang, Michael Slightsky, and Stephen R. Forrest, “Enhanced efficiency in high-brightness fluorescent organic light emitting diodes through triplet management”, Applied Physics Letters **99**, 223303 (2011)
7. Yifan Zhang, Matthew Whited, Mark E. Thompson, and Stephen R. Forrest, “Singlet–triplet quenching in high intensity fluorescent organic light emitting diodes”, Chemical Physics Letters **495**, 161 (2010)

Conference Presentations

1. (Oral Presentation) Yifan Zhang and Stephen R. Forrest, “Accurate Modeling of Triplet Annihilations in PHOLEDs”, MRS Fall Meeting, Boston, MA (2013)
2. (Poster Presentation) Yifan Zhang and Stephen R. Forrest, “Triplet-triplet Annihilations in Phosphorescent Organic Light Emitting Diodes”, SPIE Optics + Photonics, San Diego, CA (2013)
3. (Poster Presentation) Yifan Zhang and Stephen R. Forrest, “Excited State Interactions in High Intensity Organic Light Emitting Diodes”, Department of Energy, Solid State Lighting Workshop, Long Beach, CA (2013)
4. (Oral Presentation) Yifan Zhang and Stephen R. Forrest, “Triplet Management in Continuous-Wave Organic Semiconductor Lasers”, SPIE Optics + Photonics, San Diego, CA (2012)
5. (Oral Presentation) Yifan Zhang, Michael Slightsky, and Stephen R. Forrest “Triplet Management in Fluorescent Organic Light Emitting Diodes and Organic Lasers”, The Conference on Lasers and Electro-Optics (CLEO), San Jose, CA (2012)

6. (Oral Presentation) Yifan Zhang and Stephen R. Forrest, “Continuous-Wave Organic Semiconductor Lasers”, SPIE Optics + Photonics, San Diego, CA (2011)
7. (Oral Presentation) Yifan Zhang and Stephen R. Forrest, “Singlet-Triplet Quenching in High Intensity Organic Light Emitting Diodes”, 8th International Conference on Electroluminescence and Organic Optoelectronics (ICEL), Ann Arbor, MI (2010)
8. (Oral Presentation) Yifan Zhang, Stephane Kena-Cohen, and Stephen R. Forrest, “Ultra-high Intensity Stacked Organic Light Emitting Diodes under Pulsed Conditions”, MRS Fall Meeting, Boston, MA (2009)

Patents

1. Stephen R. Forrest, Yifan Zhang, and Mark E. Thompson, “Ultra-bright fluorescent organic light emitting diodes with triplet sinks”, Patent # 8456081, Issue date: 06/04/2013
2. Stephen R. Forrest and Yifan Zhang, “Continuous-wave organic semiconductor lasers by triplet managers”, Patent # 8654806, Issue date: 02/18/2014
3. Stephen R. Forrest, Yifan Zhang, Kevin Bergemann, “Ultra-high efficiency (125%) phosphorescent organic light emitting diodes using singlet fission”, filed in March 2012
4. Stephen R. Forrest and Yifan Zhang, “High efficiency hybrid organic/inorganic photovoltaics using singlet fission organic sensitizer”, filed in March 2012
5. Stephen R. Forrest and Yifan Zhang, “High efficiency and brightness fluorescent organic light emitting diodes by triplet-triplet fusion”, filed in March 2012

6. Stephen R. Forrest and Yifan Zhang, “Phosphorescent organic light emitting diodes with high efficiency at high brightness”, filed in March 2013
7. Stephen R. Forrest and Yifan Zhang, “Extended OLED Operational Lifetime Through Doping Profile Management”, filed in November 2013

References

- [1] S. M. Sze, and K. K. Ng, *Physics of Semiconductor Devices* (Wiley-Interscience, Hoboken, New Jersey, 2006), 3rd edn.
- [2] W. Shockley, and H. J. Queisser, *J. Appl. Phys.* **32**, 510 (1961).
- [3] M. L. Huggins, *J. Am. Chem. Soc.* **75**, 4123 (1953).
- [4] N. C. Giebink, and S. R. Forrest, *Phys. Rev. B* **79**, 073302 (2009).
- [5] C. H. M. Maree *et al.*, *J. Appl. Phys.* **84**, 4013 (1998).
- [6] Y. Yang, G. A. Turnbull, and I. D. W. Samuel, *Appl. Phys. Lett.* **92**, 163306 (2008).
- [7] M. A. Hopcroft, W. D. Nix, and T. W. Kenny, *Microelectromechanical Systems, Journal of* **19**, 229 (2010).
- [8] G. Heliotis *et al.*, *J. Appl. Phys.* **96**, 6959 (2004).
- [9] J. M. Torres *et al.*, *Soft Matter* **6**, 5783 (2010).
- [10] V. G. Kozlov *et al.*, *J. Appl. Phys.* **84**, 4096 (1998).
- [11] C. Karnutsch *et al.*, *Appl. Phys. Lett.* **89**, 201108 (2006).
- [12] D. Z. Garbuzov *et al.*, *Chem. Phys. Lett.* **249**, 433 (1996).
- [13] C. Karnutsch *et al.*, *Appl. Phys. Lett.* **90**, 131104 (2007).
- [14] B. K. Yap *et al.*, *Nat Mater* **7**, 376 (2008).
- [15] S. Naka *et al.*, *Synth. Met.* **111–112**, 331 (2000).
- [16] E. F. Kelley, *SID Information Display* **29**, 6 (2013).

- [17] G. Gustafsson *et al.*, *Nature* **357**, 477 (1992).
- [18] G. Gu *et al.*, *Opt. Lett.* **22**, 172 (1997).
- [19] T.-H. Han *et al.*, *Nature Photonics* **6**, 105 (2012).
- [20] T. Sekitani *et al.*, *Nature materials* **8**, 494 (2009).
- [21] J. A. Rogers, T. Someya, and Y. G. Huang, *Science* **327**, 1603 (2010).
- [22] D. J. Lipomi *et al.*, *Adv. Mater.* **23**, 1771 (2011).
- [23] R. C. Hilborn, *American Journal of Physics* **50**, 982 (1982).
- [24] S. R. Forrest, *Nature* **428**, 911 (2004).
- [25] V. Bulovic *et al.*, *Nature* **380**, 29 (1996).
- [26] R. R. Lunt, and V. Bulovic, *Appl. Phys. Lett.* **98** (2011).
- [27] N. Tessler *et al.*, *Adv. Mater.* **21**, 2741 (2009).
- [28] R. W. I. de Boer *et al.*, *Physica Status Solidi a-Applied Research* **201**, 1302 (2004).
- [29] R. R. Lunt, J. B. Benziger, and S. R. Forrest, *Adv. Mater.* **19**, 4229 (2007).
- [30] H. Nakanotani, and C. Adachi, *Appl. Phys. Lett.* **96** (2010).
- [31] P. E. Burrows *et al.*, *Appl. Phys. Lett.* **65**, 2922 (1994).
- [32] J. Shinar, and R. Shinar, *J. Phys. D: Appl. Phys.* **41**, 133001 (2008).
- [33] Y. Yang, G. A. Turnbull, and I. D. Samuel, *Adv. Funct. Mater.* **20**, 2093 (2010).
- [34] S. R. Forrest, *Chem. Rev.* **97**, 1793 (1997).
- [35] H. Yamamoto *et al.*, *Appl. Phys. Lett.* **100** (2012).
- [36] Y. Zhang, and S. R. Forrest, *Phys. Rev. Lett.* **108**, 267404 (2012).
- [37] C. Tang, and S. VanSlyke, *Appl. Phys. Lett.* **51**, 913 (1987).
- [38] M. Baldo *et al.*, *Adv. Mater.* **10**, 1505 (1998).

- [39] R. R. Lunt *et al.*, Appl. Phys. Lett. **95** (2009).
- [40] M. Shtein *et al.*, J. Appl. Phys. **93**, 4005 (2003).
- [41] G. J. McGraw, and S. R. Forrest, Adv. Mater. (2013).
- [42] T. Hebner *et al.*, Appl. Phys. Lett. **72**, 519 (1998).
- [43] R. A. Laudise *et al.*, J. Cryst. Growth **187**, 449 (1998).
- [44] S. Van Slyke *et al.*, SID Symposium Digest of Technical Papers **33**, 886 (2002).
- [45] U. Hoffmann *et al.*, SID Symposium Digest of Technical Papers **41**, 688 (2010).
- [46] D. Käfer, and G. Witte, PCCP **7**, 2850 (2005).
- [47] M. Pope, H. P. Kallmann, and P. Magnante, The Journal of Chemical Physics **38**, 2042 (1963).
- [48] T. C. Werner, J. Chang, and D. M. Hercules, J. Am. Chem. Soc. **92**, 763 (1970).
- [49] P. S. Vincett *et al.*, Thin Solid Films **94**, 171 (1982).
- [50] J. Kalinowski, and J. Godlewski, Chem. Phys. Lett. **36**, 345 (1975).
- [51] M. A. Baldo *et al.*, Appl. Phys. Lett. **75**, 4 (1999).
- [52] M. A. Baldo *et al.*, Nature **395**, 151 (1998).
- [53] C. Adachi *et al.*, J. Appl. Phys. **90**, 5048 (2001).
- [54] M. Segal *et al.*, Phys. Rev. B **68**, 075211 (2003).
- [55] M. A. Baldo *et al.*, Phys. Rev. B **60**, 14422 (1999).
- [56] D. Y. Kondakov *et al.*, J. Appl. Phys. **106**, 124510 (2009).
- [57] B. H. Wallikewitz *et al.*, Phys. Rev. B **85**, 045209 (2012).
- [58] M. A. Baldo, M. E. Thompson, and S. R. Forrest, Nature **403**, 750 (2000).
- [59] B. W. D'Andrade *et al.*, Appl. Phys. Lett. **79**, 1045 (2001).

- [60] K. Nassau, *Color for Science, Art and Technology* (North Holland; 1 edition, 1998).
- [61] S. Reineke *et al.*, *Nature* **459**, 234 (2009).
- [62] J. Piprek, *physica status solidi (a)* **207**, 2217 (2010).
- [63] F. Hide *et al.*, *Science* **273**, 1833 (1996).
- [64] N. Tessler, G. J. Denton, and R. H. Friend, *Nature* **382**, 695 (1996).
- [65] V. G. Kozlov *et al.*, *Nature* **389**, 362 (1997).
- [66] I. D. W. Samuel, and G. A. Turnbull, *Chem. Rev.* **107**, 1272 (2007).
- [67] V. G. Kozlov *et al.*, *IEEE Journal of Quantum Electronics* **36**, 18 (2000).
- [68] N. Tessler, *Adv. Mater.* **11**, 363 (1999).
- [69] C. J. M. v. Rijn, *Journal of Microlithography, Microfabrication, and Microsystems* **5**, 011012 (2006).
- [70] M. Lehnhardt *et al.*, *Phys. Rev. B* **81**, 165206 (2010).
- [71] Y. Zhang, and S. R. Forrest, *Phys. Rev. B* **84**, 241301 (2011).
- [72] C. W. Tang, *Appl. Phys. Lett.* **48**, 183 (1986).
- [73] J. You *et al.*, *Nature communications* **4**, 1446 (2013).
- [74] J. D. Zimmerman *et al.*, *ACS nano* **7**, 9268 (2013).
- [75] P. Peumans, S. Uchida, and S. R. Forrest, *Nature* **425**, 158 (2003).
- [76] M. C. Scharber *et al.*, *Adv. Mater.* **18**, 789 (2006).
- [77] A. Tsumura, H. Koezuka, and T. Ando, *Appl. Phys. Lett.* **49**, 1210 (1986).
- [78] V. Podzorov *et al.*, *Appl. Phys. Lett.* **83**, 3504 (2003).
- [79] Y.-Y. Lin *et al.*, *Electron Device Letters, IEEE* **18**, 606 (1997).
- [80] H. Sirringhaus, *Adv. Mater.* **21**, 3859 (2009).

- [81] G. H. Gelinck *et al.*, Nature materials **3**, 106 (2004).
- [82] G. Gu *et al.*, J. Appl. Phys. **86**, 4067 (1999).
- [83] I. Hill *et al.*, Appl. Phys. Lett. **73**, 662 (1998).
- [84] J. C. Scott, Journal of Vacuum Science & Technology A **21**, 521 (2003).
- [85] O. Richardson, Physical Review **23**, 153 (1924).
- [86] W. Schottky, Zeitschrift für Physik A Hadrons and Nuclei **118**, 539 (1942).
- [87] P. R. Emtage, and J. J. O'Dwyer, Phys. Rev. Lett. **16**, 356 (1966).
- [88] J. C. Scott, and G. G. Malliaras, Chem. Phys. Lett. **299**, 115 (1999).
- [89] B. Ruhstaller *et al.*, J. Appl. Phys. **89**, 4575 (2001).
- [90] B. Ruhstaller *et al.*, Selected Topics in Quantum Electronics, IEEE Journal of **9**, 723 (2003).
- [91] R. H. Fowler, and L. Nordheim, Proceedings of the Royal Society of London. Series A, Containing Papers of a Mathematical and Physical Character **119**, 173 (1928).
- [92] P. S. Davids *et al.*, Appl. Phys. Lett. **69**, 2270 (1996).
- [93] A. J. Heeger, I. D. Parker, and Y. Yang, Synth. Met. **67**, 23 (1994).
- [94] V. I. Arkhipov *et al.*, J. Appl. Phys. **84**, 848 (1998).
- [95] M. A. Baldo, and S. R. Forrest, Phys. Rev. B **64** (2001).
- [96] Y. N. Gartstein, and E. M. Conwell, Chem. Phys. Lett. **217**, 41 (1994).
- [97] R. W. G. N.F. Mott, *Electronic Processes in Ionic Crystals* (Dover Publication (2nd edition), 1964).
- [98] A. Rose, Physical Review **97**, 1538 (1955).
- [99] P. Mark, and W. Helfrich, J. Appl. Phys. **33**, 205 (1962).
- [100] P. E. Burrows, and S. R. Forrest, Appl. Phys. Lett. **64**, 2285 (1994).

- [101] A. Campbell, D. Bradley, and D. Lidzey, *J. Appl. Phys.* **82**, 6326 (1997).
- [102] N. Karl, *Synth. Met.* **133**, 649 (2003).
- [103] H. Yamamoto *et al.*, *Appl. Phys. Lett.* **86**, 083502 (2005).
- [104] M. A. Lampert, *Physical Review* **103**, 1648 (1956).
- [105] P. E. Burrows *et al.*, *J. Appl. Phys.* **79**, 7991 (1996).
- [106] T. Matsushima, H. Sasabe, and C. Adachi, *Appl. Phys. Lett.* **88** (2006).
- [107] M. Pope, and C. E. Swenberg, *Electronic Processes in Organic Crystals and Polymers* (Oxford University Press, New York, 1999), Second edn.
- [108] V. Agranovich, Y. N. Gartstein, and M. Litinskaya, *Chem. Rev.* **111**, 5179 (2011).
- [109] V. Bulovic *et al.*, *Chem. Phys.* **210**, 1 (1996).
- [110] P. W. Atkins, and R. S. Friedman, *Molecular quantum mechanics* (Oxford university press Oxford, 1997), Vol. 3.
- [111] T. Förster, *Discuss. Faraday Soc.* **27**, 7 (1959).
- [112] D. L. Dexter, *The Journal of Chemical Physics* **21**, 836 (1953).
- [113] S. Chandrasekhar, *Reviews of Modern Physics* **15**, 1 (1943).
- [114] C. Gartner *et al.*, *J. Appl. Phys.* **101**, 023107 (2007).
- [115] M. A. Baldo, R. J. Holmes, and S. R. Forrest, *Phys. Rev. B* **66**, 035321 (2002).
- [116] M. A. Baldo, C. Adachi, and S. R. Forrest, *Phys. Rev. B* **62**, 10967 (2000).
- [117] S. Reineke, K. Walzer, and K. Leo, *Phys. Rev. B* **75**, 125328 (2007).
- [118] Y. Zhang *et al.*, *Chem. Phys. Lett.* **495**, 161 (2010).
- [119] R. G. Kepler *et al.*, *Phys. Rev. Lett.* **10**, 400 (1963).
- [120] V. G. Kozlov *et al.*, *Appl. Phys. Lett.* **74**, 1057 (1999).
- [121] X. Qi, M. Slocus, and S. Forrest, *Appl. Phys. Lett.* **93**, 193306 (2008).

- [122] S. R. Forrest, D. D. C. Bradley, and M. E. Thompson, *Adv. Mater.* **15**, 1043 (2003).
- [123] C. W. Tang, S. A. VanSlyke, and C. H. Chen, *J. Appl. Phys.* **65**, 3610 (1989).
- [124] J. Shi, and C. W. Tang, *Appl. Phys. Lett.* **80**, 3201 (2002).
- [125] K. Goushi *et al.*, *J. Appl. Phys.* **95**, 7798 (2004).
- [126] I. Tanaka, Y. Tabata, and S. Tokito, *Phys. Rev. B* **71**, 205207 (2005).
- [127] C. W. Ma *et al.*, *Chem. Phys. Lett.* **397**, 87 (2004).
- [128] C. Hosokawa *et al.*, *Appl. Phys. Lett.* **60**, 1220 (1992).
- [129] Y. Sun *et al.*, *Appl. Phys. Lett.* **90** (2007).
- [130] R. H. Young, C. W. Tang, and A. P. Marchetti, *Appl. Phys. Lett.* **80**, 874 (2002).
- [131] N. C. Giebink, and S. R. Forrest, *Phys. Rev. B* **77**, 235215 (2008).
- [132] M. A. Baldo, and S. R. Forrest, *Phys. Rev. B* **62**, 10958 (2000).
- [133] H. Kanno, Y. Sun, and S. R. Forrest, *Appl. Phys. Lett.* **86** (2005).
- [134] N. J. Turro, *Modern Molecular Photochemistry* (University Science Books, Sausalito, CA, 1991).
- [135] J. Mezyk *et al.*, *Chem. Phys. Lett.* **395**, 321 (2004).
- [136] I. Sokolik *et al.*, *Appl. Phys. Lett.* **69**, 4168 (1996).
- [137] L.-Z. Yu *et al.*, *J. Appl. Phys.* **105**, 013105 (2009).
- [138] T.-H. Liu, C.-Y. Iou, and C. H. Chen, *Curr. Appl. Phys.* **5**, 218 (2005).
- [139] W. G. Herkstroeter, and P. B. Merkel, *Journal of Photochemistry* **16**, 331 (1981).
- [140] V. Bulovic *et al.*, *Science* **279**, 553 (1998).
- [141] T. Riedl *et al.*, *Appl. Phys. Lett.* **88**, 241116 (2006).
- [142] V. G. Kozlov *et al.*, *Appl. Phys. Lett.* **72**, 144 (1998).

- [143] S. Riechel *et al.*, *Opt. Lett.* **26**, 593 (2001).
- [144] S. Kóna-Cohen, *Appl. Phys. Lett.* **99**, 041114 (2011).
- [145] S. L. Chuang, *Physics of Photonic Devices* (Wiley, 2009), 2nd edn.
- [146] L. A. Coldren, and S. W. Corzine, *Diode Lasers and Photonic Integrated Circuits* (Wiley, New York, 1995).
- [147] R. Xia *et al.*, *Org. Electron.* **4**, 165 (2003).
- [148] M. Lehnhardt *et al.*, *Org. Electron.* **12**, 486 (2011).
- [149] S.-W. Wen, M.-T. Lee, and C. H. Chen, *J. Display Technol.* **1**, 90 (2005).
- [150] B. B. Snavely, *Proc. IEEE* **57**, 1374 (1969).
- [151] R. P. Groff, R. E. Merrifield, and P. Avakian, *Chem. Phys. Lett.* **5**, 168 (1970).
- [152] D. Yokoyama *et al.*, *Appl. Phys. Lett.* **99**, 123303 (2011).
- [153] S. M. King *et al.*, *J. Appl. Phys.* **109**, 074502 (2011).
- [154] Y. Luo, and H. Aziz, *Adv. Funct. Mater.* **20**, 1285 (2010).
- [155] J. Fourny, G. Delacôte, and M. Schott, *Phys. Rev. Lett.* **21**, 1085 (1968).
- [156] D. Kasemann *et al.*, *Phys. Rev. B* **84**, 115208 (2011).
- [157] A. Kohler, and H. Bassler, *Materials Science & Engineering R-Reports* **66**, 71 (2009).
- [158] B. Dick, and B. Nickel, *Chem. Phys.* **78**, 1 (1983).
- [159] M. Montalti *et al.*, *Handbook of Photochemistry* (CRC Press, Boca Raton, FL, 2006), 3rd edn.
- [160] J. D. Debad *et al.*, *J. Am. Chem. Soc.* **118**, 2374 (1996).
- [161] K. Okumoto *et al.*, *Appl. Phys. Lett.* **89**, 013502 (2006).
- [162] T. Tsutsui, *MRS Bull.* **22**, 39 (1997).

- [163] R. R. Lunt *et al.*, J. Appl. Phys. **105**, 053711 (2009).
- [164] G. Sakamoto *et al.*, Appl. Phys. Lett. **75**, 766 (1999).
- [165] R. R. Lunt, J. B. Benziger, and S. R. Forrest, Adv. Mater. **22**, 1233 (2010).
- [166] M. B. Smith, and J. Michl, Chem. Rev. **110**, 6891 (2010).
- [167] P. M. Zimmerman, Z. Zhang, and C. B. Musgrave, Nat Chem **2**, 648 (2010).
- [168] J. Lee, P. Jadhav, and M. A. Baldo, Appl. Phys. Lett. **95**, 033301 (2009).
- [169] P. J. Jadhav *et al.*, Nano Lett. **11**, 1495 (2011).
- [170] A. Rzasnyanskiy, and I. Biaggio, Phys. Rev. B **84**, 193203 (2011).
- [171] M. G. Helander *et al.*, Science **332**, 944 (2011).
- [172] Y.-S. Park *et al.*, Adv. Funct. Mater., n/a (2013).
- [173] N. Chopra *et al.*, Appl. Phys. Lett. **97**, 033304 (2010).
- [174] *Solid State Lighting Research and Development Multi-year program plan*, <http://www1.eere.energy.gov/buildings/ssl/projects.html> (U.S. Department of Energy, 2013).
- [175] J. Kalinowski *et al.*, Phys. Rev. B **66** (2002).
- [176] J. C. Ribierre *et al.*, Phys. Rev. Lett. **100**, 017402 (2008).
- [177] W. Staroske *et al.*, Phys. Rev. Lett. **98**, 197402 (2007).
- [178] E. Engel, K. Leo, and M. Hoffmann, Chem. Phys. **325**, 170 (2006).
- [179] T. Förster, Z. Naturforsch. **A4**, 321 (1949).
- [180] R. C. Powell, and Z. G. Soos, J. Lumin. **11**, 1 (1975).
- [181] R. C. Powell, Phys. Rev. B **2**, 1159 (1970).
- [182] K. B. Eisenthal, and S. Siegel, The Journal of Chemical Physics **41**, 652 (1964).
- [183] S. Lamansky *et al.*, J. Am. Chem. Soc. **123**, 4304 (2001).

- [184] M. Lehnhardt *et al.*, *Org. Electron.* **12**, 1346 (2011).
- [185] G. Ponterini *et al.*, *J. Am. Chem. Soc.* **105**, 4639 (1983).
- [186] Y. Kawamura *et al.*, *Appl. Phys. Lett.* **86**, 071104 (2005).
- [187] Y. Kawamura *et al.*, *Phys. Rev. Lett.* **96**, 017404 (2006).
- [188] see Supplemental Material.
- [189] E. B. Namdas *et al.*, *Appl. Phys. Lett.* **86**, 091104 (2005).
- [190] W. Holzer, A. Penzkofer, and T. Tsuboi, *Chem. Phys.* **308**, 93 (2005).
- [191] S. T. Roberts *et al.*, *J. Am. Chem. Soc.* **134**, 6388 (2012).
- [192] A. K. Bansal *et al.*, *Chem. Phys.* **330**, 118 (2006).
- [193] N. C. Giebink *et al.*, *J. Appl. Phys.* **105** (2009).
- [194] N. C. Giebink *et al.*, *Journal of Applied Physics* **103** (2008).
- [195] S. A. Van Slyke, C. H. Chen, and C. W. Tang, *Appl. Phys. Lett.* **69**, 2160 (1996).
- [196] H. Aziz *et al.*, *Science* **283**, 1900 (1999).
- [197] A. B. Chwang, R. C. Kwong, and J. J. Brown, *Appl. Phys. Lett.* **80**, 725 (2002).
- [198] R. C. Kwong *et al.*, *Appl. Phys. Lett.* **81**, 162 (2002).
- [199] S. H. Kim, J. Jang, and J. Y. Lee, *Applied Physics Letters* **90**, 203511 (2007).
- [200] B. D. Chin, and C. Lee, *Advanced Materials* **19**, 2061 (2007).
- [201] R. J. Holmes *et al.*, *Appl. Phys. Lett.* **82**, 2422 (2003).
- [202] R. Seifert *et al.*, *Organic Electronics* (2012).
- [203] D. Y. Kondakov, and R. H. Young, *J. Appl. Phys.* **108**, 074513 (2010).
- [204] N. C. Erickson, and R. J. Holmes, *Adv. Funct. Mater.* (2013).
- [205] G. Lei, L. Wang, and Y. Qiu, *Japanese journal of applied physics* **43**, 1226 (2004).

- [206] B. D. Chin *et al.*, in *Optics & Photonics* (International Society for Optics and Photonics, 2006), pp. 633315.
- [207] Z. Liu *et al.*, *Org. Electron.* **14**, 852 (2013).
- [208] S. Forrest *et al.*, *Synthetic Metals* **91**, 9 (1997).
- [209] T.-Y. Cho, C.-L. Lin, and C.-C. Wu, *Appl. Phys. Lett.* **88**, 111106 (2006).
- [210] H. Kanno *et al.*, *Advanced Materials* **18**, 339 (2006).
- [211] K. Celebi, T. Heidel, and M. Baldo, *Opt. Express* **15**, 1762 (2007).
- [212] H. Yamamoto *et al.*, *Applied Physics Letters* **99**, 033301 (2011).
- [213] Q. Wang, and H. Aziz, *ACS Applied Materials & Interfaces* **5**, 8733 (2013).
- [214] C. Féry *et al.*, *Applied Physics Letters* **87** (2005).
- [215] V. Bulovic *et al.*, *Phys. Rev. B* **58**, 3730 (1998).
- [216] C. Xiang *et al.*, *Light: Science & Applications* **2**, e74 (2013).
- [217] M. Stokes *et al.*, Microsoft and Hewlett-Packard Joint Report (1996).
- [218] J. C. Johnson, A. J. Nozik, and J. Michl, *J. Am. Chem. Soc.* **132**, 16302 (2010).
- [219] C. Borek *et al.*, *Angewandte Chemie-International Edition* **46**, 1109 (2007).
- [220] J. R. Sommer *et al.*, *ACS Applied Materials & Interfaces* **1**, 274 (2009).
- [221] Y. Sun *et al.*, *Nature* **440**, 908 (2006).
- [222] B. C. Krummacher *et al.*, *Org. Electron.* **10**, 478 (2009).
- [223] T. Ogiwara *et al.*, in *SID Symposium Digest of Technical Papers* (Wiley Online Library, 2013), pp. 515.
- [224] P. J. Hagerman, D. Hagerman, and J. Zubieta, *Angew. Chem. Int. Ed.* **38**, 2638 (1999).
- [225] C. Kagan, D. Mitzi, and C. Dimitrakopoulos, *Science* **286**, 945 (1999).